Earth-Science Reviews 130 (2014) 1–48

Contents lists available at ScienceDirect

Earth-Science Reviews

journal homepage: www.elsevier.com/locate/earscirev

Geophysical constraints on the link between cratonization and orogeny: Evidence from the Tibetan Plateau and the North China Craton

Zhongjie Zhang [a,†], Jiwen Teng [a], Fabio Romanelli [b], Carla Braitenberg [b], Zhifeng Ding [c], Xuemei Zhang [a], Lihua Fang [c], Sufang Zhang [a], Jianping Wu [c], Yangfan Deng [a,d,*], Ting Ma [a], Ruomei Sun [a], Giuliano F. Panza [b,c,e]

[a] State Key Laboratory of Lithospheric Evolution, Institute of Geology and Geophysics, Chinese Academy of Sciences, Beijing 100029, China
[b] Department of Mathematics and Geosciences, University of Trieste, Via Weiss, I-34127 Trieste, Italy
[c] Institute of Geophysics, China Earthquake Administration, Beijing 100080, China
[d] Guangzhou Institute of Geochemistry, Chinese Academy of Sciences, Guangzhou 510640, China
[e] International Centre for Theoretical Physics, SAND Group, I-34151 Trieste, Italy

ARTICLE INFO

Article history:
Received 21 August 2013
Accepted 16 December 2013
Available online 30 December 2013

Keywords:
Cratonization
Orogeny
Tibetan Plateau
North China Craton
3D seismic and gravity tomography
Mantle flow

ABSTRACT

Understanding the geodynamic process of orogeny and cratonization, and their transition is among the key topics of research in evaluating the link between plate tectonics and continental dynamics. The Tibetan Plateau and the North China Craton (NCC), two key areas in mainland China, offer excellent laboratories to understand continental tectonics over a broad span of Earth history. Particularly, the deep structure of the lithosphere as imaged from geophysical data on the Tibetan Plateau and the NCC provide important clues in understanding orogeny and cratonization. The Tibetan Plateau is the largest and highest plateau on Earth in terms of mean altitude, and is an important region for understanding the mechanisms of continent–continent collision and Cenozoic plateau uplift. The NCC is an Archean craton that underwent lithospheric disruption during the Mesozoic. Here we reconstruct the main features of the structure of the crust and upper mantle from surface wave tomography and gravity modeling in Tibet and its neighboring regions, in order to understand the modality of the convergence and collision process between the Indian and Eurasian plates, and the influence of this process on the uplift of the plateau. In the NCC, geological, geochemical, geophysical and tectonic investigations demonstrate that lithospheric destruction mainly occurred in the Eastern Block. The crustal structure of the NCC is reconstructed from ambient noise surface wave tomography and the different possible disruption mechanisms are evaluated. The Vs (shear-wave velocity) tomography results, and the density (ρ) structure of the crust and upper mantle (to about 350 km depth) demonstrate the lateral variation of the thickness of the metasomatic lid between the south and north of the Bangong–Nujiang suture (BNS) and the west and east of Tibet, which suggest that the leading edge of the subducting Indian slab reaches the BNS. The subduction angle of Indian Plate indicates a transition from steep to shallow from the west to east Tibet. Sections depicting the gravitational potential energy suggest that mantle flow contributes to the subduction of the Indian Plate as far as the BNS and the transition from the asthenospheric layer to the metasomatic lid overlaps with the transition from north–south shortening in south Tibet to eastward tectonic escape in north Tibet (Qiangtang and Songpan–Ganzi blocks). Both Vs and ρ models suggest the following. (1) North–southward lower-crust flow beneath the eastern NCC and interaction between the westward mantle flow and eastward escape flow beneath the central NCC (in addition to the earlier proposed mechanisms of delamination and thermal erosion) played important roles in the lithospheric disruption of the Archean craton. (2) Mantle flow plays an important role in the continental tectonic transition between neighboring tectonic blocks and within the cycle between orogeny and cratonization.

Contents

* Corresponding author at: State Key Laboratory of Lithospheric Evolution, Institute of Geology and Geophysics, Chinese Academy of Sciences, Beijing 100029, China.
E-mail addresses: dengyangfan@mail.iggcas.ac.cn (Y. Deng), panza@units.it (G.F. Panza).
† Deceased: [1964–2013].

0012-8252/$ – see front matter © 2013 Elsevier B.V. All rights reserved.
http://dx.doi.org/10.1016/j.earscirev.2013.12.005

1. Introduction

Since late 60s, plate tectonics has been accepted as the general framework that governs global tectonics with supportive evidence from multi-disciplinary investigations and considerably advanced our understanding of orogeny and the evolution of cratons. China mainland, composed of three tectonic domains: the Tethys, circum Pacific and Paleo-Asia (Fig. 1a), and subdivided into 18 tectonic units, is one of the excellent regions to evaluate continental dynamics (Yuan, 1996a, b; Li and Mooney, 1998; Zhang et al., 2011e; Teng et al., 2013). The Tibetan Plateau (Fig. 1b) and the North China Craton (NCC) (Fig. 1c) have been in global focus for two main reasons: (1) the Tibetan Plateau is a key area for the understanding of the Cenozoic (and ongoing) continent–continent collision (Yin and Harrison, 2000; Aitchison et al., 2011; Zhang et al., 2012), and (2) the NCC is one of the best natural laboratories to evaluate decratonization through Mesozoic lithospheric thinning (Zhai et al., 2007; Zhu and Zheng, 2009; G. Zhu et al., 2012; Zhang et al., 2012; Guo et al., 2013; Li et al., 2013a,b; Yang et al., 2013; Zhang et al., 2013b,c).

The Tibetan Plateau is characterized by a high mean altitude (>4000 m) and ongoing continent–continent collisional orogeny. This orogenic system has been largely created by the India–Asian collision over the past 70–50 million years, and is part of the greater Himalayan–Alpine system that extends from the Mediterranean Sea in the west, to the Sumatra arc of Indonesia in the east, over a distance of more than 7000 km (Yin, 2006). This extraordinarily long and complex amalgamated belt developed in response to the closure of the Tethys Ocean between two great landmasses, namely between Laurasia in the north and Gondwana in the south, a process that has been taking place since the Paleozoic (Hsü et al., 1995; Sengör and Natal'in, 1996).

The Himalayan–Tibetan orogen and its neighboring regions in East Asia are ideal regions for studying continent–continent collision (Yin, 2006). The mountain building process is active, so many geological relationships can be demonstrated directly using the methods of neotectonic studies (Armijo et al., 1989; Holt et al., 1995; Bilham et al., 1997; Lacassin et al., 1998; Van der Woerd et al., 1998; Larson et al., 1999; Shen and Jin, 1999; Shen et al., 2001). Secondly, the history of the plate boundary is well known, so the cause of intracontinental deformation can be quantitatively defined as a time-dependent, boundary-value problem (Peltzer and Tapponnier, 1988; Houseman and England, 1996; Kong and Bird, 1996; Peltzer and Saucier, 1996; Royden, 1996; Kong et al., 1997; Royden et al., 1997; Kumar et al., 2006). Thirdly, the collision process has produced a variety of geological characteristics, such as large-scale thrust, strike-slip and normal fault systems (Burg and Chen, 1984; Tapponnier et al., 1986; Burchfiel et al., 1992; Yin et al., 1994), leucogranite magmatism (Harrison et al., 1998), widespread volcanism (Deng, 1989; Arnaud et al., 1992; Turner et al., 1993; Chung et al., 1998; Deng, 1998), regional metamorphism (Le Fort, 1996; Searle, 1996) and the formation of intracontinental and continental-margin oceanic basins (Brias et al., 1993; Song and Wang, 1993). All these geological characteristics and processes may be useful

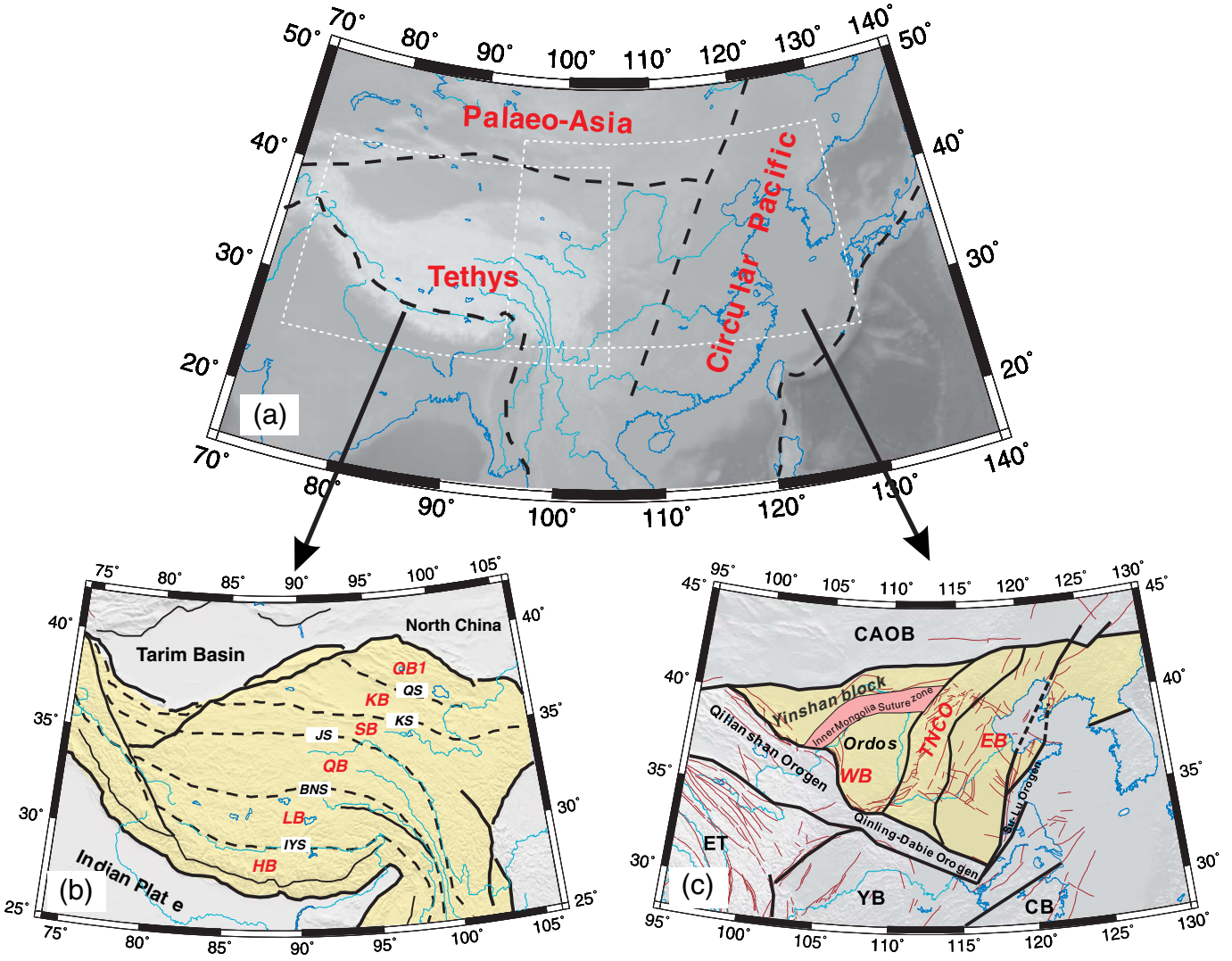

Fig. 1. (a) Simplified geological map showing the study area. (b) Outline map of the Tibetan Plateau. Key to symbols: IYS: Indus–Yarlung suture; BNS: Bangong–Nujiang suture; JS: Jinshajiang suture; KS: Anyimaqen–Kunlun–Mutztagh suture; QS: South Qilian suture; HB: Himalayan Block; LB: Lhasa Block; QB: Qiangtang Block; SB: Songpan–Ganzi Block; KB: Kunlun–Qaidam Block; QB1: Qilian Block. (c) Outline map of North China and the surrounding area. WB: Western Block; EB: Eastern Block; TNCO: Trans-North China Orogen; YB: Yangtze Block; CB: Cathaysia Block; ET: Eastern Tibet. Faults are delineated by red lines.
Tectonic lines depicted after Yin and Harrison (2000).

proxy indicators for the deep Earth processes involved in the dynamics of the continent–continent collision. Although numerous geophysical experiments have been carried out in the Tibetan Plateau in the framework of national (China) and international programs (Teng et al., 1981, 1983; Hirn et al., 1984a,b; Teng et al., 1985a,b; Xiong et al., 1985; Chang et al., 1988; Dewey, 1988; Zhao et al., 1993; Hirn et al., 1995; Makovsky et al., 1996; Yuan, 1996a,b; Teng et al., 1997; Xiong and Liu, 1997; Makovsky et al., 1999; Teng et al., 1999; Zhao et al., 2001a,b; Kind et al., 2002; Xiong and Teng, 2002; Wittlinger et al., 2004; Zhang and Klemperer, 2005; Zhang et al., 2008; Nábělek et al., 2009; Kind and Yuan, 2010; Zhang and Klemperer, 2010; Zhang et al., 2010b; Karplus et al., 2011; Mechie and Kind, 2013; Zhang et al., 2013d), the mechanism of uplift of the plateau is still in dispute.

The NCC is unusual among global cratons because of its long and complex Precambrian evolution and Phanerozoic destruction (Zhai and Santosh, 2011, 2013), with intense contemporary tectonics, as shown by high heat flow and frequent intra-plate earthquakes (Zhai et al., 2007). The NCC consists of two major blocks, the Western Block and the Eastern Block, which were amalgamated about 1.8–1.9 Ga along the Trans-North China Orogen (Zhao and Cawood, 1999; Zhao et al., 2005; Kusky et al., 2007; Zhao et al., 2010a; Trap et al., 2012). The Western Block was created through the collision between the Yinshan Block in the north and the Ordos Block in the south along the Inner Mongolia Suture Zone (incorporating the Khondalite Belt (Zhao et al., 2005; Santosh et al., 2007a,b; Santosh, 2010; Meng, 2003). More recently, Zhai and Santosh (2011) proposed a model of the amalgamation of seven micro-blocks, named the Jiaoliao (JL), Qianhuai (QH), Ordos (OR), Jining (JN), Xuchang (XCH), Xuhuai (XH) and Alashan (ALS) Blocks, to construct the basic tectonic framework of the NCC at the end of Neoarchean. The Archean lithospheric mantle experienced a complex evolution process through the Proterozoic and Phanerozoic, which was fairly heterogeneous in space and time. A mixture of rocks, with ages ranging from Archean to Phanerozoic, characterizes the present-day lithospheric mantle (Liu et al., 2000). Geochemical evidence from some sites in the NCC indicates that the lithosphere was cold and ~200 km thick in the Paleozoic, but became hot and less than 90 km thick in the Cenozoic (Fan and Menzies, 1992; H.F. Zhang et al., 2007; Zheng et al., 2009). Removal or thinning of the lithospheric mantle beneath cratons is an important event in the Earth's evolution (Lee et al., 2000; Gao et al., 2002; Riley et al., 2003). Beneath the NCC,

more than 100 km of lithospheric thickness was lost during the Mesozoic (Menzies et al., 1993; Griffin et al., 1998, 1999; Fan et al., 2000; Xu, 2001; Zheng et al., 2001; Griffin and O'Reilly, 2003). Receiver function results demonstrate the difference in the intensity of lithospheric disruption between the western and the eastern NCC (Zheng T.Y. et al., 2005, 2006, 2007b; Chen et al., 2008; Zheng et al., 2008b,c, 2009; H.F. Zhang et al., 2010). The crustal response to the disruption of the NCC lithosphere is still an open problem even though dense wide-angle seismic profiles (Teng et al., 2010, 2013) were undertaken during the past three decades as a part of the monitoring and prediction of earthquakes in the area of China's capital.

The NCC is considered as an example for the transition from orogen to craton and then to orogen (Kusky et al., 2007; Zhai et al., 2007), as demonstrated by the amalgamation of several microblocks to become a coherent craton, followed by lithosphere thinning and destruction, and the center of the NCC considered as an orogen. In this paper, we provide an overview of the deep structure of the Tibetan Plateau and the NCC based on the large amount of data acquired from recent studies on the deep structure beneath these regions.

2. Salient tectonic features of the Tibetan Plateau and the North China Craton

2.1. Tibetan Plateau

Asia is a collage of continental fragments, assembled mainly in the Paleozoic and Mesozoic, with the latest amalgamation having occurred when India began colliding with Asia in early Cenozoic (Lee and Lawver, 1995; Rowley, 1998; Hodges, 2000; and references therein). A direct consequence of this collision, which began approximately 70–65 million years ago, is the birth of the Himalayas and the Tibetan Plateau, separated from each other by the Indus–Yarlung–Zangbo suture (IYS), a relict of the Neo-Tethyan ocean floor. The Tibetan Plateau consists primarily of five nearly west–east stretching tectonic blocks successively accreted to Eurasia, namely (from south to north): Himalayan (HB), Lhasa (LB), Qiangtang (QB), Songpan–Ganzi (SB) and Kunlun–Qaidam–Qilian (KB) blocks. Separating all these structures there are at least four bordering sutures: Yarlung–Zangbo or Indus–Yalu Suture (IYS), Bangong–Nujiang Suture (BNS), Jinshajiang Suture (JS) and Ayimaqin–Kunlun–Mutztagh Suture (AKMS) (Yin and Harrison, 2000; Sherrington and Zandt, 2004; Zhu et al., 2013; Zhang and Santosh, 2012). The basement of the Lhasa Block is poorly exposed, but may consist largely of the Cambrian Amdo orthogneisses (Harris et al., 1988; Dewey et al., 1988) and perhaps also of older and more complex lithologies (Yin and Harrison, 2000; Kapp et al., 2003).

The Tibetan Plateau is commonly considered to be the archetypal collisional orogen; nevertheless, there have been a wide variety of suggestions for the age of initiation of the India–Asia collision, such as Late Cretaceous (Yin and Harrison, 2000), or mid-Eocene (Rowley, 1998), and even later as the end of the Eocene (Aitchison and Davis, 2001; Aitchison et al., 2003, 2007). The India–Asia collision, completed 45–40 million years ago, has been followed by a still active post-collisional convergence. The collision caused by the contact of the margin of Greater India with Asia at ~65 Ma is termed a "soft collision" (Lee and Lawver, 1995; Yin and Harrison, 2000; Chung et al., 2005) or "syn-collision" (Mo et al., 2007; Mo et al., 2008; Xia et al., 2009), whereas the collision that followed after ~45–40 Ma is termed a "hard collision" (Lee and Lawver, 1995; Chung et al., 2005) or "post-collision" (Mo et al., 2003, 2007, 2008).

2.2. North China Craton

The NCC is bounded on the south by the Qinling–Dabie–Sulu orogenic belt (Li et al., 1993; Meng and Zhang, 2000; Bai et al., 2007; Zhao and Zheng, 2009; Zheng et al., 2013), on the north by the Central Asian orogenic belt (Windley et al., 2007), on the west by northeastern Tibet and on the east by the Pacific Plate (Zheng et al., 2013). The NCC has been divided into the Archean to Paleoproterozoic Eastern and Western Blocks, separated by the Central Orogenic Belt, or the Trans-North China Orogen (Zhao et al., 2001a,b; Santosh et al., 2007a,b, 2009). Lithological, geochemical, structural, metamorphic and geochronological differences between the basements of the Eastern and Western Blocks and the Central Orogenic Belt have been summarized by Zhao and Zhai (2013, and references therein). The Western Block formed by the amalgamation of the Yinshan Block in the north and the Ordos Block in the south (Fig. 2) along the east–west-trending Inner Mongolia Suture Zone, incorporating the Khondalite Belt (Zhao et al., 2005; Santosh et al., 2007b; Santosh, 2010). The Eastern Block underwent Paleoproterozoic rifting event along its eastern margin at 2.2–1.9 Ga to form the Jiao–Liao–Ji mobile belt at ~1.9 Ga (Li et al., 2004; Luo et al., 2004; Li and Zhao, 2007).

The Qinling–Dabie–Sulu orogenic belt resulted from the Triassic continent–continent collision between the NCC and the Yangtze Craton (Li et al., 1993; Wu and Zheng, 2013) (Fig. 1c). The occurrence of diamond and coesite in the eclogites (Xu et al., 1992), the presence of coesite inclusions in zircons from both ortho- and para-gneisses (Liu et al., 2001a; Liu et al., 2001b), and the exsolution lamellae of clinopyroxene, rutile and apatite in garnets from the eclogites (Ye et al., 2000), all suggest that the upper and middle crustal units of the Yangtze Craton were once subducted under ultrahigh pressure conditions and then exhumed by deeper thrusts. This subduction and its subsequent collision with the NCC significantly affected the lithospheric mantle beneath the southern NCC. The melts derived from the subducted crustal materials fertilized the overlying lithospheric mantle (metasomatic lid) beneath the southern NCC, as documented from mantle xenoliths in the Mesozoic basalts of the region (Zhang and Sun, 2002; Zhang et al., 2002, 2004a,b; Fan et al., 2004; Chen et al., 2004b; Ying et al., 2006).

The Paleo Asian Ocean was present at the northern side of the NCC throughout the Paleozoic, with the Paleo-Tethys to the south (Dobretsov et al., 1995; Metcalfe, 1996, 2006). Several subduction zones were active during this interval, leading to continental growth through accretion of blocks along the northern margin of the craton and the generation of arc magmas (Davis et al., 1996; Yue et al., 2001; Davis et al., 2002; Xiao et al., 2003; Davis and Clague, 2006). The 8000 × 6000 km Central Asian Orogenic belt (CAOB), also referred to as the Central Asian Fold Belt (Windley et al., 2007; Xiao and Kusky, 2009; Kröner et al., 2014), Ural–Mongol Fold Belt, or the Altaids, is a complex collage of microcontinental blocks, island arcs, oceanic crustal remnants and continental marginal facies rocks developed between the Siberia Craton to the north and the Tarim and North China cratons to the south. It is one of the largest and most complex Phanerozoic accretionary orogenic belts on Earth, recording considerable juvenile crustal growth (Sengör and Burtman, 1993; Windley et al., 2002; Jahn et al., 2004; Windley et al., 2007; Xiao et al., 2009; Wilhem et al., 2012; Li et al., 2013c). The orogenic belt formed by multiple accretion and arc–continent collision events from the Early Neoproterozoic (ca. 1000 Ma) to the Permian, driven by the evolution and closure of the Paleo-Asian Ocean (Sengör and Burtman, 1993; Khain et al., 2002; Kovalenko et al., 2004; Windley et al., 2007; Xiao et al., 2008, 2009; Wilhem et al., 2012) (Fig. 1). Several aspects related to the contributions to lithospheric disruption (and evolution) of the NCC from its boundaries remain equivocal (Zhai et al., 2007; Zhu and Zheng, 2009; R.X. Zhu et al., 2012).

The Trans-North China Orogen is a Paleoproterozoic collisional suture dividing the NCC into the Eastern and Western Blocks (Zhao et al., 2001a,b; Gao et al., 2002; Faure et al., 2007). Some workers consider that these blocks collided at about 2.5 Ga and formed a 200 km wide orogen that included the development of a foreland basin on the Eastern Block, and a granulite-facies belt on the western block (Kröner et al., 1998; Kusky et al., 2001; Kusky and Li, 2003; Zhai and Liu, 2003; Kusky et al., 2004a,b; Polat et al., 2005, 2006), whereas others place this amalgamation as Paleoproterozoic (Zhai et al., 2007; Santosh, 2010; Zhai and Santosh, 2011; Zhao and Zhai, 2013). From two low velocity layers beneath the western NCC imaged by receiver functions, Zheng et al. (2009) postulated that the Trans-North China Orogen

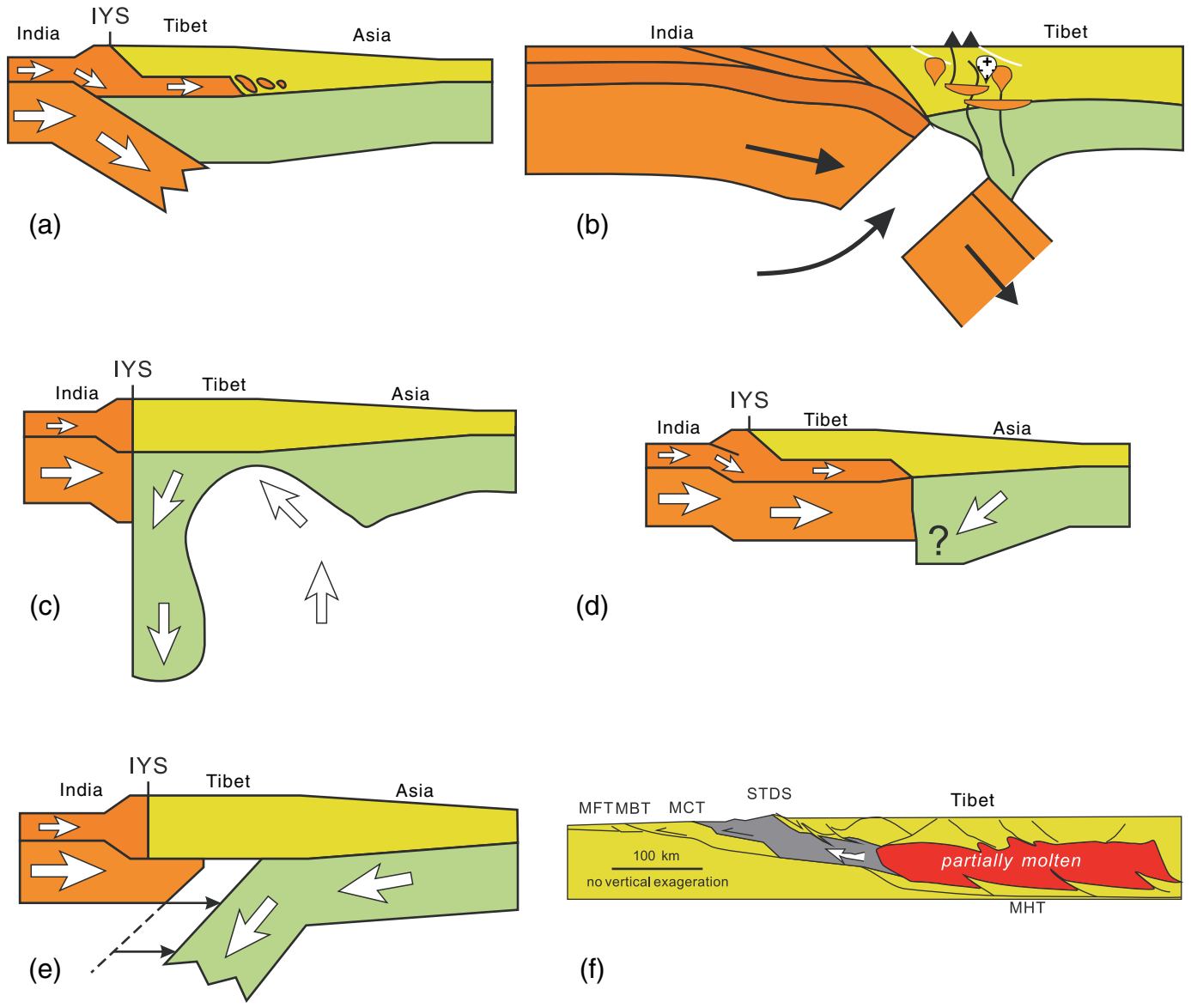

Fig. 2. Cartoon representation of the tectonic mechanisms for crustal thickening and uplift of the Tibetan Plateau: (a) injection model (Zhao and Morgan, 1984), (b) subducting Indian lithosphere broke off (Bousquet et al., 1997; Henry et al., 1997; Cattin et al., 2001; Mahéo et al., 2002; Tiwari et al., 2006; Hetényi et al., 2007; Zhang and Klemperer, 2010), (c) delamination of the thickened lithosphere (Houseman and Molnar, 1997; Kind et al., 2002; Zhang et al., 2009c, 2010b; Bai et al., 2010) to uplift the plateau interior; collision was followed by convective removal of the lithospheric mantle under Tibet (England and Houseman, 1988) (d) underthrusting of India (Argand, 1924; Powell and Conaghan, 1973); (e) subduction of Asian mantle and "roll back" of a south dipping subduction zone (Willett and Beaumont, 1994) or (f) channel flow (Beaumont et al., 2001, 2004; Klemperer, 2006; Zhang and Klemperer, 2010) of injected Indian upper crust to uplift the Himalaya as the main collision belt. IYS: Indus–Yarlung suture; MFT: Main Frontal thrust; MBT: Main Boundary thrust; MCT: Main Central thrust; MHT: Main Himalayan thrust; STDS: South Tibet detachment belt.

(TNCO) subducted westward beneath the western NCC. With the constraints of the double-vergent thrusts beneath the western and the eastern TNCO, Zhang et al. (2013c) inferred that the west and east NCC amalgamated along the TNCO with an opposite subduction polarity, by analogy with the closing of the rift between the western and the eastern NCC (Peng, 2010).

3. Mechanisms for the formation of the Tibetan Plateau and for the disruption of the North China Craton

3.1. Uplift mechanism: Tibetan Plateau

In the last three decades, many geological and geophysical investigations have been conducted in the Himalayan–Tibetan orogen, resulting in numerous syntheses dealing with both the active tectonics and the overall geological evolution of the system (Chang and Zheng, 1973; Dewey and Burke, 1973; Allègre et al., 1984; Hirn et al., 1984a,b; Molnar, 1984; Teng et al., 1985a,b; Xiong et al., 1985; Tapponnier et al., 1986; Dewey et al., 1988, 1989; Burchfiel and Royden, 1991; Harrison et al., 1992; Avouac and Tapponnier, 1993; Molnar et al., 1993; Zhao et al., 1993; Hsü et al., 1995; Nelson et al., 1996; Kong et al., 1997; Owens and Zandt, 1997; England and Molnar, 1998; Harrison et al., 1998; Xu et al., 1998; Fang, 1999; Larson et al., 1999; W.J. Zhao et al.,2001; Chen et al., 2004a; Zhang and Klemperer, 2005; Klemperer, 2006; Zhang et al., 2009c; Zhang and Klemperer, 2010; Zhang et al., 2010b; Zhao et al., 2010b; Zhang et al., 2011d,e,f). Based simply on geometric arguments, some geophysical studies have inferred (Kumar et al., 2006; Li et al., 2008; Nábělek et al., 2009; Kind and Yuan, 2010; Zhao et al., 2010b), that the Indian continental crust did not subduct beneath the Tibetan lithosphere. However, the present tectonic setting implies NNE-directed subduction of the Indian Plate, suggested also by the occurrence of syn-collisional calc-alkaline type

volcanism in southern and central Tibet. This magmatism requires some portion of the continental crust (either from the north or the south) to have been subducted into the mantle beneath Tibet, which has been confirmed by body and surface wave tomography results (Li et al., 2006), receiver function imaging (J.M. Zhao et al., 2010) and wide-angle seismic profiles (Zhang et al., 2011e). These geophysical studies indicate that the Tibetan crust is thick (~70–80 km) under the LB and becomes ~10–20 km thinner in the Qiangtang block (QB) and Songpan–Ganzi Block (SB) (Hirn et al., 1984a,b; Yuan et al., 1997; Braitenberg et al., 2000; W.J. Zhao et al., 2001; Kind et al., 2002; Tian et al., 2005a,b; J.M. Zhao et al., 2006; Chen et al., 2009b, 2010; J.M. Zhao et al., 2010; Chen et al., 2013). In addition to the prevailing strike-slip shears that developed around the plateau (Tapponnier et al., 2001), the presence of widespread north-striking normal faults in Tibet (Armijo et al., 1986; Molnar et al., 1993) reflect active east–west extension, contemporaneous with the rather uniform NNE-directed convergence rate of ~5 cm/year of the Indian Plate relative to stable Eurasia (Paul et al., 2001; Wang et al., 2001). Radiometric age data led to the conclusion that Tibetan east–west extension began diachronously, with the north-striking normal faulting initiated at ~18–14 Ma in the southern plateau (Coleman and Hodges, 1995; Williams et al., 2001) and at ~4 Ma in the north (Yin and Harrison, 2000). However, Blisniuk et al. (2001) reported that in the central QB of northern Tibet the normal faulting also started in the mid-Miocene (~13.5 Ma). In northern Tibet, Paleogene sedimentary basins, often associated with volcanism, are widespread.

A large amount of geophysical data generated through international collaborations have greatly advanced our understanding of the present-day lithospheric structure of the Tibetan Plateau. The INDEPTH project (Nelson et al., 1996), for instance, suggested the presence of a partially molten zone in the middle crust of southern Tibet. Subsequent investigations (e.g. Owens and Zandt, 1997; Yuan et al., 1997; Wei et al., 2001; W.J. Zhao et al., 2001; Zhang and Klemperer, 2005; Jiang et al., 2006a; Zhang and Klemperer, 2010; J.M. Zhao et al., 2010) repeatedly showed partial melts or aqueous fluids to be widespread in the Tibetan crust, despite the fact that volcanism is now active only in the northern plateau and that crustal xenolith data from the central QB (Hacker et al., 2000) do not support the presence of large quantities of melts or fluids. Galvé et al. (2002) and the INDEPTH III results (Haines et al., 2003a,b) indicate that underneath the QB there is no widespread zone of partial melting in the deep crust. Geophysical studies also reveal that the Indian lithospheric mantle has underthrust Asia as far north as the Bangong–Nujiang suture, in the southern plateau, and the Lhasa lithospheric mantle keel seems to be mostly absent (Bird, 1991; Owens and Zandt, 1997; Kosarev et al., 1999; Zhao et al., 2001c). In the north, where there is a thin but complex lithospheric lid beneath the QB and SB blocks (Kosarev et al., 1999; Kind et al., 2002), several of the values of the seismic parameters in the upper mantle are anomalous, all of which indicate unusually high temperatures (McNamara et al., 1995; Huang et al., 2000). A sharp Moho offset has been observed along the northern margin of the plateau, interpreted to imply a weak Tibetan crust that thickens vertically in response to the Indian penetration from the south, coupled with resistance from a more rigid crust in the Qaidam Block to the north (England and Houseman, 1985; Zhu and Helmberger, 1996, 1998).

Since Argand (1924) proposed that the Tibetan crust was thickened to double the normal crustal thickness with the superposition of the Indian and Asian crusts, numerous models have been put forward to explain the subduction of the Indian crust beneath Tibet to cause crustal thickening, including: (1) injection model (Zhao and Morgan, 1984, 1985); (2) subducting Indian lithosphere break off (Bousquet et al., 1997; Henry et al., 1997; Cattin et al., 2001; Mahéo et al., 2002; Tiwari et al., 2006; Hetényi et al., 2007; Zhang and Klemperer, 2010); (3) delamination of the thickened lithosphere (Houseman and Molnar, 1997; Kind et al., 2002; Zhang et al., 2009c; Bai et al., 2010; Zhang et al., 2010b) to uplift the plateau interior; (4) underthrusting of India (Argand, 1924; Powell and Conaghan, 1973); (5) subduction of Asian mantle and "roll back" of a south dipping subduction zone (Willett and Beaumont, 1994) or (6) channel flow (Beaumont et al., 2001, 2004; Klemperer, 2006; Zhang and Klemperer, 2010) of injected Indian upper crust to uplift the Himalaya as the main collision belt, and the lithospheric removal model to uplift the eastern margin of the plateau (Zhang et al., 2009c; Yin et al., 2010; Zhang et al., 2010b; Bai et al., 2011; Fu et al., 2011a,b; Hu et al., 2011, 2012) (Fig. 2). In order to interpret the generation of syn-collisional igneous activity, at least five different mechanisms have been proposed: (1) early crustal thickening followed by slip along a shallow dipping decollement (Himalayan leucogranites), (2) slab break-off during the early stage of the Indo-Asian collision (Linzizong volcanic sequence in southern Tibet), (3) continental subduction in southern and central Tibet, generating calc-alkaline magmatism, (4) formation of releasing bends and pull-apart structures that serve both as a possible mechanism to generate decompressional melting and as conduits to tap melts (Pulu basalts and other late Neogene–Quaternary volcanic flows along the Altyn Tagh and the Kunlun faults), and (5) viscous dissipation in the upper mantle and subduction of Tethyan flysch complexes to mantle depths, which may have been the fundamental cause of widespread and protracted partial melting in the Himalayan–Tibetan orogen during the Cenozoic.

Reconstructions of the shear-wave velocity (Vs) and density (ρ) structure of the crust and upper mantle (lithosphere–asthenosphere system) provide new insights in the understanding of the formation of the high Tibetan Plateau.

3.2. Disruption mechanism: North China Craton

According to seismic tomographic studies (Huang and Zhao, 2004; Chen et al., 2009a; Tian et al., 2009; Xu and Zhao, 2009), the NCC is still thick ($\geq$200 km) in its western part (Ordos), but becomes progressively thinned in its eastern part (varying from about 100 km to about 60 km). The cause of the lithospheric thinning is hotly debated, and many models have been proposed. It is generally accepted that the lithosphere of the eastern NCC was thinned significantly during the Mesozoic.

Menzies et al. (1993) suggested that destabilization of the cratonic lithosphere was initiated by the Indo-Eurasian collision, whereas Zheng et al. (2001) and Poudjom et al. (2001) proposed that the Archean cratonic lithosphere was replaced by young Phanerozoic lithosphere, resulting in the removal of the Archean lithospheric keel. The presence of both high- and low-magnesium olivines in spinel-facies peridotitic xenoliths entrained in the Hebi Cenozoic basalts (Zheng et al., 2001) supports such a replacement model. Menzies and Xu (1998) and Xu (2001) emphasized the importance of thermo-mechanical erosion from the base of the lithosphere and subsequent chemical erosion resulting from upwelling from the asthenosphere. Deng et al. (2004) suggested that this thermal erosion would have been related to the mantle plume activity and Chen et al. (2008) thought that this lithospheric removal was driven by subduction of the Pacific Plate. Niu (2005) suggested that water brought into the lithospheric mantle by the circum-craton subduction had an important effect on the Mesozoic lithospheric rheology. Several authors (Liu et al., 2004; Niu, 2005) have speculated that the lithospheric thinning (due to lithospheric weakening) uplifted the Tibetan Plateau, and led to mantle flow from western to eastern China, which initiated decompressional melting of the mantle to form widespread Cenozoic basalts in eastern China (Liu et al., 2004). An alternative model of lithospheric delamination, proposed by Wu et al. (2005) and Gao et al. (2004), proposes that lithospheric thinning was caused by delamination of the thickened lower crust and underlying lithospheric mantle. This model indicates that the Mesozoic volcanic rocks were derived from this delaminated lithosphere and the present lithospheric mantle is the newly accreted one (metasomatic lid). This dramatic lithospheric removal was initiated by Triassic continental subduction and subsequent collision, which resulted in the Dabie–Sulu high and ultrahigh pressure metamorphism (Xu et al., 1992; G.W. Zhang et al., 2004; Bai et al.,

2007). The lithospheric enrichment and transformation from refractory to fertile peridotites was probably a result of the lithospheric removal and massive injection of melts from recycled continental crust, as inferred from geochemical characteristics of Mesozoic basalts and their entrained olivine xenocrysts on the southern NCC (Zhang et al., 2002; Zhang and Sun, 2002; Fan et al., 2004; Y.J. Chen et al., 2004; Zhang et al., 2004a,b,c; Ying et al., 2006).

The major mechanisms proposed for the lithosphere disruption of the NCC are: (1) delamination (Deng et al., 2004; Wu et al., 2005; Deng et al., 2006; Wu et al., 2006; Windley et al., 2010); (2) thermal erosion (Menzies and Xu, 1998; J.P. Zheng et al., 2001; Zhang et al., 2003; Xu et al., 2004; Zhang et al., 2004a,b; J.P. Zheng et al., 2007; Xu et al., 2008); (3) peridotite–melt reaction (Zhang, 2005); (4) mechanical extension; and (5) hydration of lithosphere (Niu, 2005).

Taking account of the dynamic forces of the lithosphere destruction, there are also several debates on this issue as (1) the collision between Indian and Asian plates (Menzies and Xu, 1998; Liu et al., 2004); (2) the westward subduction of the Pacific Plate (Xu and Zhao, 2009; Zhu and Zheng, 2009), (3) a mantle plume (Xu et al., 2008; Peng, 2010; Lei, 2012), (4) the collision between North China (NC) and the Yangtze Plate at the southern margin of the craton (Zhang et al., 2005; Zhai et al., 2007), and (5) the collision between NCC and southern Mongolia at the northern margin of the NCC (Zhang et al., 2003; Zhai et al., 2007) and lower crustal flow (Zhang et al., 2012, 2013b), through the mechanisms of lithospheric delamination, thermal erosion, or both (Zhu and Zheng, 2009). The crustal-scale response to the disruption of the NCC still remains an open question (Zhang et al., 2012) and is explored here by means of crust/mantle structural imaging from ambient noise Rayleigh wave tomography.

4. Materials and methods

4.1. Description of data

4.1.1. Surface wave data in the plateau and surrounding region

Group velocity and Vs structure of the lithosphere–asthenosphere system were derived from long period seismic records of earthquakes that occurred during the period 1966–2007 in the Qinghai–Tibet Plateau and adjacent areas. The digital seismic stations of IC (NCDSN), G (Geoscope), XA (Bhutan), XR (INDEPTH II and III), YA (2003MIT-China), II/IU (GSN), YL (Himalayan Nepal Tibet Experiment) and KZ (Kazakhstan) made these data available, which have since been enriched by several earthquake records from some Indian stations, made available by S.S. Rai of NGRI. Seismic events with magnitudes greater than 5.0, focal depths of less than 300 km and epicenter-station distances greater than 1200 km are considered here using surface wave tomography (Fig. 3). The seismic stations and the focal mechanisms of the earthquakes are listed in Tables 1 and 2.

4.1.2. Gravity data in the Himalaya and Lhasa blocks

The gravity data used in this study are mainly $10' \times 10'$ gridded Bouguer anomalies (Braitenberg et al., 2003) based on the Chinese gravity network 85, with height reference to the Yellow Sea (Sun, 1989). In order to obtain data coverage over a rectangular grid, which of necessity goes beyond the Chinese border, the data were integrated with Bouguer anomalies derived from the IGG97L (Institute of Geodesy and Geophysics, CAS, Wuhan) Earth gravity model (Hsü and Lu, 1995). The Chinese gridded data were integrated with gravity data from the GRACE derived potential field (Shin et al., 2007), which has been combined with terrestrial gravity data (Fig. 4). In order to interpret gravity data in the HB and LB blocks, which have strong topographic undulations, a complete terrain correction was made (maximum radius of 166.7 km and density $\rho = 2.67$ g/cm^3). The major features of the regional Bouguer anomaly can be summarized as follows: (1) the Bouguer anomaly varies between −574 mGal and −247 mGal in the study area. The gravity data along seven ~1000 km long north–south oriented profiles give similar trends, with a value of ~−500 mGal for the Bouguer anomaly across southern and central Tibet decreasing southwards of the Himalaya; (2) a difference of about 330 mGal indicates large-scale structural variations not only in the crust but also in the upper mantle of the area; and (3) an extensive gravity low (32°N–34°N, 86°E–92°E) is located in the north-east of the study area in the QB, while four limited gravity lows are located in the LB, around (31°N 83°E), (30°N 86°E), (30°N 90°E) and (34°N 82°E), respectively.

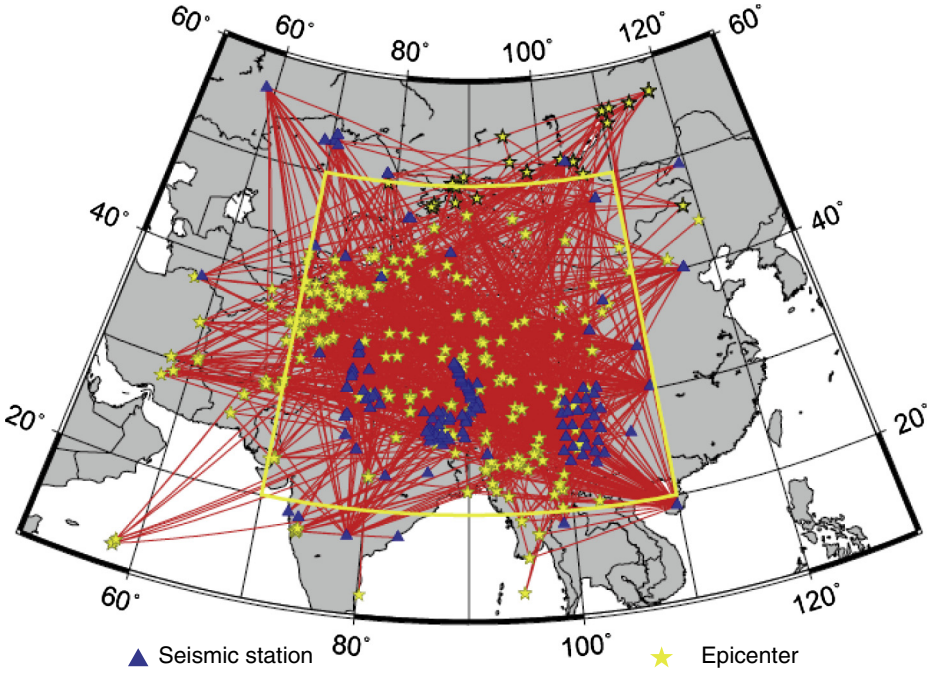

Fig. 3. The coverage of 791 ray paths (red curves) used in the study. The blue triangles are seismic stations. The yellow stars are epicenters.

Table 1
Codes of the seismic stations, which have recorded the events selected in the surface tomography.

Network	Stations code
G—GEOSCOPE	HYB, WUS
IC/CD—CDSN	BJI, CD2, ENH, GYA, HIA, KMI, LSA, LSA, LZH, PZH, QIZ, WMQ, XAN, YCH
II/IU—GSN	AAK, ABK, ARU, BRVK, CHTO, KURK, NIL, TLY, ULN
KZ—Kazakhstan	BRVK, BVAR, CHK, CHKZ, KKAR, KUR, KURK, MAKZ, MKAR, VOS, ZRN, ZRNK
NDI—India	ALB, BDI, BHT, BNK, BOK, BOM, CHD, DCH, DCL, GRG, HNL, JHN, KDG, KSL, KSP, KTH, KUL, LEH, LTA, NDI, NPL, NTL, POO, SHL, TKS, VIS
XA—Bhutan	CHUK, PARO
XR—INDEPTH II &III	BB05, BB08, BB10, BB14, BB18, BB20, BB23, BB34, BB36, DONG, LUMP, ST01, ST04, ST05, ST08, ST09, ST10, ST11, ST12, ST15, ST19, ST20, ST22, ST23, ST28, ST29, ST30, ST31, ST33, ST34, ST35, ST37, ST39, ST40
YA—2003MIT-China	MC01, MC02, MC03, MC04, MC05, MC06, MC07, MC08, MC09, MC10, MC11, MC12, MC13, MC14, MC15, MC16, MC17, MC18, MC19, MC20, MC21, MC22, MC23, MC24, MC25
YL—Himalayan Nepal Tibet Experiment	BIRA, BUNG, DINX, GAIG, HILE, ILAM, JANA, JIRI, MAZA, MNBU, ONRN, PHAP, PHID, RBSH, RUMJ, SAGA, SAJA, SIND, SSAN, SUKT, THAK, TUML

4.1.3. Ambient noise data in North China

Ambient noise data, used here in surface wave tomography, were obtained from a two-year seismic station observatory experiment in North China (Fang et al., 2009, 2010; Fang, 2010). The seismic experiment (NCSA) was carried out by the Institute of Geophysics, China Earthquake Administration, between November 2006 and November 2008. The aim of the experiment was to reconstruct the structure of the crust and upper mantle, in order to provide constraints for the validation of various mechanisms proposed for the disruption of the NCC lithosphere. In the experiment, 250 portable stations with an average station interval of about 35 km were deployed in North China. Continuous vertical-component seismograms, spanning the period from January 1, 2007, to February 28, 2008, recorded by 190 broadband stations and 10 very broadband stations, were used in this study (Fig. 5). The broadband stations were equipped with Guralp CMG-3ESPC seismometers (60 s to 50 Hz flat velocity response), while the very broadband stations were equipped with Guralp CMG-3 T seismometers (120 s to 50 Hz flat velocity response). The interstation paths ranged from 8 km to over 600 km (Fig. 6). Cross-correlations between all possible station pairs were made, which yields a total of $n * (n - 1) / 2$ possible station pairs (where n is the number of stations).

Fig. 7 shows an example of 14-month stacks of cross-correlations plotted as a record-section. The ray path density diagrams for the four selected periods considering cells of size of $0.25° \times 0.25°$ are shown in Fig. 8a–d. The general coverage is sufficient, except at the margins of the study region.

4.2. Methods

4.2.1. Surface wave tomography

Group velocity dispersion of the fundamental mode of Rayleigh waves was measured using the frequency–time analysis (FTAN) method of Levshin et al. (1992). In this study, a 2-D surface-wave tomography method (Ditmar and Yanovskaya, 1987; Yanovskaya and Ditmar, 1990) was applied to calculate lateral variations in the group velocity distribution for periods ranging from 8 to 150 s. The method does not require a priori parameterization. For each period, the group velocities are obtained as a function of position (latitude and longitude). In the procedure the travel time residuals are calculated along all paths with a reliable estimate of the resolution of lateral velocity variations. To reduce the effect of large errors, data with residuals greater than $3\times$ r.m.s. are rejected, and the procedure of tomographic reconstruction is repeated. Such selection is performed several times, until no large residuals remain in the data set. The group velocity values for each period before and after selection, the initial and the final r.m.s. residuals are listed in Table 2.

4.2.2. Ambient noise surface wave tomography

Once the daily cross correlations are computed, they are stacked to produce the final cross-correlation. The resulting cross-correlations are two-sided time functions with both positive and negative time coordinates, i.e., both positive and negative correlation lags. We typically store correlations from −1500 to 1500 s. These waveforms represent waves traveling in opposite directions between the stations (e.g. Lobkis and Weaver, 2001; Campillo and Paul, 2003; Shapiro and Campillo, 2004). If the sources of ambient noise are distributed homogeneously in azimuth, the causal and acausal signals will be identical. However, considerable asymmetry in amplitude and spectral content is typically observed, which indicates differences in both the source process and distance to the source in directions radially away from the stations. The two-sided signal can be compressed into a one-sided signal by averaging the causal and acausal parts, thereby enhancing the signal-to-noise ratio (SNR) (Bensen et al., 2007; Lin et al., 2007). Because measurements can be made between each station pair, this approach leads to high-resolution surface wave array tomography at short periods (e.g. Shapiro et al., 2004, 2005). Rayleigh wave group velocity dispersion curves and 2-D tomographic images were determined as in Section 4.2.1.

4.2.3. 3-D density structure inversion (crust and upper mantle)

The gravity stations are placed at their measurement heights above sea level, but the topography was not included in the model because its effect on the gravity attraction was already removed by the complete terrain corrections. Forward modeling of the Bouguer anomaly, essentially limited to the crust, was performed using the IGMAS software (Interactive Gravity and Magnetic Application System; see http://www.gravity.uni-kiel.de/igmas; Götze, 1984; Götze and Lahmeyer, 1988; Schmidt and Götze, 1998; Breunig et al., 2000). The 3-D structure is obtained in IGMAS by defining several vertical 2-D planes on which geological bodies are geometrically defined in the form of polygons (Schmidt, 1996). The 2-D vertical planes are connected via triangulation, thereby forming the 3-D structure. Hence, in order to perform detailed modeling, a large number of 2-D cross-sections must be included. S.F. Zhang (2010) described the details of the 3-D model construction in her Ph.D. thesis. The starting model of the ρ structure follows the geometry supplied by the controlled-source seismic experiments. The design of a 3-D ρ model in IGMAS requires three important assumptions: (1) the definition of the initial structure, (2) the selection of ρ values for the bodies forming the model and (3) the choice of a reference model. By iteratively changing the geometry of the initial structure in accordance with the available geophysical constraints a 3-D ρ structure is obtained that will be used in the subsequent fully 3-D inversion to a depth of 350 km.

In order to infer the deeper structure (lower crust and uppermost upper mantle), we used the program library GRAV3D, which is a suite of algorithms for inverting gravity data in 3D (Li and Oldenburg, 1996, 1998). The subsurface volume is modeled as a set of rectangular elements each with ρ anomaly. For forward calculations the anomalous ρ in each cell is known and the Bouguer anomalies are calculated. The inverse problem involves estimating the ρ contrasts of all the elements

Table 2
List of focal parameters for the earthquakes used in the surface tomography.

Event no.	Latitude (°N)	Longitude (°E)	Depth (km)	Mag.	Time (yyyy/mm/dd/hh:mm:ss.s)
1	29.92	69.62	26.0	5.4	1966/01/24/07:23:09.8
2	29.94	69.74	14.0	5.0	1966/01/24/15:32:51.0
3	17.30	73.85	29.0	5.0	1967/12/12/06:18:36.0
4	27.42	91.86	19.0	5.8	1967/09/15/10:32:44.2
5	17.33	73.91	27.0	6.2	1967/12/12/15:48:55.0
6	17.20	73.72	1.0	5.8	1967/12/11/20:49:46.0
7	17.34	73.96	33.0	5.5	1967/12/24/23:49:53.4
8	17.41	73.84	1.0	5.4	1968/10/29/10:00:00.8
9	17.51	73.92	30.0	5.1	1969/11/03/23:22:12.0
11	17.24	73.87	33.0	5.0	1980/09/20/07:28:58.0
12	17.26	73.64	19.0	5.2	1980/09/20/10:45:30.0
13	50.32	88.81	15.0	5.3	1986/11/04/16:19:18.4
14	50.84	89.22	15.3	5.4	1986/11/04/16:19:15.3
15	32.22	94.51	53.0	5.0	1986/11/22/20:59:53.0
16	41.77	81.48	15.0	5.9	1987/01/05/22:52:49.0
17	34.23	103.86	15.0	5.5	1987/01/07/18:19:09.1
18	41.26	79.31	15.0	6.3	1987/01/24/08:09:21.8
19	39.12	70.14	33.0	5.0	1987/02/23/00:21:21.1
20	38.08	91.16	35.6	5.7	1987/02/25/19:56:35.6
21	38.30	91.08	15.0	5.3	1987/02/25/19:56:36.4
22	41.30	79.52	33.0	5.1	1987/03/03/09:41:33.8
23	42.44	70.02	15.0	5.2	1987/03/26/11:56:55.8
24	41.74	69.88	57.7	5.1	1987/03/26/11:56:57.7
25	39.67	74.67	15.0	5.7	1987/04/30/05:17:37.1
26	24.58	93.94	75.3	5.9	1987/05/18/01:53:51.0
27	41.32	82.09	18.5	5.1	1987/08/05/10:24:18.5
28	29.30	83.77	34.0	5.2	1987/08/09/21:14:58.2
29	38.20	106.50	15.5	5.4	1987/08/10/12:12:15.5
30	37.57	105.63	21.3	5.1	1987/08/10/12:12:17.8
31	52.16	95.78	23.3	5.0	1987/09/16/17:57:23.3
32	47.24	89.69	15.0	5.6	1987/09/18/21:58:36.6
33	34.14	80.66	41.0	5.0	1987/09/27/06:12:41.0
34	36.59	71.97	98.2	5.9	1987/10/03/11:00:03.3
35	41.27	89.75	19.0	5.9	1987/12/22/00:16:39.1
36	39.01	75.50	36.7	5.4	1988/01/06/15:31:13.5
37	39.63	75.53	15.1	5.0	1988/01/06/15:31:15.1
38	38.90	71.01	15.0	5.3	1988/01/09/03:55:05.1
39	29.80	94.87	33.0	5.5	1988/01/25/01:12:22.0
40	24.05	91.66	42.7	5.8	1988/02/06/14:50:41.8
41	24.05	91.66	31.0	5.8	1988/02/06/14:50:42.7
42	30.41	68.10	15.0	5.0	1988/03/19/20:19:15.6
43	38.23	73.60	128.3	6.1	1988/03/26/22:58:41.5
44	41.99	85.68	55.0	5.6	1988/05/25/18:21:55.0
45	42.92	77.49	43.2	5.4	1988/06/17/13:30:43.2
46	33.49	89.38	40.3	5.0	1988/06/30/12:31:40.3
47	37.01	72.94	53.5	5.4	1988/07/20/06:20:53.5
48	48.88	91.04	18.0	5.8	1988/07/23/07:38:09.9
49	25.19	94.89	100.5	7.1	1988/08/06/00:36:24.6
50	39.82	74.20	15.0	5.2	1988/08/12/18:58:40.3
51	26.89	82.48	10.2	7.2	1988/08/20/23:09:10.2
52	26.52	86.64	34.7	6.8	1988/08/20/23:09:11.2
53	34.41	91.94	30.4	6.8	1988/11/05/02:14:30.4
54	34.17	91.70	15.0	6.2	1988/11/05/02:14:30.8
55	31.10	85.40	27.8	5.0	1988/11/07/02:20:27.8
56	23.38	99.42	15.0	5.3	1988/11/07/02:39:56.5
57	34.29	91.77	15.0	5.6	1988/11/25/22:29:41.1
58	39.72	71.56	15.0	5.5	1988/12/14/11:45:59.8
59	46.81	95.73	24.0	5.6	1988/12/15/06:40:52.0
60	49.88	78.82	40.1	6.0	1989/01/22/03:57:06.1
61	29.74	90.13	15.0	5.6	1989/02/03/17:50:01.9
62	36.25	80.85	0.0	5.0	1989/02/21/14:09:40.1
63	21.61	98.30	58.1	6.0	1989/03/01/03:25:07.8
64	24.25	91.71	33.0	5.2	1989/04/13/07:25:36.6
65	29.92	99.37	15.0	6.5	1989/04/15/20:34:11.7
66	30.00	99.69	15.0	6.3	1989/05/03/05:53:00.4
67	50.32	105.93	15.0	5.1	1989/05/13/03:35:02.7
68	35.69	91.65	15.0	5.0	1989/05/13/23:19:42.2
69	35.83	91.33	19.8	5.0	1989/05/16/22:15:19.8
70	22.13	89.88	15.0	5.7	1989/06/12/00:04:10.4
71	20.61	102.61	15.0	5.5	1989/06/16/20:12:31.3
72	29.79	99.54	15.0	5.6	1989/07/21/03:09:16.1
73	30.87	102.83	15.0	6.0	1989/09/22/02:25:53.5
74	20.32	99.06	15.0	5.8	1989/09/28/21:52:17.0
75	36.35	82.68	29.7	5.0	1989/10/08/15:49:29.7
76	21.62	93.89	44.6	5.2	1989/12/02/19:44:26.8
77	24.42	94.95	129.6	6.1	1990/01/09/18:51:28.9
78	36.56	70.84	113.5	6.4	1990/02/05/05:16:45.1
79	28.66	66.16	28.0	6.3	1990/03/04/19:46:22.1
80	37.04	72.85	17.5	6.5	1990/03/05/20:47:03.5
81	37.18	72.84	33.0	5.0	1990/03/06/18:07:06.1
82	39.04	73.09	22.0	5.4	1990/03/29/16:19:15.2
83	29.92	99.35	10.0	5.0	1990/04/08/19:13:49.6
84	39.29	74.78	15.0	5.2	1990/04/17/01:59:28.4
85	36.01	100.27	15.0	6.9	1990/04/26/09:37:14.3
86	35.44	70.09	113.1	6.0	1990/05/15/14:25:20.7
87	38.12	74.58	115.7	5.5	1990/05/17/13:21:07.3
88	32.20	93.28	15.0	5.6	1990/06/02/00:32:35.2
89	47.88	85.19	36.0	5.6	1990/06/14/12:47:28.3
90	26.75	65.25	15.0	5.8	1990/06/17/04:51:46.1
91	48.25	85.28	32.0	6.0	1990/08/03/09:15:04.1
92	47.96	84.96	33.4	6.2	1990/08/03/09:15:06.1
93	37.06	103.54	15.0	5.6	1990/10/20/08:07:30.5
94	43.79	83.99	15.0	5.6	1990/10/24/23:38:15.2
95	35.19	70.74	135.7	6.0	1990/10/25/04:53:46.5
96	43.18	78.24	15.0	6.4	1990/11/12/12:28:49.0
97	42.96	78.07	19.1	6.4	1990/11/12/12:28:51.5
98	40.62	73.41	32.0	5.0	1990/12/01/18:09:28.8
99	36.01	70.23	126.1	6.9	1991/01/31/23:03:34.9
101	40.34	79.20	15.0	6.0	1991/02/25/14:30:29.3
102	34.47	91.84	30.0	5.1	1991/02/26/15:38:42.0
103	15.81	95.57	16.0	6.0	1991/04/01/03:53:03.3
104	42.68	87.25	22.0	5.2	1991/06/06/08:02:06.1
105	35.99	84.74	24.0	5.0	1991/06/17/06:55:16.3
106	33.89	92.24	10.0	5.0	1991/08/10/20:21:51.5
107	46.03	85.41	54.8	5.7	1991/08/19/06:05:53.0
108	37.27	95.40	0.0	5.5	1991/09/02/11:05:56.6
109	54.68	110.70	32.6	5.1	1991/09/12/00:33:32.4
110	40.18	105.08	0.0	5.0	1991/09/14/13:16:37.7
111	30.22	78.24	15.0	6.8	1991/10/19/21:23:15.5
112	34.11	88.89	35.0	5.0	1991/12/14/08:20:24.5
113	33.91	88.81	34.0	5.2	1991/12/23/01:58:24.4
114	51.12	98.14	15.0	6.4	1991/12/27/09:09:36.9
115	35.13	74.45	103.4	5.3	1992/01/24/05:04:50.9
116	22.54	98.97	15.0	5.8	1992/04/23/14:18:37.9
117	22.44	98.90	12.0	6.1	1992/04/23/14:18:35.1
118	32.95	71.27	15.0	6.1	1992/05/20/12:20:35.0
119	24.03	95.93	17.3	6.3	1992/06/15/02:48:56.2
120	29.58	90.16	14.1	6.1	1992/07/30/08:24:46.6
121	29.46	90.30	15.0	5.7	1992/07/30/08:24:49.2
122	42.19	73.32	17.0	7.3	1992/08/19/02:04:36.5
123	37.35	71.86	131.2	5.8	1992/12/04/11:36:36.3
124	30.84	90.37	33.0	5.9	1993/01/18/12:42:07.8
125	29.08	87.33	12.2	6.2	1993/03/20/14:51:59.7
126	28.87	87.64	15.0	6.0	1993/03/20/14:52:01.0
127	36.35	70.59	209.6	6.3	1993/08/09/11:38:31.1
128	36.48	71.80	117.6	6.1	1993/09/18/05:02:27.2
129	38.16	88.82	15.0	6.1	1993/10/02/08:42:32.8
130	39.73	76.50	19.0	5.6	1993/11/30/20:37:12.9
131	24.80	97.40	15.0	6.1	1994/01/11/00:51:59.7
132	30.83	60.50	15.0	6.1	1994/02/23/08:02:05.3
133	30.59	60.44	15.0	6.1	1994/02/26/02:31:11.6
134	26.19	96.87	33.0	5.9	1994/04/06/07:03:27.6
135	25.62	97.05	15.0	5.9	1994/04/06/07:03:27.7
136	37.10	66.85	24.0	6.2	1994/05/01/12:00:37.0
137	32.57	93.67	9.5	5.9	1994/06/29/18:22:33.5
138	17.96	96.58	15.0	5.8	1994/08/19/21:02:45.0
139	56.76	117.90	12.3	6.0	1994/08/21/15:55:59.2
140	25.54	96.66	14.0	5.9	1994/11/21/08:16:34.0
141	24.98	95.29	118.0	6.4	1995/05/06/01:59:07.1
142	12.12	57.94	62.0	6.5	1995/05/26/03:11:17.1
143	51.96	103.10	11.6	5.8	1995/06/29/23:02:28.2
144	21.97	99.18	10.0	5.9	1995/07/09/20:31:31.4
145	36.43	70.39	223.0	6.2	1995/10/18/09:30:38.5
146	56.10	114.50	21.5	5.8	1995/11/13/08:43:14.5
147	48.44	88.14	17.0	5.6	1996/03/12/18:43:42.8
148	11.91	57.82	10.0	6.1	1996/03/28/07:28:28.0
149	40.77	109.66	26.0	5.5	1996/05/03/03:32:47.1

(continued on next page)

Table 2 (*continued*)

Event no.	Latitude (°N)	Longitude (°E)	Depth (km)	Mag.	Time (yyyy/mm/dd/hh:mm:ss.s)
150	30.15	88.19	33.0	5.6	1996/07/03/06:44:45.5
151	36.05	70.71	120.0	5.9	1996/09/14/08:01:03.7
152	12.43	58.07	10.0	6.4	1996/10/01/15:50:23.6
153	19.33	95.01	80.0	6.0	1996/11/11/09:22:27.7
154	24.50	92.64	50.0	5.3	1996/11/19/00:12:18.6
155	35.34	78.13	33.0	6.8	1996/11/19/10:44:46.0
156	41.03	74.28	22.0	5.9	1997/01/09/13:43:31.5
157	39.47	77.00	33.0	5.9	1997/01/21/01:48:30.1
158	37.66	57.29	10.0	6.5	1997/02/04/10:37:47.1
159	29.98	68.21	33.0	7.1	1997/02/27/21:08:02.3
160	30.14	68.02	33.0	5.9	1997/03/20/08:50:40.3
161	39.51	76.86	33.0	5.9	1997/04/05/23:46:19.5
162	39.54	77.00	33.0	6.0	1997/04/06/04:36:35.2
163	39.53	76.94	15.0	6.2	1997/04/11/05:34:42.7
164	39.63	76.99	23.0	5.8	1997/04/15/18:19:10.1
165	24.89	92.25	35.0	5.9	1997/05/08/02:53:14.7
166	36.41	70.95	196.0	6.4	1997/05/13/14:13:45.7
167	23.08	80.04	36.0	5.8	1997/05/21/22:51:28.7
168	33.94	59.48	10.0	5.9	1997/06/25/19:38:40.6
169	35.07	87.33	33.0	7.5	1997/11/08/10:02:52.6
170	22.21	92.70	54.0	6.1	1997/11/21/11:23:06.3
171	25.38	96.61	33.0	5.8	1997/12/30/13:43:18.6
172	41.08	114.50	30.0	5.8	1998/01/10/03:50:41.5
173	37.08	70.09	33.0	5.9	1998/02/04/14:33:21.2
174	36.30	71.00	221.0	5.5	1998/02/14/00:08:08.0
175	36.48	71.09	236.0	6.3	1998/02/20/12:18:06.2
176	30.15	57.61	9.0	6.6	1998/03/14/19:40:27.0
177	36.40	70.10	225.0	6.0	1998/03/21/18:22:28.0
178	24.93	95.31	122.0	5.5	1998/05/02/08:36:50.1
179	37.11	70.11	33.0	6.5	1998/05/30/06:22:28.9
180	30.13	88.17	33.2	5.8	1998/07/20/01:05:58.3
181	30.08	88.11	33.0	5.9	1998/08/25/07:41:40.1
182	39.66	77.34	33.0	6.3	1998/08/27/09:03:36.6
183	27.31	101.03	33.0	5.2	1998/11/19/11:38:14.8
184	41.67	88.46	23.0	5.9	1999/01/30/03:51:05.0
185	34.25	69.36	33.0	6.0	1999/02/11/14:08:51.0
186	51.60	104.86	10.0	6.1	1999/02/25/18:58:29.0
187	28.34	57.19	33.0	6.6	1999/03/04/05:38:26.0
188	55.90	110.21	10.0	5.8	1999/03/21/16:16:02.2
189	30.51	79.40	15.0	6.6	1999/03/28/19:05:11.0
190	30.09	69.44	33.0	5.3	1999/06/26/21:54:10.0
191	36.62	71.35	189.0	5.7	1999/06/29/23:18:05.0
192	36.52	71.24	228.0	6.5	1999/11/08/16:45:43.0
193	25.61	101.06	33.0	5.9	2000/01/14/23:37:07.9
194	38.12	88.60	33.0	5.5	2000/01/31/07:25:59.0
195	38.48	66.50	11.0	5.5	2000/04/20/08:41:29.0
196	26.86	97.24	33.0	6.4	2000/06/07/21:46:55.9
197	17.15	73.80	33.0	5.4	2000/09/05/00:32:46.0
198	54.64	94.95	33.0	5.6	2000/10/27/00:08:53.0
199	23.43	70.07	33.0	5.2	2001/01/26/07:32:33.0
200	23.51	70.52	10.0	5.8	2001/01/28/01:02:10.7
201	23.65	70.64	33.0	5.9	2001/01/28/01:02:15.0
202	29.52	101.13	33.0	5.7	2001/02/23/00:09:23.0
203	34.33	86.94	33.0	5.9	2001/03/05/15:50:07.0
204	11.95	80.23	10.0	5.5	2001/09/25/14:56:44.0
205	35.83	93.61	10.0	5.7	2001/11/18/21:59:53.0
206	35.97	69.17	33.0	5.9	2002/03/25/14:56:33.0
207	36.06	69.32	8.0	6.1	2002/03/25/14:56:33.8
208	38.53	73.41	117.5	5.4	2002/04/14/02:04:21.1
209	30.54	81.44	33.0	5.5	2002/06/04/14:36:05.5
210	30.80	69.98	33.0	5.8	2002/07/13/20:06:27.5
211	30.99	99.90	33.0	5.5	2002/08/08/11:42:05.2
212	35.41	74.52	33.0	6.4	2002/11/20/21:32:30.8
213	39.61	77.23	11.0	6.4	2003/02/24/02:03:41.4
214	37.53	96.48	14.0	6.4	2003/04/17/00:48:38.5
215	39.43	77.22	10.0	5.8	2003/05/04/15:44:35.5
216	34.61	89.48	17.7	5.8	2003/07/07/06:55:43.0
217	25.98	101.29	10.0	5.9	2003/07/21/15:16:31.9
218	22.85	92.31	10.0	5.6	2003/07/26/23:18:17.8
219	43.81	119.57	24.4	5.7	2003/08/16/10:58:42.8
220	29.58	95.61	33.0	5.6	2003/08/18/09:03:03.5
221	56.02	111.34	33.0	5.6	2003/09/16/11:24:55.7
222	50.04	87.81	16.0	7.3	2003/09/27/11:33:25.0
223	50.09	87.77	10.0	6.4	2003/09/27/18:52:46.9
224	50.21	87.72	10.0	6.7	2003/10/01/01:03:25.2

Table 2 (*continued*)

Event no.	Latitude (°N)	Longitude (°E)	Depth (km)	Mag.	Time (yyyy/mm/dd/hh:mm:ss.s)
225	49.95	88.21	10.0	5.5	2003/10/23/00:25:45.8
226	38.40	100.95	10.0	5.8	2003/10/25/12:41:35.2
227	50.20	87.60	10.0	5.7	2003/11/17/01:35:47.9
228	42.91	80.52	10.0	6.0	2003/12/01/01:38:31.9
229	29.00	58.31	10.0	6.6	2003/12/26/01:56:52.4
230	31.57	91.21	10.8	5.5	2004/03/07/13:29:45.2
231	45.45	118.17	15.8	5.7	2004/03/24/01:53:49.3
232	33.95	89.18	8.0	6.0	2004/03/27/18:47:29.2
233	36.51	71.03	187.1	6.5	2004/04/05/21:24:04.0
234	30.69	83.67	13.0	6.2	2004/07/11/23:08:44.1
235	12.46	95.00	22.4	5.8	2004/07/29/01:44:06.9
236	36.44	70.80	207.0	6.0	2004/08/10/01:47:32.8
237	30.96	81.08	9.6	5.3	2004/10/26/02:11:33.5
238	41.73	79.44	22.0	6.1	2005/02/14/23:38:08.6
239	30.49	83.66	11.0	6.3	2005/04/07/20:04:41.0
240	28.87	94.60	37.2	5.9	2005/06/01/20:06:42.7
241	43.05	109.00	10.0	5.5	2005/07/20/21:54:06.8
242	36.39	70.72	209.1	5.5	2005/07/23/14:40:25.0
243	27.72	87.42	54.9	5.0	2005/08/28/13:14:10.2
244	24.64	94.81	88.4	5.8	2005/09/18/07:26:00.3
245	34.73	73.10	8.0	6.4	2005/10/08/10:46:28.7
246	34.57	73.18	10.0	5.5	2005/10/08/12:08:28.1
247	34.79	73.14	20.3	5.9	2005/10/08/12:25:22.1
248	34.56	73.20	10.0	5.5	2005/10/09/07:09:19.0
249	34.87	73.13	10.0	5.6	2005/10/12/20:23:38.7
250	34.82	72.97	10.0	5.8	2005/10/19/02:33:29.8
251	34.81	73.04	10.0	5.6	2005/10/19/03:16:22.0
252	34.88	73.02	10.0	6.2	2005/10/23/15:04:21.3
253	34.74	73.06	10.0	5.6	2005/11/21/08:26:12.7
254	27.38	88.36	20.1	5.7	2006/02/14/00:55:23.8
255	27.01	91.67	10.0	5.5	2006/02/23/20:04:54.3
256	26.91	91.71	10.0	5.5	2006/02/23/20:04:53.5
257	34.87	73.79	10.0	5.5	2006/03/20/17:40:45.3
258	44.46	102.30	35.0	5.8	2006/04/30/00:43:14.7
259	45.39	97.35	9.0	5.8	2006/06/15/06:49:48.8
260	39.11	71.82	7.7	5.7	2006/07/06/03:57:51.2
261	44.19	83.47	23.5	5.4	2006/11/23/11:04:45.0
262	39.82	70.30	14.0	5.9	2007/01/08/17:21:49.7
263	37.71	91.81	10.0	5.5	2007/02/02/22:32:19.1
264	34.25	81.97	9.0	5.8	2007/05/05/08:51:39.0
265	31.41	97.79	33.8	5.6	2007/05/07/11:59:51.1
266	42.93	82.31	11.8	5.5	2007/07/20/10:06:52.7

based upon the available measurements of the Bouguer anomalies. The inversion is solved as an optimization problem with the simultaneous goals of: (1) minimizing an objective function on the model and (2) generating synthetic data that match observations to within a degree of misfit consistent with the statistics of the available data. The definition of length scales for smoothness controls the degree to which either of these two goals dominates. This is a crucial step and allows the user to incorporate a priori geophysical or geological information into the inversion. Explicit a priori information may also take the form of the upper and lower bounds on the ρ contrast in any cell.

The smoothness control takes the function of wavelength filtering that avoids the effect of superficial masses to be mis-interpreted as deeper residing masses (e.g. Braitenberg et al., 2000; Ebbing et al., 2001; Shin et al., 2009; Steffen and Lars, 2011).

An alternative conventional method for gravity inversion is to apply an inversion for ρ within a 3-D grid of small cuboidal elements (Li and Oldenburg, 1996, 1998). This approach has been extensively applied to upper crustal problems, however, applications to the lower crust and upper mantle have been limited (Welford and Hall, 2007; Welford et al., 2010; Brandmayr et al., 2011). Despite being less popular than the shallow-modeling approach, due to neglecting the sphericity, this approach can be used to model simultaneously ρ variations within the crust and mantle, and by proxy to model the Moho geometry. Intelligent mesh design and sensible regularization procedures permit reasonable resolution of the Moho surface, while allowing ρ variations within the crust and mantle to be modeled as part of the

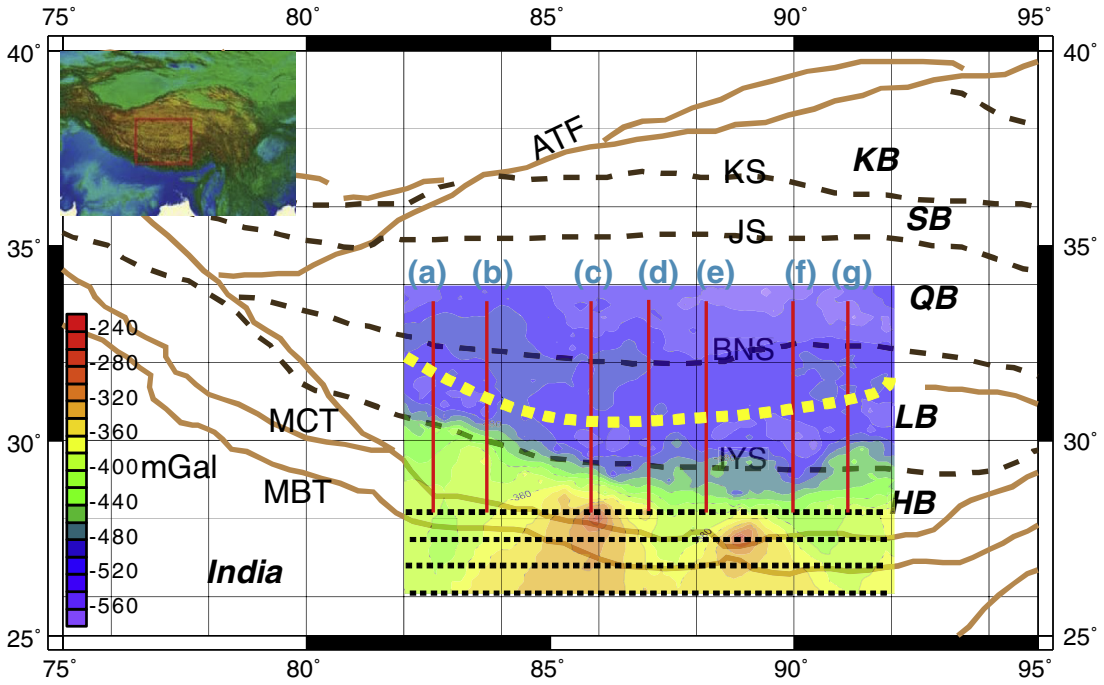

Fig. 4. Bouguer anomaly data in central-south Tibet (color scale in mGal). In the blow up of the red rectangle traced in the geographic map in the upper left corner, black dotted lines mark the area where terrestrial gravity data are not available and the yellow curve connects a series of gravity lows, which are located above the supposed northern margin of the Indian Plate. Brown lines indicate MBT: Main Boundary thrust; MCT: Main Central thrust; ATF: Altyn Tagh Fault. Dashed lines indicate IYS: Indus–Yarlung suture; BNS: Bangong–Nujiang suture; JS: Jinshajiang suture; KS: Anyimaqen–Kunlun–Mutztagh suture; HB: Himalayan Block; LB: Lhasa Block; QB: Qiangtang Block; SB: Songpan–Ganzi Block; KB: Kunlun–Qaidam Block.

same procedure (Welford and Hall, 2007; Welford et al., 2010). The t?>full 3-D nature of this approach and the requirement for a large number of elements in the vertical direction, means that this method is more computationally demanding than other methods, thus its application to very large scales requires significant computational resources and time. Considering furthermore the inherent non-uniqueness of the inversion problem, it is therefore natural to use the reliable part of the crustal inversion as a constraint for the inversion involving the mantle down to 350 km (see e.g. Mueller and Panza, 1986).

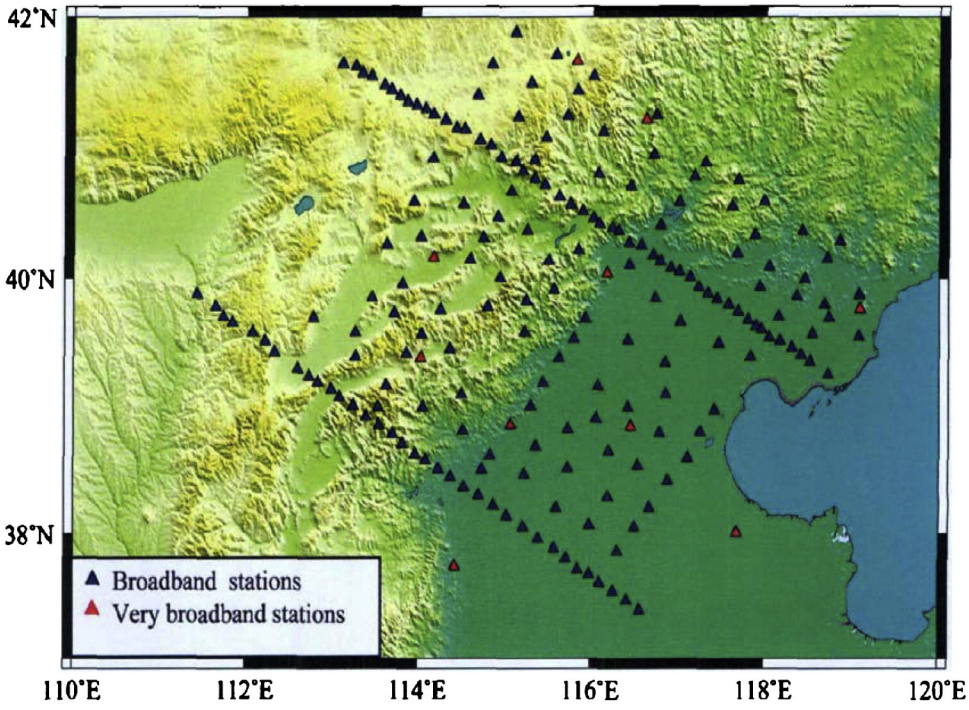

Fig. 5. Station distribution for the ambient noise study in NCC. Black triangles denote broadband seismic stations; red triangles very broadband stations.

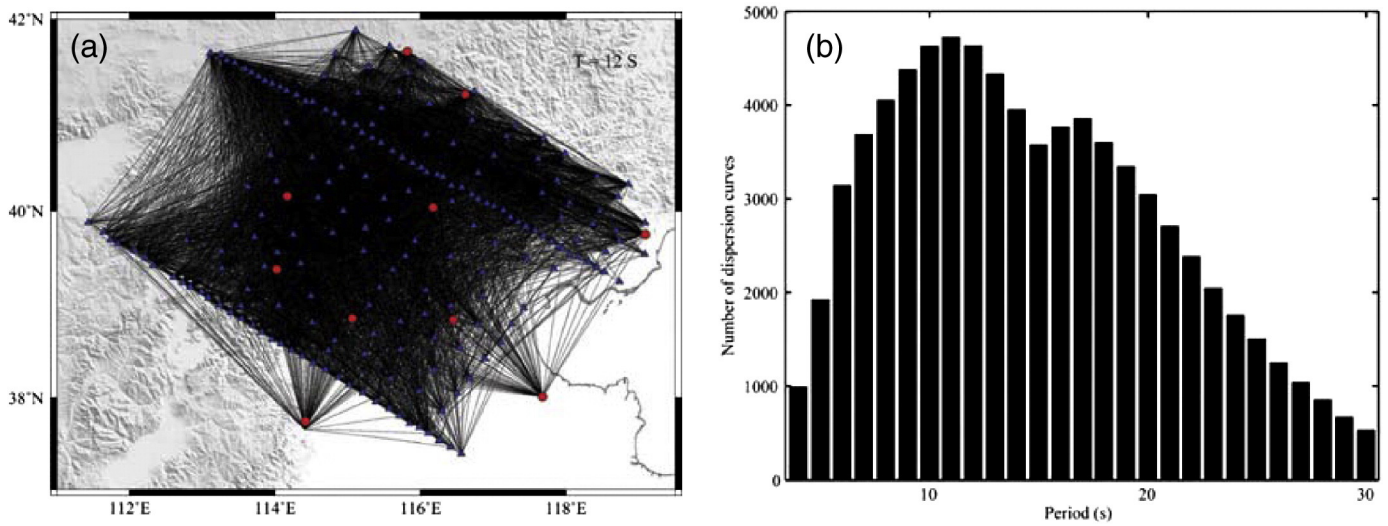

Fig. 6. The interstation path lengths range from 8 km to over 600 km. Cross correlations between all possible station pairs were made, which yields a total of n ∗ (n − 1) / 2 possible station pairs (where n is the number of stations) that can be used in the ambient noise study.

5. New development of crust/mantle structure imaging in the Tibetan Plateau and North China Craton

5.1. Lithosphere–asthenosphere shear wave velocity structure of the plateau

In the group velocity maps of surface wave tomography (X.M. Zhang et al., 2007; X.M. Zhang, 2010), the most conspicuous low group velocity anomaly, in the range 25 to 40 s, appears in the whole Qinghai–Tibet Plateau, whereas the Indian Plate and the Yangtze Craton are characterized by high group velocity anomalies. At intermediate periods (50–80 s) the most dominant characteristic is the NW–SE directed low velocity anomaly in the Qinghai–Tibet Plateau. At long periods (100–150 s) the velocity anomaly is comparable with the anomaly at lower periods, which is consistent with the findings of previous studies (e.g. Y. Chen et al., 2009; Chen et al., 2010). On account of the complexity of the study area we use absolute surface wave tomography, properly accounting for most of the recent caveats on tomographic images (Foulger et al., 2013).

The representative crust–upper mantle Vs models were chosen by LSO (Boyadzhiev et al., 2008) in 181 cells with dimensions 2° by 2°, in which dispersion relations have been non-linearly inverted (Panza, 1981 and references therein). We performed fully non-linear inversion in order not to miss unknown, but detectable, characteristics that could not be explored using a linear search. The hedgehog non-linear inversion scheme has been parameterized taking into account the resolving power of the considered data as, for instance, in Knopoff and Panza (1977), Panza (1981), and Panza et al. (2007a,b). X.M. Zhang (2010) displays the final shear wave velocity models beneath the cells in the Tibetan Plateau and its neighboring areas. The main features detected are discussed below.

Beneath the Ganges catchment, to the south of the Qinghai–Tibet Plateau, we observe that there is a relatively low velocity lower crust with an average Vs of about 3.65 km/s. Beneath the Moho, a fast lid with a Vs of about 4.7 km/s reaches a depth of about 180 km. Regional Rayleigh wave group velocities (Mohan et al., 1997) also show a high-velocity upper mantle in this area. The asthenosphere is thin with Vs of about 4.50 km/s in the region. To the south of the Ganges drainage area, the lithosphere is also thinner. In the Indus drainage area, we can observe high velocity lower crust of about 3.80 km/s. Near the Himalaya Block (HM), the lithosphere reaches a depth of about 165 km and a relatively slow lid, with a velocity of about 4.45 km/s. In the north Indus drainage area, a lid with a Vs value of about 4.65 km/s overlies an ~90 km thick metasomatic lid with Vs of about 4.50 km/s. In the Ganges drainage area, the lid reaches a depth of about 180 km with average Vs of ~4.60 km/s. There is a relatively thin lower velocity anomaly that sits on a metasomatic lid, with Vs ~ 4.50 km/s. To the south of the Ganges drainage area, the lithosphere (Vs approximately 4.65 km/s)

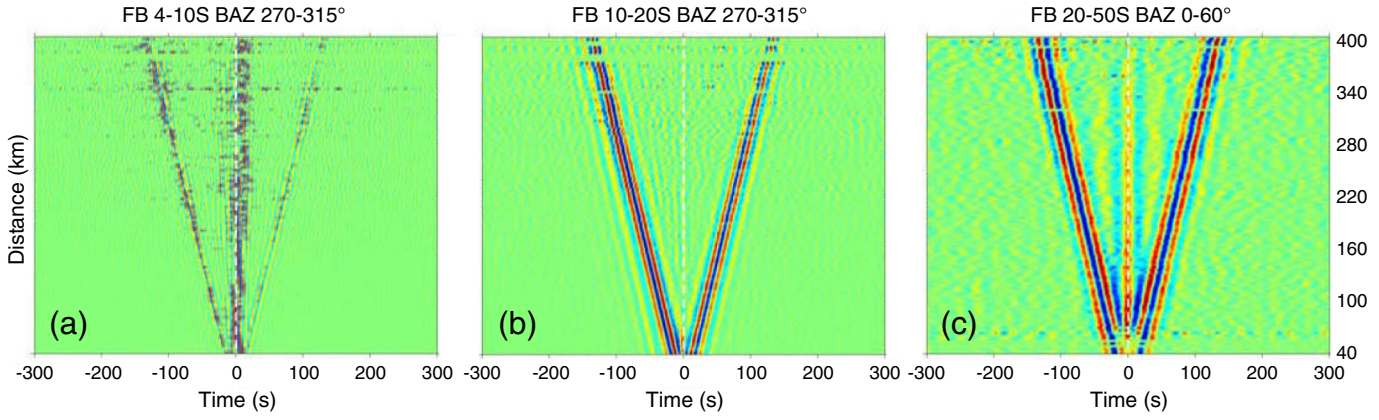

Fig. 7. Example of 14-month stacks of cross-correlations plotted as a record-section.

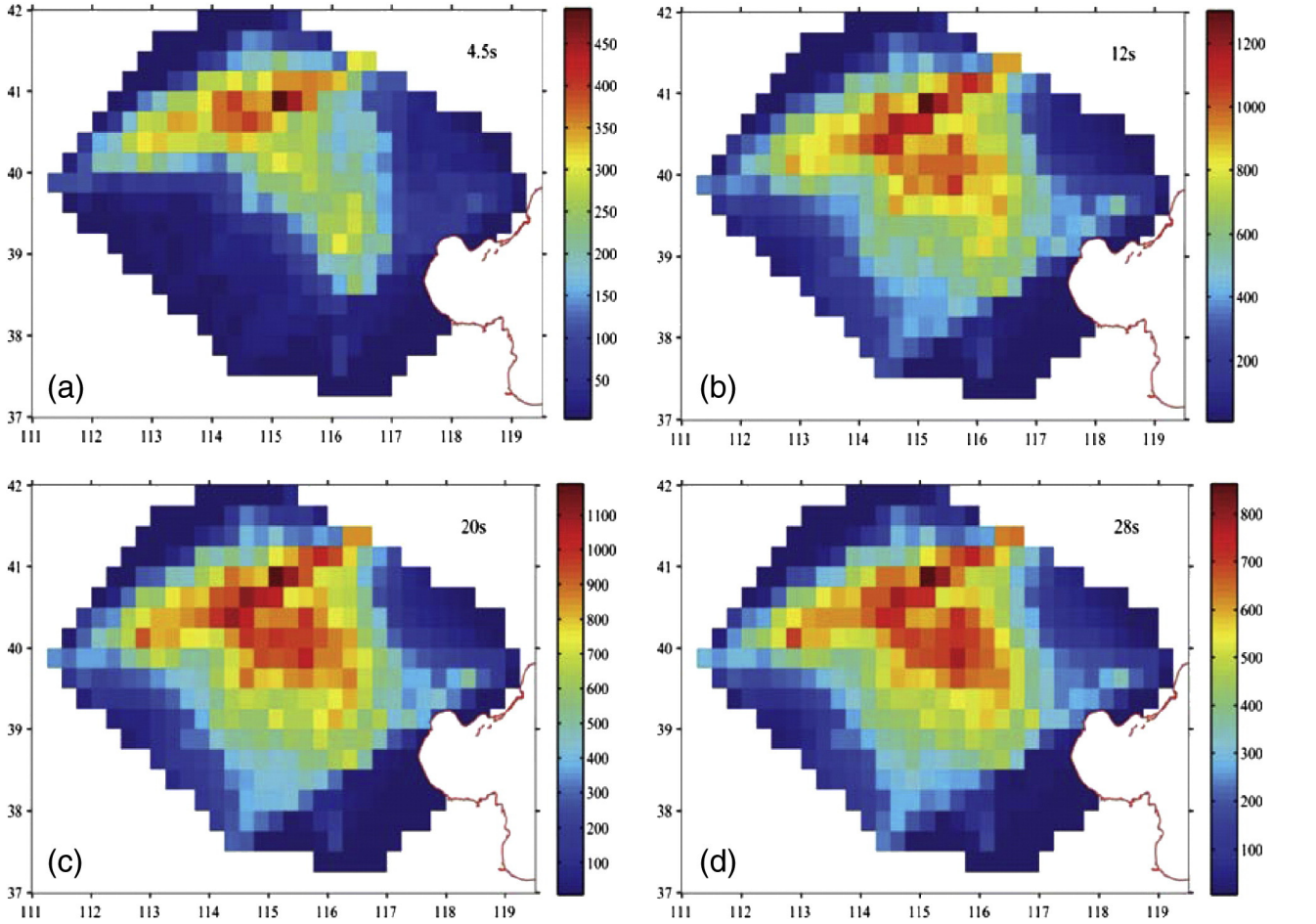

Fig. 8. The ray path density diagrams for the four selected periods (a) 4.5 s; (b) 12 s; (c) 20 s; (d) 28 s for cells of size 0.25° × 0.25°. The general coverage is sufficient, except at the margins of the study region (blue areas). The color scale represents ray path density.

reaches a depth of about 175 km, while between the Himalayan mountains and Nage Hill, the lid has a Vs of about 4.50 km/s and extends to a depth of about 160 km. The Burmese arc lies on the eastern margin of the Indian plate, marked by the Indo-Burman mountain ranges. Near the Bay of Bengal, a relatively low velocity (Vs ~ 2.83 km/s) upper crustal layer reaches a depth of about 8 km. Under the lower crust the Mohorovicic discontinuity reaches a depth of about 39 km. With a fast lid (Vs ~ 4.70 km/s) the bottom of the lithosphere extends to a depth of about 160 km, overlying a high-velocity asthenosphere layer with a Vs of about 4.60 km/s. Along the Yarlung Zangbo suture belt (IYS), the lid (metasomatic?) in the depth range ~80–165 km is relatively slow (Vs ~ 4.45 km/s) and it overlies an asthenosphere with a Vs of about 4.40 km/s, which extends to a depth of about 255 km. Further to the north, the Moho is deeper than 40 km. At Nage Hill the crustal thickness is about 43 km, and a fast lid with a Vs of about 4.70 km/s overlies a low velocity asthenosphere (Vs ~ 4.20 km/s), which reaches a depth of about 240 km. East of Nage Hill the lower crust, with a high Vs of about 3.85 km/s, overlies a very low velocity uppermost mantle (Vs ~ 4.25 km/s). At the bottom of the lithosphere, the asthenosphere, with Vs ~ 4.50 km/s, reaches a depth of about 260 km. Further to the north, the Mohorovicic discontinuity reaches a depth of about 44 km above a very slow layer (Vs ~ 4.1 km/s), which reaches a depth of about 75 km. Under a lid with Vs of about 4.65 km/s, a low velocity asthenosphere (Vs ~ 4.35 km/s) can be detected, reaching a depth of about 260 km.

The Southern Burmese arc is characterized by the velocity of the sub-Moho layer of about 4.55 km/s and the lithospheric thickness is about 150 km. To the east, in the Red River zone, it appears that there is no high velocity lid. The bottom of the lithosphere is at a depth of about 130 km, with an average lid velocity of ~4.50 km/s), overlying a slow asthenosphere (Vs ~ 4.30 km/s) which extends down to a depth of around 255–265 km.

We now consider in some detail the main properties of the cellular models. In cell B17 the bottom of the lithosphere reaches a depth of about 130 km with a relatively low velocity lid, which overlies an asthenosphere with Vs ~ 4.25 km/s. More to the east, cell B18 has the asthenosphere, with Vs ~ 4.40 km/s and extends to a depth of about 270 km.

To the east of the Jinshajiang suture fault (JS), near the Yangtze Craton, in cell D16, at the bottom of the lithosphere, with Vs ~ 4.60 km/s, the asthenosphere (Vs ~ 4.55 km/s) is detected, which extends to a depth of about 270 km. Further to the east, the Mohorovicic discontinuity is at a depth of about 60 km in cell E15. The cell E16, which is located among three faults: the Xianshuihe Fault, the Longmenshan Fault and the Xiaojiang Fault, has a crustal thickness of around 57 km. Below the low velocity (Vs ~ 4.25 km/s) uppermost mantle, the lithosphere reaches a depth of about 157 km (Vs in the lid ~4.55 km/s), overlying the asthenosphere (Vs ~ 4.45 km/s) which extends down to a depth of about 280 km.

The Himalayan Block (HM) has a complex structure of crust and mantle. In cells D05, D06 and D07, south of the Himalaya Block (HM), the lithosphere reaches a depth of about 160 km with a fast lid (Vs ~ 4.65 km/s). Under the lithosphere the asthenosphere (Vs ~ 4.50 km/s) extends down to a depth of about 250 km. Further to the east, in cells D08, D09, D10 and D11, the lithospheric thickness of about 150 km in cells D06, D07, D08 and D09 is slightly less than the thickness of about 160 km in cells C06, C07, C08 and C09. In cells D06, D07, D08, D09, D10 and D11 the velocity in the lid is about

4.6 km/s. At the bottom of the lithosphere a low velocity asthenosphere, with variable thickness from 90 to 140 km, with a Vs ~ 4.45 km/s, is detected. In the west of the Himalaya Block (HM), in cells E04 and E05, the lithosphere reaches a depth of about 155 km, and a fast lid, with Vs ~ 4.65 km/s can be seen in the depth range from ~85 to ~155 km. The asthenospheric thickness is about 90 km with Vs ~ 4.45 km/s. Further to the west in cells F03 and F04, a Vs of about 4.15 km/s, overlies a relatively fast lid with Vs ~ 4.65 km/s. The lithospheric thickness reduces slightly from 160 km in cell F03 to 150 km in cell F04. A relatively high velocity asthenosphere with Vs of about 4.50 km/s is seen in cells F03 and F04. To the west of the Himalaya Block (HM), in cells G02 and G03 the uppermost mantle layer with a Vs ~ 4.30 km/s overlies a lid with Vs ~ 4.50 km/s, down to a depth of about 155 km in cells G02 and G03. In cell G03, the lithosphere overlies a low velocity asthenosphere with an average Vs ~ 4.30 km/s, which reaches a depth of about 270 km. Further to the south, in cells E06 and E07 the fast lid reaches a depth of about 150 km, with Vs ~ 4.60 km/s. The asthenospheric thickness is about 100 km with Vs ~ 4.45 km/s. South of the Yarlung Zangbo suture belt (IYS), in cells E08, E09 and E10, the lithosphere reaches a depth of about 150 km, and the asthenosphere (Vs ~ 4.40 km/s) has a thickness of about 130 km. In cell E09 the asthenosphere reaches a depth of about 300 km, with Vs ~ 4.45 km/s. Cell E10, in the Lhasa Block (LS), has an asthenosphere as thick as about 120 km.

The eastern Lhasa Block (LS), to the east of 90°E, has a deep structure which is different from that of the western one. INDEPTH (Zhao et al., 1993; Nelson et al., 1996) shows that the crust is double-thickened with the Moho estimated to be at a depth greater than 70 km. In cell E13 the Vs in the lid is as high as about 4.80 km/s in the depth range 80–135 km. Below the Moho the bottom of the lithosphere reaches a depth of about 145 km in cells E11 and E12. The underlying asthenosphere has a relatively high average Vs of ~4.45 km/s. The lithosphere is slightly shallower in cell E13, where it reaches a depth of about 135 km and overlies an approximately 150 km thick asthenosphere (Vs ~ 4.55 km/s).

Further to the north, cells F05, F06, F07, F08, F09 F10, F11, F12 and F13 have a crust as thick as about 80 km. The bottom of the lithosphere reaches a depth of about 150 km, and overlies the asthenosphere with Vs ~ 4.50 km/s, which extends to a depth of about 275 km in cell F05. In cell F06 the asthenosphere (Vs ~ 4.50 km/s) extends to a depth of about 315 km. Further to the east, cells F07, F08, F09, F10, F11, F12 and F13 have Vs in the range 3.05–3.25 km/s at depths in the range 16–32 km. The results from surface wave and body wave tomography (Ding et al., 2001) also show that there are remarkable low velocity zones in the upper crust of the Lhasa Block (LS). The middle crust of Tibet has a high temperature and a low velocity (Nelson et al., 1996), which favors lateral crustal flow (Beaumont et al., 2001, 2004; Clark and Royden, 2000; Sun et al., 2004; Zhang and Klemperer, 2005; Shapiro et al., 2004; Y. Chen et al., 2009). There is a slow lower crust (Vs ~ 3.65 km/s) that starts at a depth of about 47 km and reaches a depth of about 75 km in cells F07, F08 and F09. In cells F10, F11 and F12 the lower crust have an average Vs ~ 3.65 km/s in the depth range 50–80 km. In particular, in cell F13 the Vs is about 3.50 km/s in the lower crust, which reaches a depth of about 80 km. Below the slow lower crust, a fast lid as thick as about 65 km, with a Vs ~ 4.65 km/s, reaches the bottom of the lithosphere, which extends down to a depth of about 140 km in cells F07 and F08. The asthenosphere (Vs ~ 4.50 km/s) reaches a depth of about 300 km. In cells F09 and F10 the lithosphere is slightly thinner, to a depth of about 130 km, and the lid, with a Vs ~ 4.70 k m/s, can be observed in the depth range 75–130 km, overlying an approximately 160 km thick asthenosphere, with a Vs ~ 4.50 km/s. To the east of cell F10, a 140 km thick lithosphere is detected in cell F11, with a fast lid (Vs ~ 4.75 km/s) overlying an ~155 km thick asthenosphere (Vs ~ 4.55 km/s). Similarly, cells F11, F12 and F13 have a fast lid with a Vs ~ 4.70 km/s. Under the lithosphere, a 160 km thick asthenosphere with an average Vs ~ 4.45 km/s is observed. In cells F12 and F13, a relatively low velocity layer (Vs ~ 4.35 km/s) may be seen between about 230 and 310 km.

To the east, in cells F14 and F15, the lithosphere is relatively thin (~145 km thick) and overlies an approximately 140 km thick asthenosphere, with an average Vs ~ 4.50 km/s. To the north, the Mohorovicic discontinuity in the western SB block (cells G14 and G15) reaches a depth of about 72 km. In cells with a fast lid (average Vs ~ 4.70 km/s) the lithosphere reaches a depth of about 160 km, and overlies a high velocity asthenosphere (average Vs ~ 4.55 km/s), which extends down to an average depth of about 270 km.

Further to the east, the lithosphere extends to an average depth of about 155 km and overlies an approximately 125 km thick asthenosphere. To the east, a lithosphere reaching a depth of about 165 km overlies an asthenosphere that reaches a depth of about 275 km.

To the east of the western syntaxes of the India–Eurasia collision zone, cells G04 and G05 have a complex crust–mantle transition. below the Mohorovicic discontinuity, a fast lid with Vs ~ 4.70 km/s is seen, reaching a depth of about 155 km, overlying the asthenosphere (Vs ~ 4.50 km/s), which extends to a depth of about 345 km. In the western QB Block (QT) (cells G06, G07, G08 and G09) the Moho reaches a depth of about 80 km. The tomographic results (Ding et al., 2001; Yao et al., 2005, 2006) indicate the presence of a prominent low velocity anomaly lying mainly in the lower crust and uppermost mantle in the QB. The tomographic cross-section (Wittlinger et al., 1996) reveals that the crust of the QB Block appears to be thick (~70 km) with a low velocity. Similar to cells F09 and F10, below the thick crust in cells G06, G07 and G08, the fast lid, with a Vs ~ 4.70 km/s, is relatively thin (about 50 km), and reaches a depth of about 130 km. A relatively thin lithosphere (with thickness of about 125 km) is seen in cells G08 and G09. Below the thin lithosphere a metasomatic lid as thick as about 100 km, with a Vs in the range ~ 4.35–4.50 km/s, extends to a depth of about 250 km and overlies the Indian lithosphere in cells G06, G07, G08 and G09. To the eastern part of the QB Block (cells G10, G11, G12 and G13), the lithosphere with a 70–80 km thick lid (Vs ~ 4.65 km/s) becomes thicker and reaches a depth in the range 145–155 km. This result is in good agreement with that of Sun et al. (2004). Below these depths an approximately 100 km thick metasomatic lid is present, with a Vs ~ 4.5 km/s. In cells G11, G12 and G13 the asthenospheric thickness is thinner than in the western QB Block (QT) and reaches an average depth of about 305 km.

Near the western syntaxes of the India–Eurasia collision zone, cells H03 and H04 have a crust about 75 km thick. To the west, in cells H03 and H04, the lithospheric thickness is about 170 km, with a lid Vs velocity in the range 4.50–4.55 km/s. Similar to that detected in cells F09 and F10 of the western QB Block (QT), below the lithosphere a developed asthenosphere with a low velocity of about 4.45 km/s extends to a depth of about 345 km in cells H03 and H04.

To the north of the QB, the Bayankla Block (BK) (cells H05, H06, H07, H08 and H09) has a thick crust of about 75 km and a thin lithosphere, with a thickness of about 150 km. In cell H05, between the Tarim Basin (TRM) and the Qinghai–Tibet Plateau, a fast lid with a Vs ~ 4.65 km/s reaches a depth of about 150 km; at greater depths the Vs is about 4.60 km/s. Compared to the lithospheric thickness of the cells in the QB Block, the lithosphere is thicker in cells H06, H07, H08 and H09. At the bottom of the lithosphere a metasomatic lid, with a thickness of approximately 100 km and an average velocity of about 4.45 km/s, is present on top of the Indian subducted lithosphere.

In the western Qinghai–Tibet Plateau in cells H01, H02, I01 and I02, the Moho has a depth of about 72 km. In cells G01, H01, H02, I01, I02 and J02, the lithosphere is relatively thick (~170 km). Similar to that seen in the QB, in cells H02, I02 and J02, under the lower crust a fast lid with Vs ~ 4.75 km/s is observed. Below the bottom of the lithosphere a positive velocity gradient is detected, with an average Vs ~ 4.55 km/s, at an average depth in the range 170–270 km in cells H01, H02, I01 and I02.

To the south of the Qaidam Basin (QDM), in cells H10 and H11, the lithospheric thickness is about 160 km, thicker than that observed in the southern cells G10 and G11. Under a fast lid (Vs ~ 4.70 km/s) there may be a metasomatic lid (Vs ~ 4.50 km/s) down to a depth of about 250 km. Moving to the east, in cells H12 and H13, the uppermost mantle has a low velocity layer, with a Vs ~ 4.30 km/s, on top of a fast lid with a high velocity of about 4.80 km/s, which extends to a depth of about 160 km. Under the high velocity lithosphere of cell H13, the shear velocity is about 4.60 km/s and may correspond with the metasomatic lid. Moving to the east, a layer of quite low velocity is detected in the uppermost mantle, with a Vs ~ 4.10 km/s in cells H16 and H17 on top of a fast lid with an average Vs ~ 4.75 km/s in cells H15, H16 and H17. The asthenosphere (Vs ~ 4.45 km/s) reaches a depth of about 290 km.

To the northeast, the first deep seismic sounding experiment in the Qaidam Basin was carried out in 1958 (Zeng and Gan, 1961). The studies revealed that the crust is about 52 km thick in the basin and that a low velocity anomaly zone exists in the crust. Below the Moho, a fast lid (Vs ~ 4.70 km/s), reaching a depth of about 160 km, is observed in cells I09, I11, I12 and I13. In cell I10, below the Mohorovicic discontinuity, the velocity of the lid at depths in the range 80–160 km is about 4.55 km/s. Under the lithosphere, there is a metasomatic lid, with a Vs ~ 4.50 km/s, which extends to a depth of about 250 km in cells I09, I10 and I11, and overlies the subducting Indian lithosphere. Further to the east, below the Mohorovicic discontinuity, a low velocity uppermost mantle layer, with a Vs ~ 4.20 km/s overlies a fast lid with a Vs ~ 4.70 km/s in cells I12, I13 and I14. The lithospheric thickness is about 165 km in cells I12, I13 and I14, and it overlies the metasomatic lid, which is about 100 km thick. In cells I15 and I16, under the lid (Vs ~ 4.65 km/s) the bottom of the lithosphere reaches a depth of about 150 km and overlies a relatively fast and thin asthenosphere with Vs ~ 4.50 km/s. To the east, cell I17 (which is not located within the Qinghai–Tibet Plateau) shows a different deep structure, the lid is fast, with Vs ~ 4.70 km/s and a relatively thick lithosphere (~175 km) overlies an approximately 85 km thick asthenosphere with Vs ~ 4.45 km/s.

So far, we have discussed the Vs structure beneath several tectonic areas. In the following section, we briefly discuss the Vs structure across the main tectonic blocks, Himalayan (HB), Lhasa (LB), Qiangtang (QB), Songpan–Ganzi (SB) and Kunlun–Qaidam–Qilian (KB), with reference to some cross-sections in the Tibetan Plateau. Fig. 9a shows the spatial distribution of the seven sections A–A′, B–B′, C–C′, D–D′, E–E′, F–F′ and G–G′, all trending NE–SW. This selection (1) accords with the principle of using sections "orthogonal" to the main characteristics, (2) follows the trend of the tectonic equator (TE) and of the TE-perturbed (Crespi et al., 2007; Doglioni et al., 2007; Panza et al., 2010) and (3) is consistent with the trend of the dominant trends seen in group velocity tomographic maps. All these sections were constructed using Vs cellular models (five for section A–A′, left panel in Fig. 9b), extend from the Indian plain to the northern margin of the Tibetan Plateau, and depict the first-order, large-scale characteristics useful for furthering our general understanding. Regional and local geophysical studies are required to improve the lateral resolution of the deep structure. In all the sections, the uppermost part with Vs < 4.0 km/s is interpreted to be the crust, the portion underlying the crust with Vs values in the range 4.4–4.65 km/s is interpreted to be the mantle lid, and the portion with a Vs of ~4.5 km/s below the mantle lid is interpreted to be the asthenosphere layer. Within the mantle lid, the portion with Vs ~ 4.5 km/s km/s, when present, is interpreted to be the metasomatic lid. With these definitions that, among others, consider the presence of mantle xenoliths in the Mesozoic basalts of the region (Zhang et al., 2002; Y.J. Chen et al., 2004; Fan et al., 2004; Zhang et al., 2004b; Ying et al., 2006), we obtained the conceptual sections shown in the right-hand panels of Fig. 9b–h.

In Section AA′ (left panel, Fig. 9b), the crust gradually thickens from about 40 km south of the MBT to about 80 km beneath the boundary between Tibet and the Tarim Basin (TRM in Fig. 9b). The asthenosphere layer thins from about 80 to 90 km south of the Jinshajiang suture (JS in Fig. 9b); and then to the north the metasomatic lid appears and thickens to ~100 km beneath the north segment of the section.

In Section BB′ (Fig. 9c), the crust and mantle structure is similar to that of section AA′. The major differences are: (1) a step appears in the Moho beneath the JS (Fig. 9c) and (2) the asthenosphere layer is generally 20–30 km thicker and less steep in Section BB′ than in Section AA′.

In Section CC′ (Fig. 9d), the crustal thickening pattern is very different from those along Sections AA′ and BB′. In this section the crustal thickness is relatively constant between the IYS and north to the JS (Fig. 9d), and the asthenosphere layer thins northward at the IYS while keeping a constant thickness to the south; the metasomatic layer begins between the BNS and the JS (the boundary between the south and the north QB).

The structure of the crust along section DD′ is similar to that along section CC′, but the metasomatic lid appears south of the BNS in section DD′ (Fig. 9e). Along section EE′ (Fig. 9f), the step in the Moho is seen to the south of the JS, and the metasomatic lid begins to appear beneath the boundary between the southern and the northern QB Block.

Along Section FF′ (Fig. 9g), the step in the Moho appears beneath the boundary between the southern and the northern QB Block, and the size of the metasomatic lid is rapidly reduced. This situation is similar to that shown in Section GG′ (Fig. 9h), but under Section GG′, the asthenosphere layer thickens from the Indian plain to the central part of the LB block, and then thins northward (Fig. 9h).

5.2. Lithosphere–asthenosphere density structure beneath the Himalaya and Lhasa blocks

We obtained the 3-D ρ structure of the crust and uppermost upper mantle by means of the forward gravity modeling performed with IGMAS and the results can be summarized in four models (S.F. Zhang, 2010). In the following discussion we will consider a typical cross-section, namely section (f) in Fig. 4. The initial 3-D model (Model I) was constructed starting from the available seismic data and the relationship between seismic velocities and density given in Table 3: the resulting gravity anomaly is shown in Fig. 10a. The comparison between the calculated and measured anomalies is clearly not satisfactory. It demands further modeling by adjusting the geometry of the interfaces and inverting densities iteratively. In Model I, the unit QL316 (Qaidam lower crust, for details see the caption of Fig. 10a) is notable for its relatively high ρ value (3.2 g/cm^3). Seismic and seismological investigations indicate a crust thicker than 40 km, thus unit QL316 should be attributed to the lower crust and, consequently, its density should be decreased and a suitable ρ value is estimated to be 3.05 g/cm^3. The geometrical perturbations introduced have a linear dimension of less than about 2 km.

The result obtained so far (Model II) is shown in Fig. 10b and is in better agreement with the observed data than Model I, with the exception of some misfits that are either local or at the border of the model. The main negative anomalies at the contact zone between the Indian and Eurasia plates are properly reproduced.

Eclogitization beneath Tibet is a subject of broad interest in the field. Previous studies have shown that eclogitization of the lower crust is a key process in support of the high elevation of both Himalayas and Tibet (Bousquet et al., 1997; Henry et al., 1997; Cattin et al., 2001; Tiwari et al., 2006; Hetényi et al., 2007). Model III is designed with eclogite in the lower crust, with the same geometry as in Model II (Fig. 10c). The calculated gravity anomaly is remarkably larger than the observed data, when using the model with lower crustal density over 3.3 g/cm^3 beneath the Himalaya and Lhasa blocks. In order to match the calculated gravity anomaly with the observed data, the lower crustal densities are reduced. Finally, Model IV is created and its average lower crustal density is less than 3.2 g/cm^3. Fig. 10d presents the eastern profile with the whole lithosphere structure of Model IV,

which is our preferred model, obtained after performing several tests following a trial-and-error approach. The calculated Bouguer anomaly is in good agreement with the observed data, with the exception of few minor local misfits. Since Model IV is representative of the whole study area, the ρ structural optimization just described can be naturally extended to 3-D and the obtained model can be used as constraint for the subsequent full 3-D inversion to 350 km depth. We consider three initial models. The first model (model A) is derived entirely from the Vs results discussed in detail in Section 5.1, using literature conversion relations between Vs and ρ (see Table 3; Feng et al., 1986; Mueller

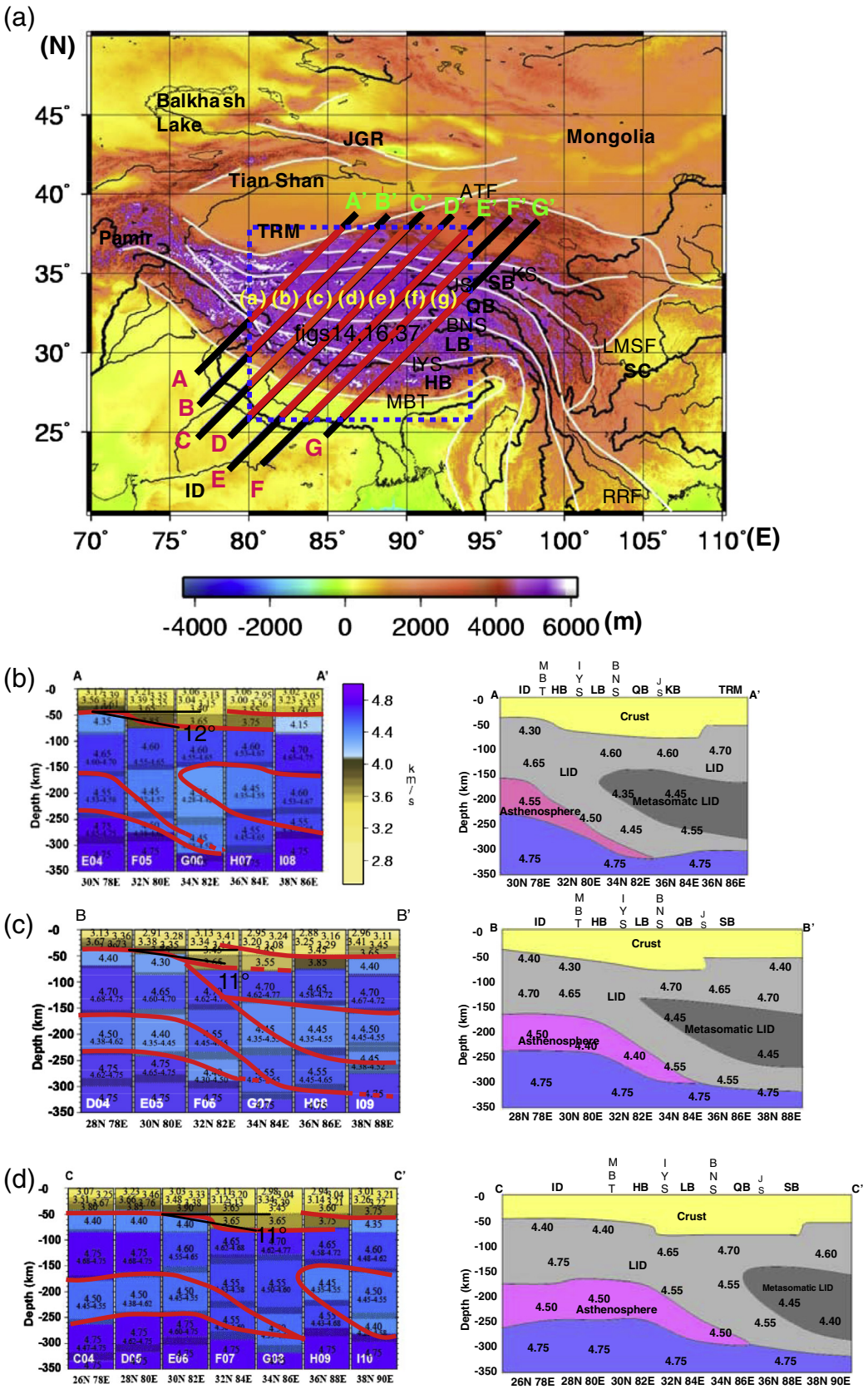

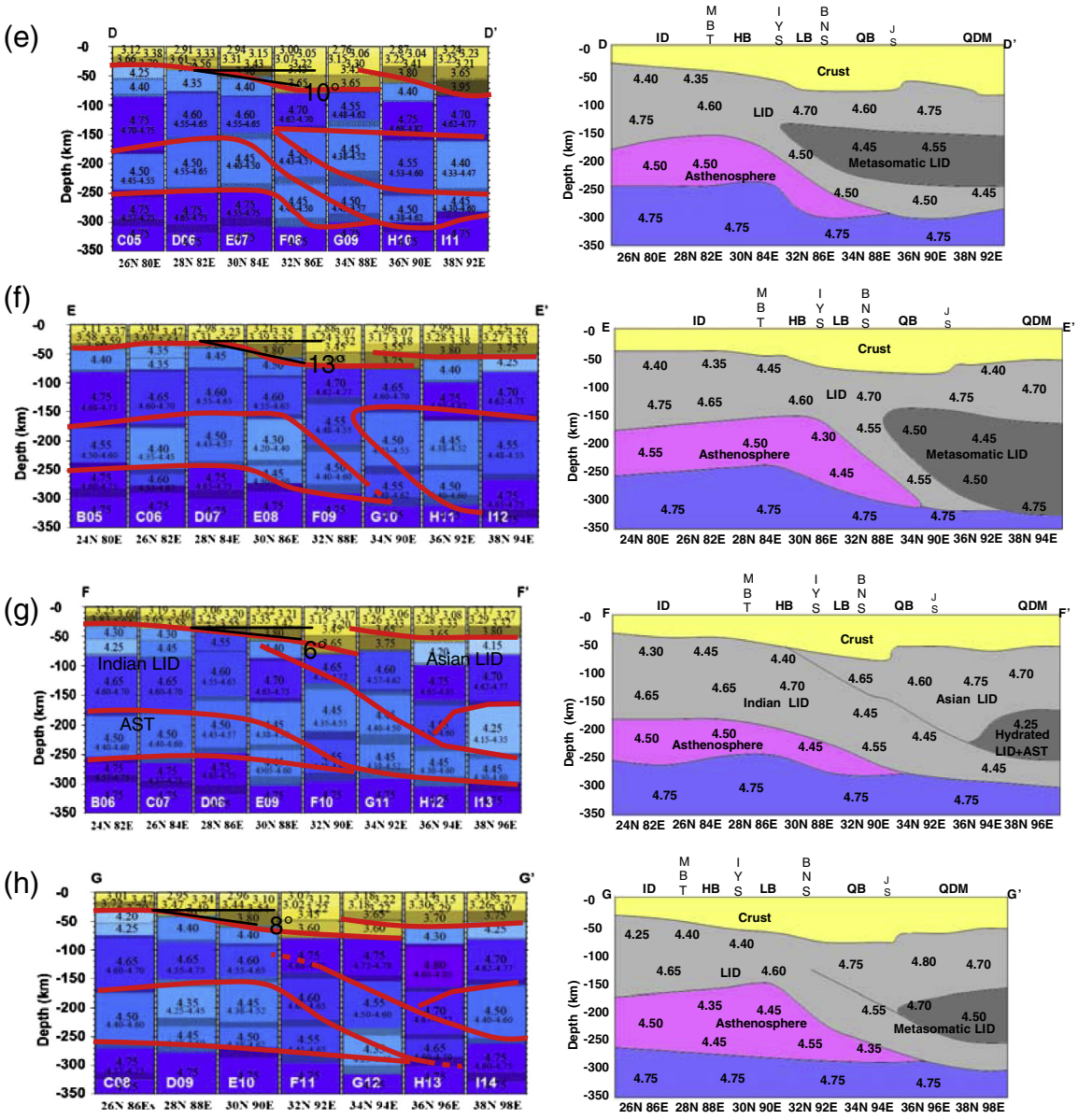

Fig. 9. (a) Spatial distribution of the seven sections A–A′, B–B′, C–C′, D–D′, E–E′, F–F′ and G–G′. All of these sections were constructed from the Vs cellular models. The color scale describes elevation in m. (b) Section A–A′ extends from the Indian plain to the northern margin of the Tibetan Plateau (five cellular models are used). This cross-section, and all the others in this figure, represent a first-order, large-scale feature. The upper part with Vs < 4.0 km/s is interpreted as crust. The portion (underlying the crust) with Vs values of 4.4–4.65 km/s is interpreted as mantle lid while the portion with Vs ~ 4.5 km/s below the mantle lid is interpreted as the asthenosphere layer. Within the asthenosphere, the portion with Vs ~ 4.45 km/s is interpreted as the metasomatic lid. With these definitions, we obtained the conceptual sections shown as right panels of the corresponding figures (left panels in Fig. 12b–h). Considering the uncertainties, the subducted angle of the India plate is about 15° beneath the west of the Tibetan Plateau and about <10° beneath the eastern part. The color scale describes Vs distribution in km/s. IYS: Indus–Yarlung suture; BNS: Bangong–Nujiang suture; JS: Jinshajiang suture; KS: Anyimaqen–Kunlun–Mutztagh suture; QS: South Qilian suture; HB: Himalayan Block; LB: Lhasa Block; QB: Qiangtang Block; SB: Songpan–Ganzi Block; KB: Kunlun–Qaidam Block; ID: Indian Plate; TRM: Tarim Basin; QDM: Qaidam Basin. YB: Yangtze Block; ATF: Altyn Tagh Fault.

and Panza, 1986) and PREM model (Dziewonski and Anderson, 1981) for the crust and upper mantle to a depth of 350 km. As discussed in Section 4.2.3, the ρ distribution in the crust is relatively reliable, and it has been constrained by deep seismic profiles in the IGMAS software. This relatively reliable part of the crustal inversion was therefore introduced as a constraint for the inversion involving the mantle down to 350 km (see e.g., Mueller and Panza, 1986). The constraint has been fixed to the uppermost 40 km (model B) and to the uppermost 80 km (model C) of the structure, whereas the deeper part is common to the three models.

The 3-D ρ inversion code (Li and Oldenburg, 1996, 1998) is used to reconstruct the ρ model of the crust and upper mantle to a depth of 350 km, using the three initial models described above. The performance of the constraints on the reliable ρ distribution in the 3-D density inversion can be measured by the difference between the observed and the computed Bouguer anomalies along the seven profiles shown in Fig. 9a. Fig. 11 shows the misfit between the observed and modeled Bouguer gravity anomalies along the seven transects for the model C. The misfit is within 40 mGal beneath most transects (Fig. 11). In analogy with what done in the Alps by Mueller and Panza (1986), the misfit between the observed and predicted Bouguer anomalies reduces for most transects in a extent, when using model B and model C to constrain their uppermost parts.

The ρ structure beneath the cells in the study area is illustrated in Fig. 12a. Their density values can be seen from the Supplementary material. For the first-order ρ approximation of the crust and upper

Table 3
Physical parameters of the different bodies used in the initial modeling.

Description	ρ	V
	(g/cm^3)	(km/s)
Tertiary Indian foreland basin	2.45	Vs = 2–2.75 (Mitra et al., 2005)
India UC—lesser Himalayan	2.7–2.89	Vs = 3.5–3.8 (Mitra et al., 2005)
Greater Himalayan belt	2.75–2.91	Vs = 3.4–3.8 (Mitra et al., 2005) Vp > 5.7 (Hauck et al., 1998)
Tethyan Himalayan sequences	2.65–2.7	Vs = 2.5–3.2 (Mitra et al., 2005) Vp = 5.2 (Hauck et al., 1998)
Gangdese Batholith	2.75	Vp = 6–6.5 (Meissner et al., 2004)
Lhasa terrane UC	2.7–2.93	Vp = 6.1–6.5 (Zhao et al., 2001c)
Qiangtang Basin, sediments	2.5–2.6	Density (Haines et al., 2003a,b) Vp ~ 5.7 (Meissner et al., 2004)
Qiangtang terrane UC	2.64–3.01	Density (Haines et al., 2003a,b) Vp ~ 5.8–7 (Meissner et al., 2004) Vp ~ 5.6–6.5 (Zhao et al., 2001c)
Songpan–Ganzi terran, Kunlun	2.6–2.85	Vp = 5.4–6.2 (Jiang et al., 2006a)
Qaidam Basin	2.4	Vp = 5–5.5 (J.M. Zhao et al., 2006)
Qaidam–Qilian Shan UC	2.53–2.92	Vp = 6–6.3 (Jiang et al., 2006a) Vp = 5.5–6.5 (J.M. Zhao et al., 2006) Vp = 5.5–6.3 (Gao et al., 1999)
India LC	2.98	Vs = 3.9 (Mitra et al., 2005)
Greater Himalayan LC	3.05	Vs = 4–4.2 (Mitra et al., 2005)
Lhasa–Qiantang LC	3.05	density (Haines et al., 2003a,b) Vp = 6.6–7.1 (Meissner et al., 2004) Vp = 7–7.3 (Zhang and Klemperer, 2005) Vp = 6.5–7.3 (Zhao et al., 2001c)
Qaidam–Qilian–Beishan LC	3.0	Vp = 6.5–6.8 (Jiang et al., 2006a)
Lithospheric mantle	3.2	

mantle to a depth of 350 km, eleven cells (the cells labeled A01–A08 and B01–B03) are used to describe the density structure beneath the northern Indian Plate (Fig. 12a). Eight cells (B04–B08 and C01–C03) are used to characterize the density structure beneath the Himalaya Block. Thirteen cells, C04–C08 and D01–08, are used to characterize the density structure beneath the LB. Similarly, the sixteen cells, labeled E01–E08 and F01–F08, are used to describe the density distribution of the QB and SB blocks, respectively. Five cells (G04–G08) are used to describe the density structure for the Qaidam–Kunlun Block, and three cells (G01–G03) for the southern Tarim Basin (Fig. 12a).

Fig. 12b displays the final cellular ρ models for the study area of the Tibetan Plateau and neighboring regions. The main features of the density distribution in the crust and upper mantle can be summarized as follows. Beneath the northern Indian Plate, in cells A01–A08 the crust is as thick as about 40 km, and then thickens to about 50 km under cells B01 and B02. The lateral heterogeneity in the Indian plate can be exemplified by the fact that the crust is relatively denser to the west (A01–A04) than the east (A05–A08), and this fact may be related to along-strike variation in the Himalaya and even in the whole Tibetan Plateau. Beneath the Himalaya Block, the west–east variation of crustal ρ can also be observed: ρ beneath the western part (cells B03–B06) is obviously higher than under the eastern part (cells B07 and B08). The lateral variation of ρ is more pronounced below 50 km depth, which may indicate the superposition of the subducted Indian crust and its extrusion. Beneath the LB, the crustal thickening is obvious as is its lateral variation: in cells C03–C08, the crustal thickness is >70 km, while in cells C01 and C02 it is about 80 km, with relatively denser lower crust and lighter upper crust, compared to what is seen towards the east. Beneath the QB, the crustal thickness is about 60–65 km in cells E03–E06, reaching 80 km in the three cells C01–C03, and decreasing to 70 km in the eastern cells E07 and E08. The ρ distribution beneath the SB (cells F01–F08) is somewhat similar to that under the QB Block, but strikingly different from that under the Qaidam–Kunlun Block and the Tarim Basin (Fig. 12b).

In the following, we discuss the ρ structure beneath several areas with reference to the Vs structure, and we briefly discuss the seismic ρ–Vs structure along sections in the Tibetan Plateau, across the main tectonic blocks (HB, LB, QB, SB and KB). The ρ-depth distribution along profiles (positions as shown in Fig. 9a (a), (b), (c), (d), (e), (f) and (g) is shown in the different panels of Fig. 13. In all these cross-sections, the upper part with ρ < 2.90 g/cm^3 (Vs < 4.0 km/s) is interpreted to be the crust, and the portion (underlying the crust) with ρ increasing from 3.2 g/cm^3 to 3.4 g/cm^3 (Vs 4.4–4.65 km/s) is interpreted to be the mantle lid. The part with ρ ~ 3.3 g/cm^3 (Vs ~ 4.5 km/s) below the mantle lid is interpreted to be the asthenosphere layer. Within the asthenosphere, the portion with ρ ~ 3.3 g/cm^3 (Vs ~ 4.45 km/s) is interpreted to be the metasomatic lid. Lateral variations in ρ extend to a depth of 350 km, and therefore earlier crust and uppermost mantle ρ models along the INDEPTH profiles or other north–south trending profiles, all limited to the crust and uppermost upper mantle (to a depth around 70 km), cannot be generalized to the whole of the Tibetan Plateau. Along profiles (a) (Fig. 13a) and (b) (Fig. 13b) ρ ranges from 2.4 g/cm^3 to 2.9 g/cm^3 in the crust, and the layer with ρ in the range 2.8–2.9 g/cm^3 thickens to about 70 km to the north (to about 30° N). These results may be consistent with the speculation that the crust of the Indian Plate penetrated through the whole of the Tibetan Plateau (Zhou and Murphy, 2005; Li et al., 2008; Zhang et al., 2011e). Along transects (c) (Fig. 13c), (d) (Fig. 13d) and (e) (Fig. 13e), we clearly observe that the convergence between the Indian and Eurasian plates thickens the crust between these two transects. These results may suggest that the leading edge of the injected Indian crust may be located at the Bangong–Nujiang suture (Zhang et al., 2011c). In Fig. 13f the mantle lid thickens remarkably north of the Yarlung–Zangbo suture, where the crust is also thickened. Compared with the other transects (Fig. 13a–g), the area of the metasomatic lid is reduced northward (Fig. 13f).

5.3. Crustal structure in the North China Craton

5.3.1. Group velocity distribution

Using the tomographic method, as described in Section 4.2.1, Rayleigh wave group velocity maps at 4.5 s, 12 s, 20 s and 28 s were produced (Fig. 14) from ambient noise records. At 4.5 s (Fig. 14a), the shortest period of our tomography, the partial derivative of the group velocity with respect to Vs shows a peak at a depth of about 7 km. The group velocity map at 4.5 s is therefore sensitive to variations in Vs at depths around 7 km and mainly reveals the characteristics of the uppermost crust, and can be correlated with the thickness and mechanical properties of the sedimentary cover. The boundary between the North China Plain (NCP) and the surrounding mountain ranges is clearly outlined. A broad low-velocity zone is observed in the NCP, which is due to the large thickness of sediment. Zheng et al. (2005) derived the shear wave velocity model in the NCP by inverting the receiver functions obtained at 44 temporary seismic stations. Their results indicate that the sedimentary cover of the NCP is about 2–12 km thick. The Taihangshan and Yanshan uplifts are imaged as high velocity zones. The Quaternary intermountain basins, such as Yanqing–Huailai, Yangyuan–Yuxian, Datong and Zhangjiakou, show up as low-velocity anomalies. A small low-velocity anomaly is observed between Fuping and Yuxian, which is consistent with the location of the Lingqiu Basin. In general, the group velocity map correlates very well with known geological structures. The resolution in the southeastern part (NCP) is relatively low because the local noise in this part is very strong and at the same time wave attenuation in the sediment basin is very strong, so it is very difficult to obtain cross correlations with high SNR. At a period of 12 s (Fig. 14b), the lateral resolution is improved by the increase in ray-path density and the group velocity map shows lateral variations as large as 1.2 km/s. Geological units with small areas can be identified clearly and the Jizhong Depression, Cangxian Uplift and Huanghua Depression are also mapped. Filled in by thick sedimentary deposits, the Jizhong and Huanghua depressions are mapped by relatively low velocities, while the Cangxian, Taihangshan and Yanshan horsts are

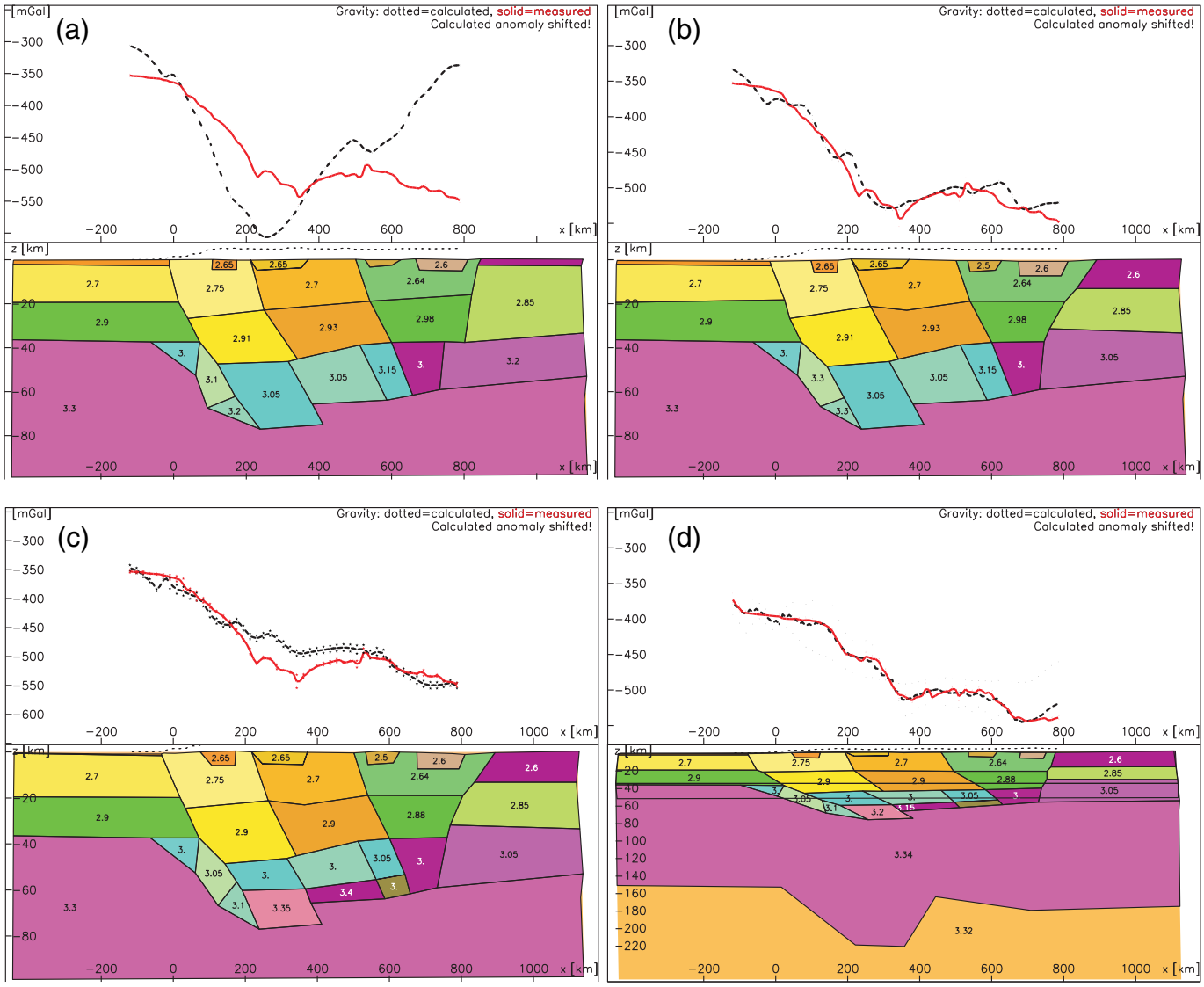

Fig. 10. Typical cross-section across the study area, namely section (f) in Fig. 4. (a) The initial density crustal model (Model I) is defined from seismic velocity models according to the relationship between velocity and ρ given in Table 3 (S.F. Zhang, 2010). The misfit is quite evident. (b) Density of some units and the geometry of interfaces have been changed with respect to Model I. (c) If we impose eclogitization beneath Tibet, we can get Model III (the geometry is the same as Model II), the calculated gravity anomaly is larger than the observed data. (d) The final model (Model IV) with its average lower crustal density is less than 3.2 g/cm^3. It is in good agreement with the observed data, with the exception of some misfits that are either local or at the border of the model. The main negative anomalies of the contact zone between the Indian and Eurasian plates are properly reproduced.

mapped by high velocities. The Yanqing–Huailai, Yangyuan–Yuxian and Datong basins still show up as low velocities.

Using 30 DSS profiles, Jia and Zhang (2005) studied the velocity structure of the crust beneath the eastern and the central NCC. Their results reveal that the thicknesses of the sediment deposits in the Huanghua and Jizhong depressions are about 7–9 and 6–10 km, respectively. Therefore the low velocities in the tomographic maps at short periods are an excellent indicator of the location and nature of the sedimentary basins in North China, i.e. the extremely thick sedimentary deposits are the direct cause of the low-velocity anomalies of Rayleigh waves in the Jizhong and Huanghua depressions.

For periods shorter than 20 s, the tomographic maps predominantly reflect the low velocities caused by sedimentary basins. Almost all the basins are mapped as low velocity areas. However, with respect to shorter periods, at 20 s the area of low velocity in the Jizhong Depression is smaller, while a large high velocity is seen in the Cangxian Horst; the velocity differences between the sediment basins, such as Yangyuan–Yuxian and Yanqing–Huailai, and their surrounding areas decrease (Fig. 14c).

At the 28 s period (Fig. 14d), waves are primarily sensitive to depths between 30 km and 50 km, namely, to the lower crustal velocity, the crustal thickness and the uppermost upper mantle velocity. As expected, in this map the influence of the sedimentary basins decreases and the group velocity map differs greatly from those obtained at 4.5 s, 12 s and 20 s. High velocities are observed in the eastern part of the study region, while low velocities are observed in the northwestern part. Thick crust is mapped by low velocities; thin crust by high velocities. Reflection and refraction profiles in North China (Jia and Zhang, 2005; Jia et al., 2005) show that the crust is relatively thin in the NCP, and thick in the northwest of our study region: the crustal thickness is about 28–29 km in Bohai Bay, about 35–36 km in Beijing and more than 40 km to the west of the Taihangshan Fault. Group velocities at the 28 s period show a well-defined low-velocity zone in the Beijing–Tianjin–Tangshan region (Fig. 14d). In our tomographic results, the low velocity zone in the Beijing–Tianjin–Tangshan region can be seen between 23 and 30 s. Tomographic maps at these periods mainly reveal the velocity structures in the lower crust and uppermost upper mantle. In the tomographic maps two further important characteristics can be

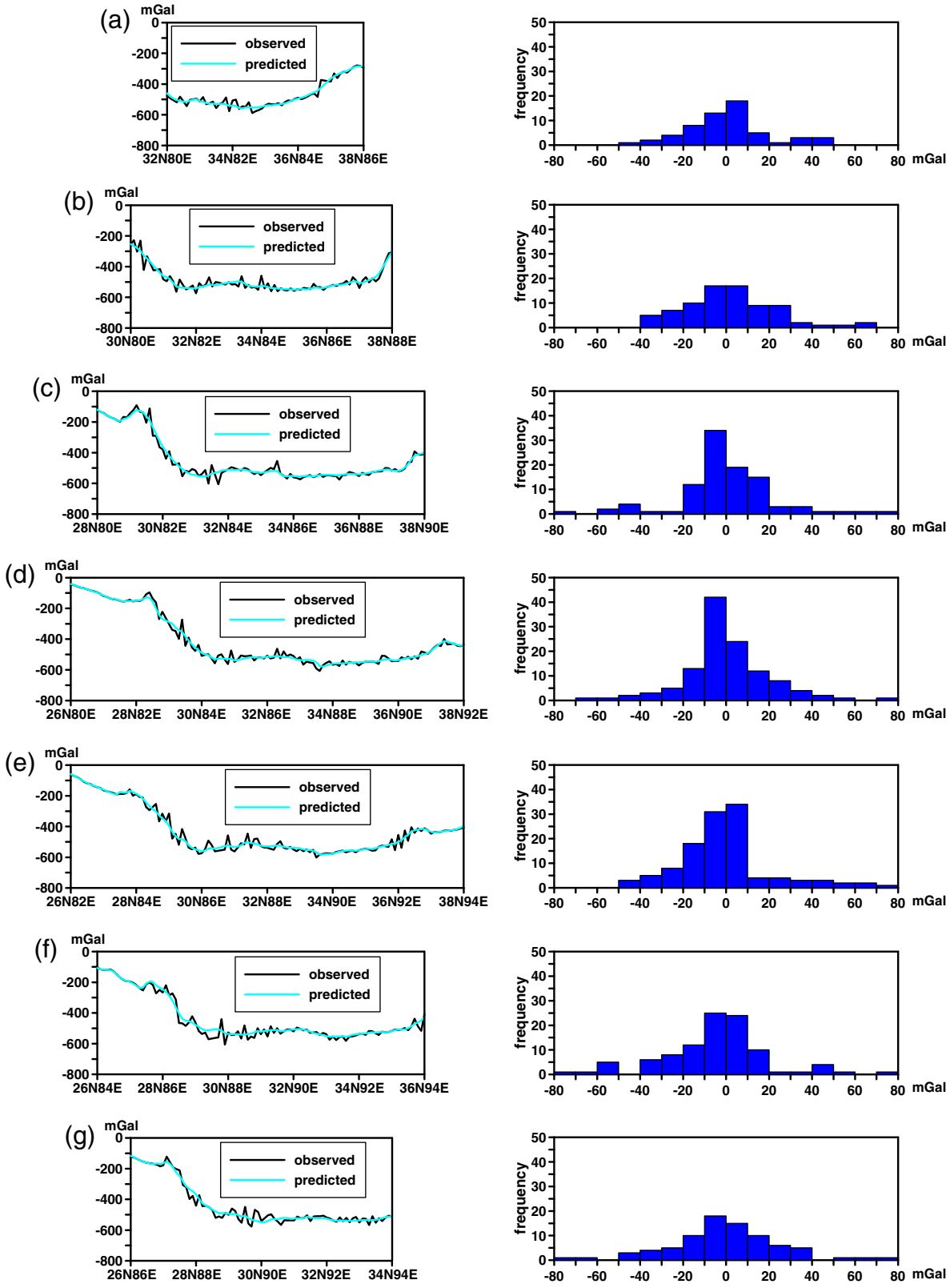

Fig. 11. The misfit between the observed and the expected Bouguer anomaly along the profiles (a), (b), (c), (d), (e), (f) and (g). The location of the profiles are shown in Fig. 9a.

seen: (1) a high velocity zone near Datong, Shouzhou and Qingshuihe and (2) a strong velocity gradient near the boundary between the North China Basin and the Yanshan–Taihangshan uplift. The zone with high-velocity Rayleigh waves near Datong, Shouzhou and Qingshuihe is located at the northeastern margin of the Ordos Block, which shares the typical features of cratonic lithosphere and has not been affected by the reactivation of the NCC. The trend of the strong group velocity gradients seen near the boundary of the NCP and the Yanshan–Taihangshan

Uplift resembles that visible in the Bouguer gravity anomaly map (Yin et al., 1989), where along the NE–SW-trending Taihangshan Uplift, a continuous gradient zone is obvious.

The Taihangshan Fault is within this gradient belt and P-wave tomography has shown that the fault cuts through the Moho interface and penetrates into the upper mantle (Huang and Zhao, 2004; J. Zhang et al., 2007). The belt therefore represents a major lithospheric boundary and separates the NCC into western and eastern sectors, which can be shown to have fundamentally different architectures. Gravity anomaly values decrease from east to west, indicating that the main ρ interface (Moho discontinuity) is deeper in the west than in the east. Both densities and velocity structures thus differ considerably between the two sides of the Taihangshan Fault.

5.3.2. Crustal structure

We constructed a 'favored preliminary model' using Genetic Algorithm (GA) inversion of the dispersion relations at each grid point. Juxtaposing these 1-D isotropic models, we obtained a 3-D Vs velocity model for about the uppermost 50 km of the North China Craton. The fully non-linear inversion will be the subject of a forthcoming paper. Horizontal slices of Vs at selected depths (1, 8, 10, 12, 27 and 36 km) are shown in Fig. 15a–f. The most striking features at 1 km depth (Fig. 15a) are several large sedimentary basins. The NCP, Yanqing–Huailai Basin and Datong Basin clearly appear as low Vs regions. Due to the large sediment thickness, a broad zone with low Vs is observed in the NCP. Zheng et al. (2005) derived the Vs model in the NCP by inverting the receiver functions obtained at 44 temporary seismic stations. Their results indicate that the thickness of the sedimentary cover in the NCP varies between 2 km and 12 km. Taihangshan and Yanshan horsts are imaged as high-velocity zones. In general, the Vs structure at 1 km correlates very well with known surface geological structures. At 10 km and 12 km depths, the Jizhong Depression, Cangxian Uplift and Huanghua Depression are mapped very well. Finally, at 36 km depth, high velocities (Vs about 4.2–4.4 km/s) are observed in the eastern part of the study region, while low velocities (Vs about 3.4–3.6 km/s) are observed in its northwestern part.

A high velocity zone (Vs about 3.6–3.8 km/s) near Datong, Shouzhou and Qingshuihe is observed in the depth range from 1 to 23 km, at the northeastern margin of the Ordos Block. The block is characterized by low seismicity, low heat flow, a positive vertical velocity gradient and a lack of active fault and magmatic activity (Qiu et al., 2005). The inversion results agree with the stable characteristics of this region. A strong velocity gradient near the boundary between the NCP and the Yanshan–Taihangshan Uplift can be seen in the 1–12 km depth range. Below 13 km, the high to low velocity contrast near the Taihangshan front fault fades away and remains visible only sporadically. Thus the Taihangshan front fault does not penetrate through the Moho discontinuity along the whole fault, but probably only in some part. P-wave tomography, on the other hand, has shown that the fault cuts through the Moho interface and penetrates into the upper mantle (Huang and Zhao, 2004; J. Zhang et al., 2007). The discrepancy may be caused by a key difference in the tomographic methods used. P-wave tomography is a relative method, and as such is very sensitive to the reference velocity model used. Surface wave tomography supplies absolute models that, when obtained by direct non-linear inversion of a dispersion relation, do not depend on any a priori assumptions of an initial reference model, and permit an estimation of the uncertainties in the results (e.g. Panza et al., 2007a,b). Zhu and Zeng (1990) found a low velocity section in the Beijing–Tianjin–Tangshan region at 50 km depth, which extends to 100 km beneath Tangshan and Tianjin. Using regional seismic arrival data and the Simultaneous Iterative Reconstruction Technique, Ding and Zeng (1994) showed that a clear low velocity zone lies between Beijing and Tangshan in the 20–35 km depth range. Recent body wave tomography shows a low velocity zone in the lower crust beneath the Beijing–Tianjin–Tangshan region (Huang and Zhao, 2004) as well. In our tomographic results, the low velocity zone in the Beijing–Tianjin–Tangshan region can be seen between 22 and 30 km. We infer that the low velocity zone is related to the upwelling of hot mantle material or to fluids and partially molten material as suggested by Huang and Zhao (2004). Seismic refraction and reflection profiles across Tangshan indicate that there is a 3–5 km offset of the Moho discontinuity beneath Tangshan (Zeng et al., 1988). The hot

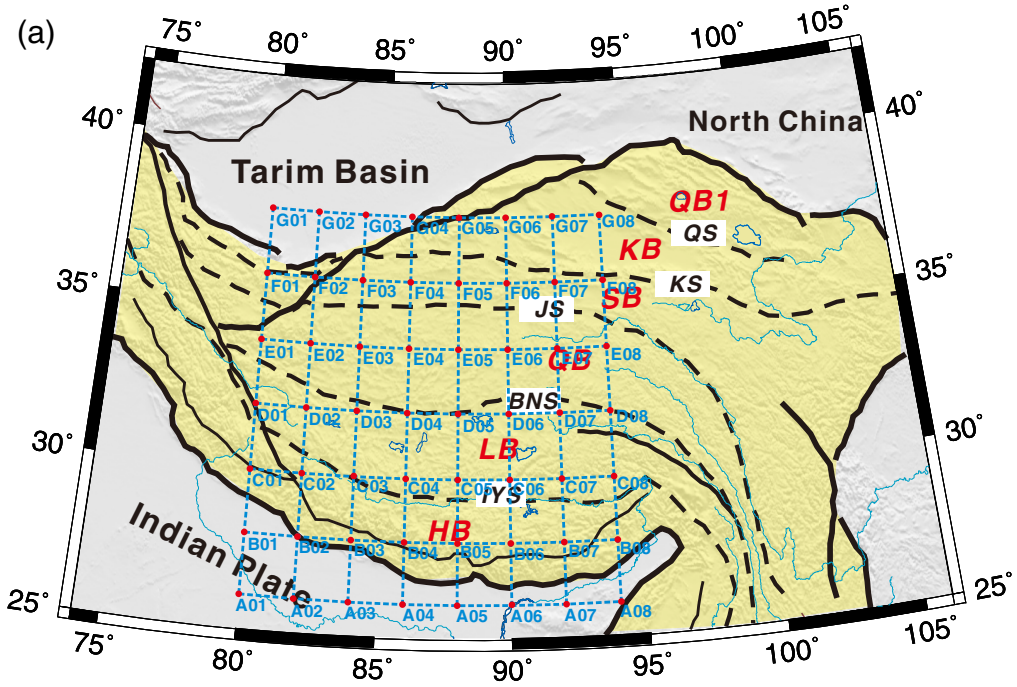

Fig. 12. (a) The spatial distribution of the cells covering the area where Bouguer gravity anomaly inversion was performed to define the ρ versus depth distribution in the uppermost 350 km. IYS: Indus–Yarlung suture; BNS: Bangong–Nujiang suture; JS: Jinshajiang suture; KS: Anyimaqen–Kunlun–Mutztagh suture; QS: South Qilian suture; HB: Himalayan Block; LB: Lhasa Block; QB: Qiangtang Block; SB: Songpan–Ganzi Block; KB: Kunlun–Qaidam Block. (b) the final ρ cellular models in the study area of the Tibetan Plateau and its neighboring regions. The color scale gives density in g/cm^3.

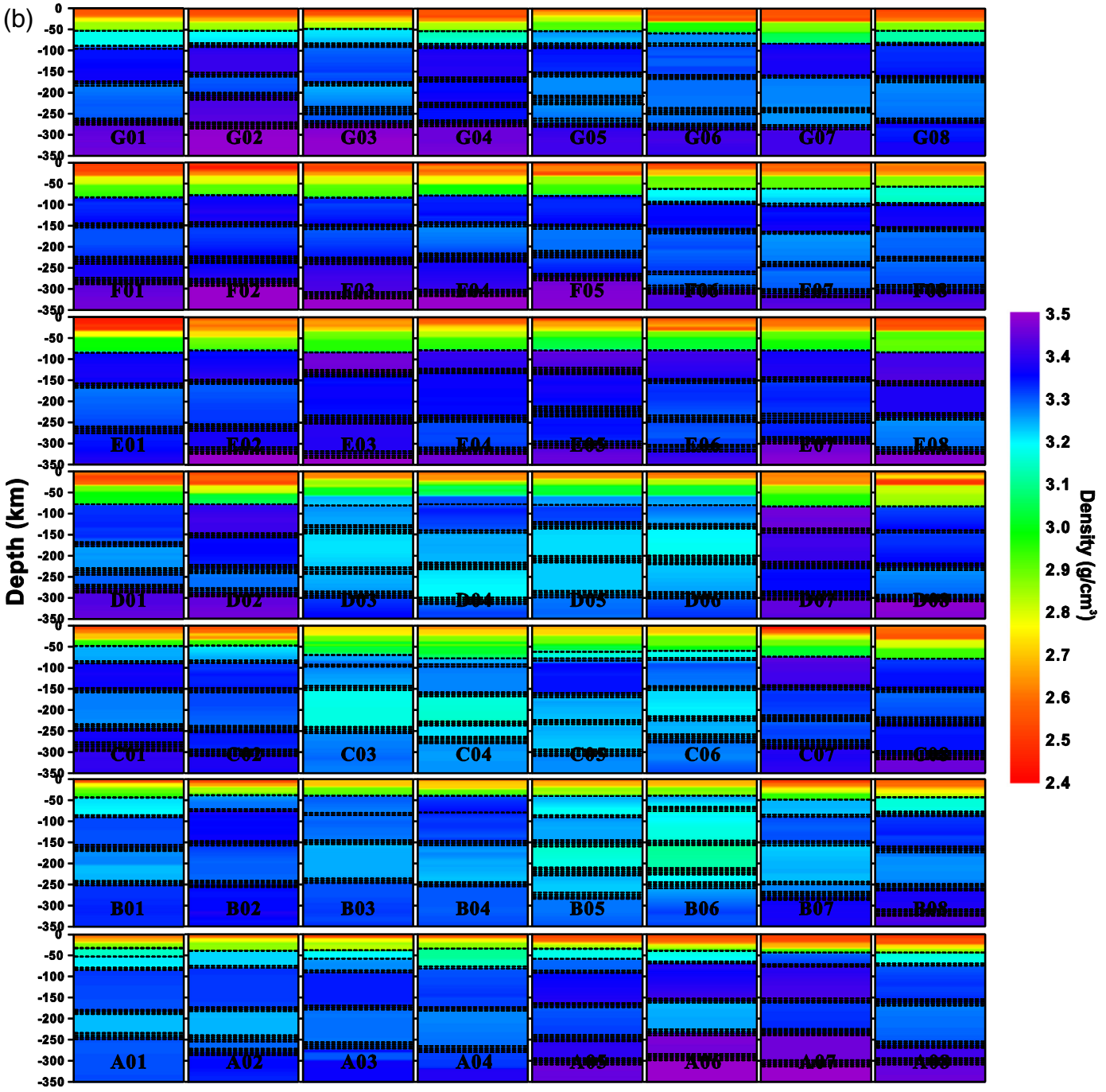

Fig. 12 (*continued*).

material of the uppermost upper mantle may migrate to the crust along the offset of the Moho discontinuity. The intrusion of mantle material heats up the lower crust and can cause the reduction of seismic velocity. A high conductivity layer has been found between 20 and 30 km depth under this region using magnetotelluric soundings (Liu et al., 1989).

6. Discussion

6.1. Lateral variation of the metasomatic lid and partial melting anomaly beneath the Tibetan Plateau

Averaged models of the lithosphere–asthenosphere system in the Qinghai–Tibet Plateau and its vicinity have been obtained using hedgehog non-linear inversion (Valyus et al., 1969; Knopoff, 1972; Valyus, 1972; Panza, 1980, 1981). The depth of the Mohorovicic discontinuity is identified, as a rule, as the depth of the strong Vs gradient from ~3.7 km/s to ~4.3 km/s. The depth where the Vs value begins to decrease is considered to be the bottom of the lithosphere. The asthenosphere is a relatively low velocity zone that extends from the bottom of the lithosphere to a greater depth, where Vs is again as much as or larger than that at the bottom of the lithosphere. In several cellular models the situation is not so straightforward and an approximately 100 km thick metasomatic lid is detected as the main consequence of the subduction of the Indian Plate.

Referring to the division of the tectonic setting in the Tibetan Plateau (Fig. 1b) and to the differences in the upper-crust, lower-crust, mantle

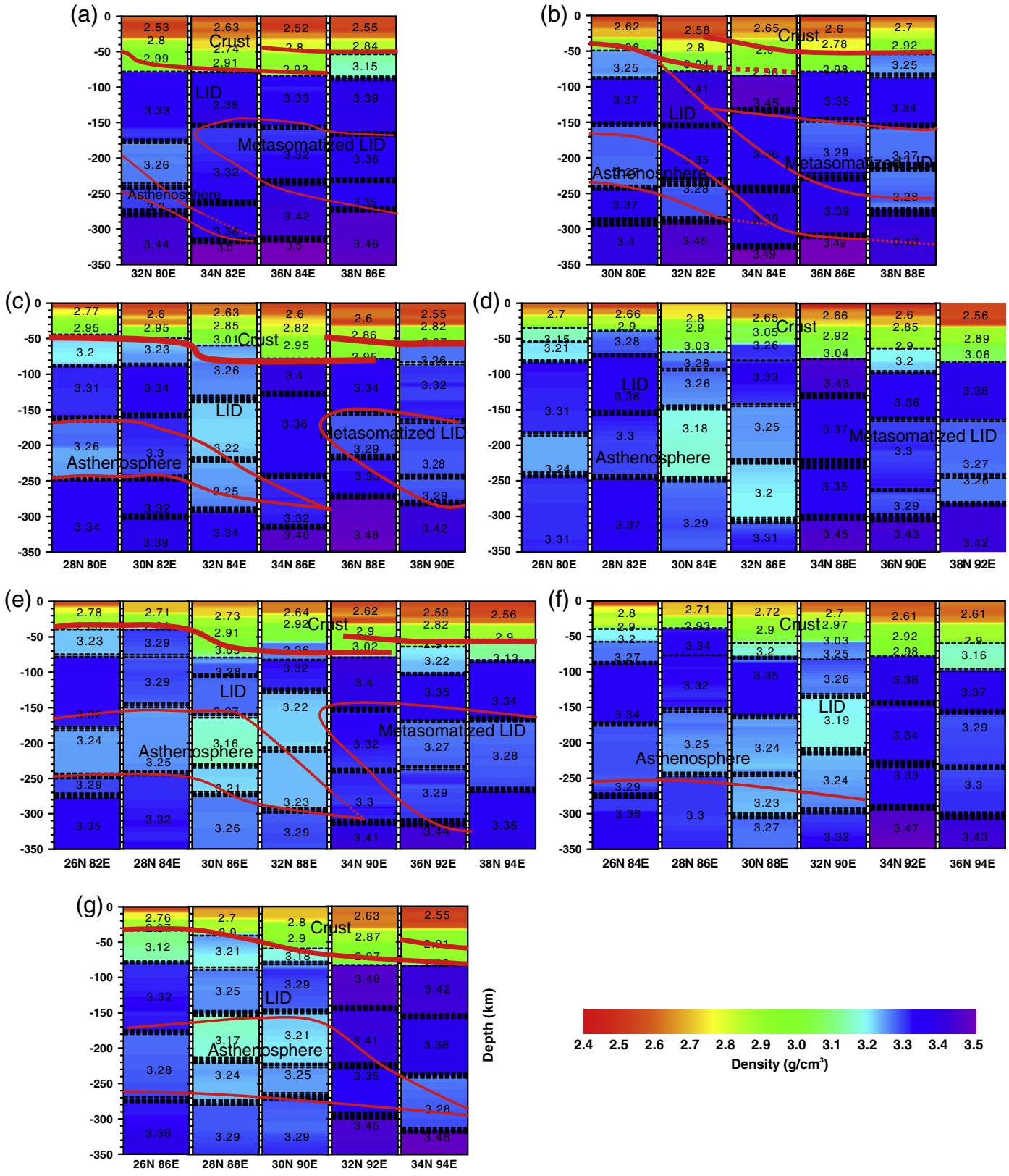

Fig. 13. Distribution of ρ reaching the depth of 350 km along the seven sections (a), (b), (c), (d), (e), (f) and (g). The location of the profiles is the same as in Fig. 9a. The color scale gives density in g/cm^3.

lid, metasomatic lid and asthenosphere (Figs. 9 and 13), we compiled the Vs–ρ values for different tectonic units and different portions in the upper mantle and constructed the Vs–ρ diagram shown in Fig. 16. The Vs and ρ structure of the crust and upper mantle show two remarkable characteristics: (1) the mantle lid and crust naturally define two distinct Vs–ρ domains: the mantle lid occupies the upper right

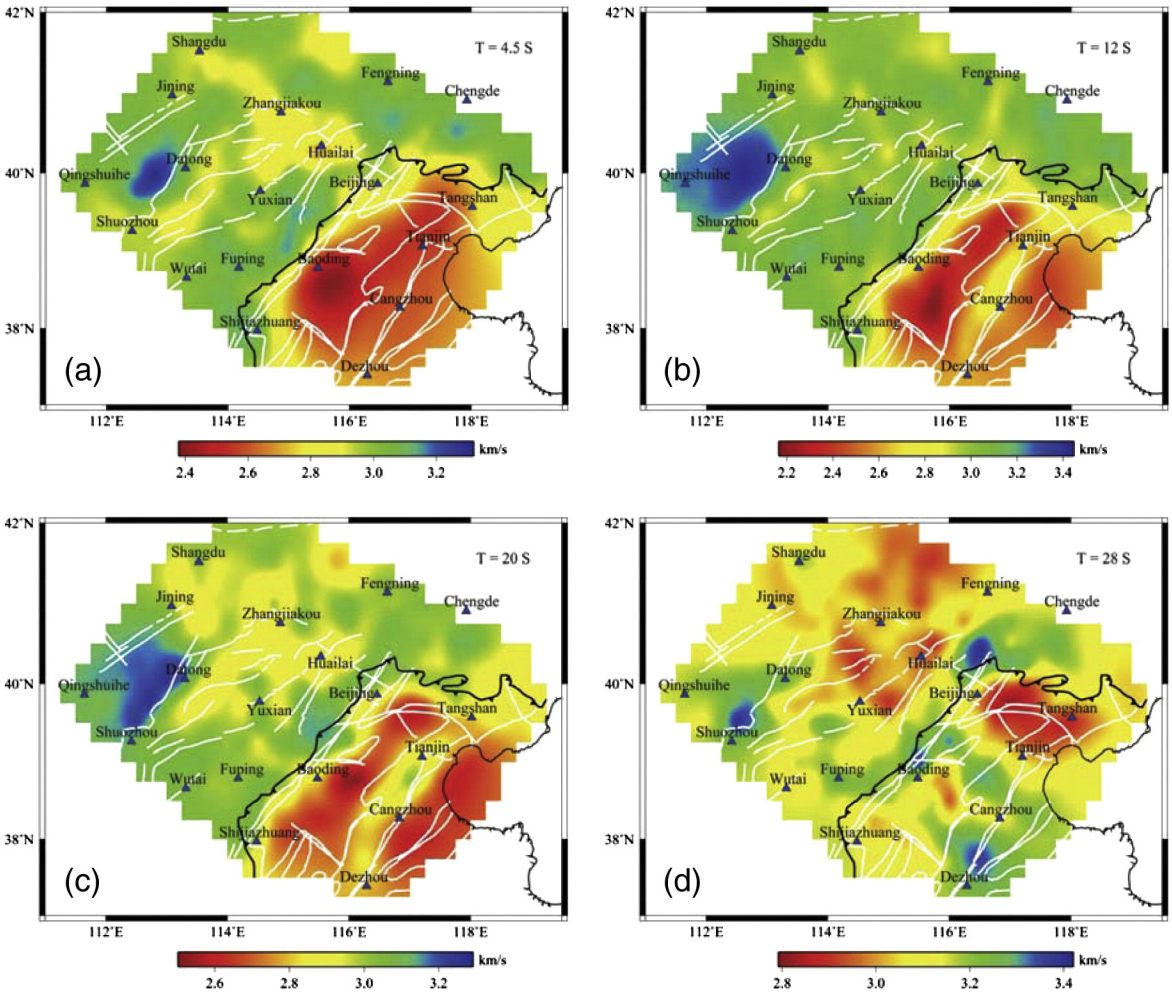

Fig. 14. Ambient noise tomography: Rayleigh wave group velocity maps at 4.5 s, 12 s, 20 s and 28 s obtained using the tomographic method.

corner of the domain while the crust occupies its lower left corner and (2) beneath different tectonic blocks of Tibet, there are obvious variations in the metasomatic lid (Vs and ρ). In addition, the Vs–ρ distribution in the crust can be grouped for different tectonic blocks. Usually we observe that the range of crustal ρ values is slightly greater for the Himalaya Block (HB) and the Lhasa Block (LB), whereas the Vs range is relatively narrower for the Qiangtang (QB) and Songpan–Ganzi blocks (SB). This difference may reflect the difference in composition of the crust of tectonic blocks to the north and south of the Bangong–Nujiang suture. For the mantle, we observe that the range of ρ values is usually 3.0–3.4 g/cm^3, and Vs range is 3.5–4.75 km/s for HB and LB. For the mantle in the QB and SB, the ρ range is 3.1–3.3 g/cm^3, while the Vs range is 4.0–4.6 km/s. The differences in Vs–ρ distribution may correspond to two different mantle and crust typologies belonging to the Indian and Eurasian plates, respectively.

The Tibetan Plateau is the product of the continuing collision of India with the southern margin of Eurasia over the past 65 Ma. The Cenozoic magmatism is extensive, and granitic intrusions and potassic volcanic rocks are widely distributed in the Tibetan Plateau (Yin and Harrison, 2000; Mo et al., 2008; Fu et al., 2010). At least 3 petrogenetic mechanisms for the origin of granite in the Tibetan Plateau have been proposed: (1) crustal anatexis during continental collision; (2) high-temperature crustal anatexis related to asthenospheric upwelling and mantle attenuation; and (3) partial melting of thickened lower crustal rocks, triggered by underplating of ultra-potassic magma during slab breakoff.

The observed lateral variation of the metasomatic lid is in agreement with the discoveries of Miocene potassic granite–syenite associations in both the western and the eastern Tibetan Plateau (Jiang et al., 2006b, 2010, 2012).

In the western Tibetan Plateau, the Miocene (12–10 Ma) Karibasheng and Kuzigna plutons are composed of monzogranite, syenogranite, diopside-bearing syenite and diopside syenite. These rocks are shoshonitic and have very high Ba and Sr concentrations. The granites and syenites in the western Tibet Plateau have higher Ba/Rb (10–34) and lower Rb/Sr (0.08–0.26) ratios than the Yulong monzogranite-porphyry in the eastern Tibetan Plateau, suggesting the presence of both phlogopite and amphibole in their source regions. Detailed elemental and isotopic data suggest that the granites and syenites were derived directly from the veined lithospheric mantle that had been hybridized by continental slab-derived melts. The continental slab break-off was most likely to be the mechanism associated with the generation of granites and syenites (Jiang et al., 2012).

In the eastern Tibetan Plateau, the Yulong monzogranite-porphyry shows clearly high Rb/Sr (>0.17) and low Ba/Rb (<7) signatures, and has been inferred to have been derived from a phlogopite-bearing (amphibole-free) source (Jiang et al., 2006b). Low-degree melting of a metasomatic lithospheric mantle has been proposed as the origin of the Cenozoic Yulong monzogranite-porphry (Jiang et al., 2006b).

6.2. Transition from W- to E- and NE-directed subduction: a mechanism to explain the lateral variation of the mantle lid?

GPS measurements suggest an along-strike variation of the rate of motion between the west and east of the Himalaya and even the whole Tibetan Plateau. The seismic activity pattern, the high or ultra

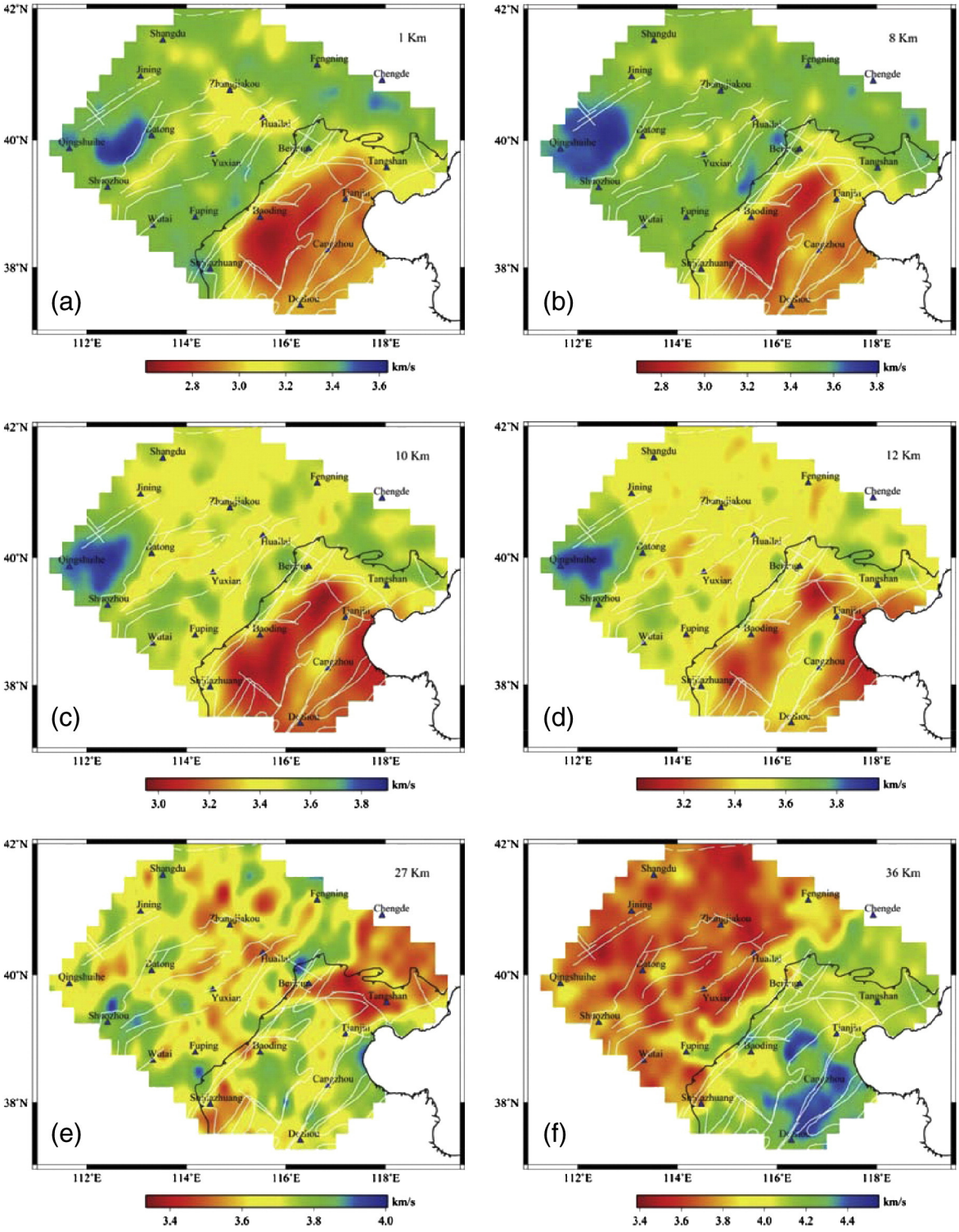

Fig. 15. Horizontal slices of Vs at selected depths (1, 8, 10, 12, 27 and 36 km) as determined using a 'favored preliminary model' defined through Genetic Algorithm (GA) inversion of the dispersion relations at each grid point. Juxtaposing these 1-D isotropic models, we obtained a 3-D Vs velocity model for the uppermost 50 km of North China.

high-pressure metamorphic rock distribution and the westward flow of the Indus River, opposite to the eastward flow of the Yarlung River, represent remarkable phenomena associated with the along-strike variation of motion in the Himalaya. The lateral variation in metasomatic lid thickness, the spatial distribution and thickness of the partial melting layer and the geochemical features of granitoids may represent important responses to the transition of the subduction polarity from W- to E- and NE-directed. By polarity we mean the direction of subduction with respect to the tectonic mainstream, which is not E–W, but can be identified with a great circle, the tectonic equator (TE), that forms an angle relative to the geographic equator close to that of the revolution plane of the Moon (Doglioni, 1990, 1991; Riguzzi et al., 2006; Crespi et al., 2007; Doglioni et al., 2007). In the hotspot reference framework a "westward" rotation of the lithosphere can be observed (Gripp and Gordon, 2002; Cuffaro and Jurdy, 2006). The origin of this net rotation of the lithosphere

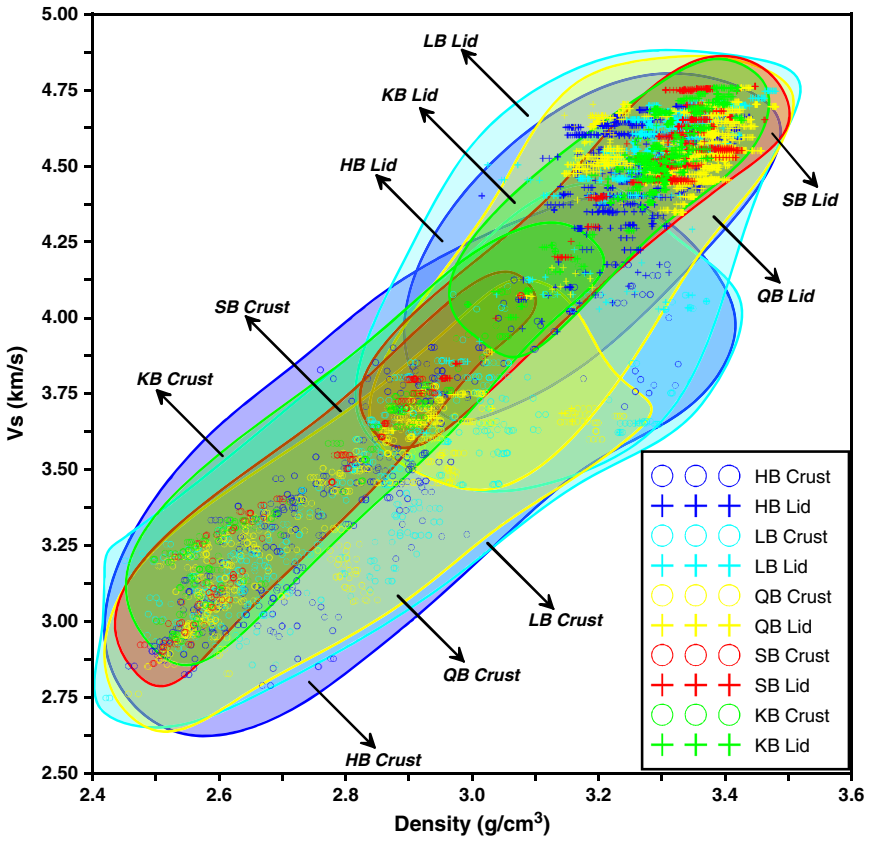

Fig. 16. Vs–ρ diagram from Vs (Fig. 9) and ρ (Fig. 12) structural models of the crust and upper mantle. The Vs–ρ distribution in the crust can be grouped for different tectonic blocks; beneath different tectonic blocks of Tibet, there are obvious variations in the metasomatic lid HB: Himalayan Block; LB: Lhasa Block; QB: Qiangtang Block; SB: Songpan–Ganzi Block; KB: Kunlun–Qaidam Block.

(Bostrom, 1971) is still under debate (Scoppola et al., 2006), but it should range between 4.9 (Gripp and Gordon, 2002) and 13.4 cm/yr (Crespi et al., 2007) at the tectonic equator. This implies that the plate motion flow is significantly polarized toward the "west" (Doglioni et al., 1999a,b), and subduction zones follow or oppose the relative "eastward" mantle flow. Subduction zones following the flow are the North and South American cordilleras, the Dinarides, the Hellenides, the Caucasus, Zagros, Makran, the Himalayas, the Indonesia–Sunda arc, Taiwan, New Guinea, New Hebrides and southern New Zealand. Subduction zones opposing the flow are Barbados, Sandwich, the Apennines, the Carpathians, Banda, Molucca, Tonga, Kermadec, the Marianas, Izu–Bonin, Nankai, the Philippines, Kurili and the Aleutians. The Japan subduction appears to be a transitional subduction zone.

The W-directed slabs are generally very steep (up to 90°; on average 66°) and deep, apart from a few cases such as in Japan. They have a cogenetic backarc basin, and the related single verging accretionary prism has a low elevation (e.g. Barbados, Sandwich and Nankai), is mostly composed of shallow rocks, and has a frontal deep trench or foredeep (Doglioni et al., 1999a,b). The E- or NE-directed subduction zones are less inclined (15–70°; on average about 27°) and the seismicity generally dies at about 300 km, apart from some deeper clusters close to the upper-lower mantle transition (Omori et al., 2004), not necessarily indicating the presence of slab fragments (Varga et al., 2012). The related orogens have high morphological and structural elevation (e.g. the Andes, the Himalayas, and the Alps), wide outcrops of basement rocks, and two shallower trenches or foredeeps at the fronts of the double verging belt, i.e., the forebelt and the retrobelt. The retrobelt decreases its development when the upper plate is subject to extension (e.g. Central America and the Aegean and Andaman seas).

Royden (1993) proposed that asymmetry of subduction zones is related to a convergence rate faster or slower than the slab retreat. Doglioni et al. (2006) instead suggested that the subduction system is primarily sensitive to the behavior of the subduction hinge, i.e., whether it is moving towards or away from the upper plate, regardless of the convergence rate. The subduction rate is faster than the convergence rate where the hinge migrates away from the upper plate, and slower than the convergence where the hinge converges or advances toward the upper plate. The two end members appear sensitive to the geographic polarity of the subduction zones, the asymmetry being not among E–W subduction zones, but along the tectonic equator, following or opposing the "westerly" directed lithospheric flow (Doglioni, 1993), validated by space geodesy and statistical analysis (Crespi et al., 2007). This tectonic mainstream implies a relative mantle counterflow "eastward" directed.

6.3. Influence of the transition of the subduction polarity of the Indian Plate

6.3.1. Tracing the crust/lithosphere/asthenosphere boundaries between the Indian and Eurasian plates

Since Argand (1924) presented the model of underthrusting of the Indian shield beneath the Qinghai–Tibet Plateau, subduction has been considered to be a major mechanism in the uplift and evolution of the plateau. After Panza and Mueller (1979) and Mueller and Panza (1986) provided geophysical evidence for continental lithosphere subduction in continent–continent collision in the Alpine domain, some collision models for the Indian Plate and the Eurasian Plate interaction were proposed. These models are constructed to interpret the north–south strong crustal shortening and vertical thickening of the highest plateau in the world and fall into two main categories: (1) those in which the Indian lithosphere is subducted

under the Qinghai–Tibet Plateau (Zhao and Morgan, 1985; Powell, 1986), and (2) those in which the stronger Indian lithosphere acted as a rigid indenter and resulted in the thickening of the lithosphere of the Qinghai–Tibet Plateau (Dewey et al., 1988; England and Houseman, 1988; Dewey et al., 1989; Willett and Beaumont, 1994).

By combining the shear wave velocity cross-sections (Fig. 9b–f) along the profiles A–A′, B–B′, C–C′, D–D′, E–E′, F–F′ and G–G′, oriented in accordance with the direction of the global mantle flow (Crespi et al., 2007; Panza et al., 2010; Riguzzi et al., 2010) and consistent with the dominant characteristics seen in group velocity tomographic maps, such as the NW–SE directed low velocity anomaly in the Qinghai–Tibet Plateau, it has been possible to compile a section that shows the Moho and the lithosphere–asthenosphere boundary (LAB) boundaries between the Indian and Eurasian plates (J.M. Zhao et al., 2010). From the profiles crossing the Main Boundary Thrust (MBT) it can be seen that the uppermost upper mantle of the Indian Plate is clearly subducted almost horizontally beneath the Himalaya (HM) and the Lhasa Block (LS) and underthrust as far as around the Bangong–Nujiang suture (BNS). Similar results for the mantle boundary or LAB between the Indian and Eurasian plates can be found in recent receiver function images along the west and the central N–S profiles across the Tibetan Plateau (J.M. Zhao et al., 2010). The combined interpretation of all wide-angle seismic profiles in the Tibetan Plateau indicates that, at the crustal level, the boundary between India (subducted) and Eurasia mimics the LAB boundary (Zhang et al., 2011e), as shown by our Vs and ρ models.

6.3.2. Does the Indian Plate subduct beneath the Himalaya as a low angle slab?

It is still unclear whether the Indian Plate is subducting beneath the Himalaya steeply or gently. A deep seismic sounding survey in the Kashmir Himalaya (Kaila and Narain, 1976) showed the Moho dipping toward the north–northeast, at an average angle of 15°–20°. Hauck et al. (1998) and Schulte-Pelkum et al. (2005) proposed that the Moho dips with an angle of a few degrees northwards beneath the Sub and Lesser Himalaya and steepens to about 15° beneath the Greater Himalaya. Tiwari et al. (2006) suggested that the MBT and MCT dip with an angle of about 22° and about 16° to the north, respectively. Reinterpretation of the Sino-French joint west–east wide-angle seismic profile in the Himalaya indicates that the Indian Plate subducts or subducted beneath the Himalaya as a low-angle subduction slab (~8.5°) but may have undergone a transition from steep subduction to low-angle, gentle subduction (Zhang and Klemperer, 2010).

The S-wave models along different profiles (Fig. 9), going from west to east, show the following features: (1) to the south of the Indus–Yarlung–Zangbo suture (IYS), the crustal thickness exceeds 70 km in the Himalaya Block. The Moho interface is 73–79 km deep (average is about 76 km) in the east; in the west it is 70–78 km deep, with an average of about 73 km. (2) The depth of the Moho interface increases northward; in the south of the study area, the Moho interface is discontinuous near the sutures when moving from the eastern to the western profiles. Near the Yarlung–Zangbo suture, the following features can be observed.

(1) To the south of the IYS, the Moho interface is 73–79 km deep (average depth 76 km) to the east, and to the west it is at 70–78 km of depth, with an average of 73 km, i.e., the depth of the Moho interface is deeper to the east than to the west. For example, the Moho is at 78 km depth in the east (Pumoyong Cuo, the distance is 70 km along the Yadong–Namu Cuo profile) and 70 km in the west (Peigu Cuo) (Zhang and Klemperer, 2010); the whole Moho interface shows that the crustal thickness of the Himalaya Block thins from east to west and deepens northward.
(2) The derived lateral variation in the subduction angle of the crust (Fig. 9b) is in good agreement with the ρ structure, which extends to a depth of 350 km, as shown in Fig. 13a–f. In these figures, the relative higher density layer (~3.3 g/cm3) is interpreted as the mantle lid, the thickness of which is almost constant of around 100 km to the south to the Yarlung–Zangbo suture, increasing beneath the IYS and reaching 150–200 km beneath the LS, QB and SB blocks. Considering the possible uncertainties of the subducting angle, we suggest that the slip angle is ~15° on the western part of the Tibetan Plateau, and is <10° towards the east.

The surface wave tomography results (Fig. 9) demonstrate the lateral (west–east) variation in the geometry of the Indian lid subduction: the Indian lid is subducted at a large angle beneath the Eurasian plate just before the Yarlung–Zangbo suture (IYS) to the west of 82°E, but with a small angle towards the east. In the lithosphere of the Qinghai–Tibet Plateau the crust is very thick, with low velocity in its lower part, and the lithospheric mantle is thin. A double-crust structure is not detected in the Qinghai–Tibet Plateau. We reiterate the view of Le Pichon et al. (1992), who considered that the Indian lower crust is not preserved in the Himalayan thrust sheets. The crust of the Qinghai–Tibet Plateau is twice as thick as the average continental crust (60–80 km) with an abnormal thermal state, resulting from the continent crustal convergence due to the collision and compression of the Indian and Eurasian plates. The upper part of the Indian crust has been removed by erosion along the Himalayan front (Zhao and Morgan, 1985). In contrast, the lithosphere is relatively thin in the central Qinghai–Tibet Plateau, above a thick metasomatic lid; indeed, north of the BNS large portions of metasomatic lid are widely present. The low-velocity lower crust and the metasomatic lid, detected in the central Qinghai–Tibet Plateau, show that in the QB Block the relatively low velocities could be associated with high temperatures and/or the fluids released by dehydration of the subducting slab, consistent with the active Cenozoic volcanism in the area. The doubling (superposition) of the upper (Asian) and lower (Indian) plates can account for the uplift of the Qinghai–Tibet hinterland.

This lateral variation, from steep subduction beneath the west to the gentle subduction in the central and eastern Himalaya, is consistent with the exposure of ultra high-pressure metamorphic rocks to the west, while only high-pressure rock exposures are found in the central and eastern Himalaya. This is also supported by the recent numerical modeling of small- and large-angle subduction of the Indian Plate beneath the Tibetan Plateau (Li et al., 2008). The origin of this west–east difference in the subduction angle of the Indian slab is still unclear, but most studies are focused on the Indian crust or lithosphere itself and neglect a possible key contribution from the eastward mantle flow (e.g. Doglioni et al., 1999a,b).

In addition to the temporal variation in the convergence rate between the Indian and the Eurasian plates (equivalent to the lateral variation of the two plates' convergence rate between the west and the east of the Himalaya), the contribution from mantle flow should be taken into account, in particular the subduction asymmetry of the W-directed on one side and E- and NE-directed plates (Doglioni et al., 1997, 2007, 2009; Panza and Raykova, 2008; Panza et al., 2010) on the other. It is thus reasonable to speculate that the subduction of the Indian Plate may have experienced such a polarity variation from W-directed beneath the western Himalaya, to E- and NE-directed subduction in the central and eastern syntaxis of the Tibetan Plateau. This possible variation of the subduction polarity of the Indian Plate may indicate the west–east difference in convergence rate between the Indian and Eurasian plates, and then leads to the west–east variation of the leading edge of the subducting slab. Receiver function imaging (Hetényi et al., 2007; J.M. Zhao et al., 2010) and seismic traveltime tomography (Li et al., 2008) suggest that the Indian lithosphere passes through the whole of the plateau at the west, and is in contact with the Tarim Basin at the north end, but terminates south of the Bangong–Nujiang suture at the central and final part of the plateau. Combining all these results, we speculate that the lithospheric mantle is decoupled from its crust at the west; in other words the Indian

crust has been injected into the whole Tibetan Plateau at a small angle, and the Indian lithospheric mantle subduction at a large angle is terminated by the Yurlung–Zangpo suture. This steepening of the Indian lithospheric mantle produces the thick metasomatic lid (as observed in surface wave tomography, Fig. 9) before the Yarlung–Zangbo suture, which enhanced the deformation ability and provided favorable conditions for the far-reaching injection of Indian crust into the plateau. The Hindu Kush and the Pamir seismic region, characterized by high concentrations of intermediate-depth seismicity, further support this speculation. These intermediate-depth events trace the Wadati–Benioff zone, which dips to the north under the western and central parts of the Hindu Kush and southwards under the Pamir. Earthquake studies in the region show that seismicity extends to a depth of about 300 km. Our surface wave tomographic result is consistent with the inferences from surface wave tomography made by Brandon and Romanowicz (1986) and the interpretation of the gravity field (Molnar, 1988; Burov et al., 1990). These results indicate that the Moho reaches about 70 km of depth in the Pamir, and suggest the injection of the Indian crust through the whole of the western Tibetan Plateau (Zhang et al., 2011e).

6.4. The lower crust beneath the Himalaya and Lhasa: is it eclogitizing now or was it eclogitized?

Previous studies have shown that eclogitization of the lower crust is a key process in support of the high elevation of both the Himalayas and Tibet (Bousquet et al., 1997; Henry et al., 1997; Cattin et al., 2001; Tiwari et al., 2006; Hetényi et al., 2007. In the north of the Himalaya, the lower Indian crust is characterized by a high-velocity region consistent with the formation of eclogite and a high-density material, the presence of which affects the dynamics of the Tibetan Plateau (Schulte-Pelkum et al., 2005). However, several seismic studies have inferred abnormally low, rather than increased, velocities for the Tibetan lower crust (Cotte et al., 1999; Zhao and Helberger, 1991; Zhao et al., 1996), thus suggesting the absence of eclogite. It is also worth mentioning that there are still different observations and arguments to support or reject the model of eclogitization in the lower crust of Tibet. Firstly based on a receiver function study and observed fast Vp in the lower crust, Schulte-Pelkum et al. (2005) argued that the lower crust is partially (~30%) eclogitized just south of the IYS, and that the eclogitization process is governed by water availability. This implies that the lower-crust material reaches the eclogite facies via granulite facies conditions, as shown by Le Pichon et al. (1997) for geotherms established after more than ~20 Ma of relaxation. However, the latter study also showed that the geotherm may follow an amphibolite–eclogite and even a blueschist–eclogite path for shorter relaxation times, between ~10 and 20 Ma and less than ~10 Ma, respectively. Secondly, based on thermo-kinematic modeling, Henry et al. (1997) proposed that the high altitude of the Himalayas is related to the absence of eclogites beneath the mountain range. Eclogites would not have been formed due to the fast rates of underthrusting of relatively cold material. Thirdly, another kind of support for the eclogized lower crust model comes from studies in the LB (Cattin et al., 2001; Tilmann et al., 2003; Tiwari et al., 2006). Seismic tomography of the upper mantle in central Tibet revealed a sub-vertical high velocity zone beneath the northern LB block that probably represents the detachment front of the Indian mantle lithosphere (Tilmann et al., 2003). Fourthly, based on gravity data combined with numerical modeling of the gravity anomaly, Cattin et al. (2001) showed that eclogitization does not take place under the High Himalayan range as expected from a steady-state local equilibrium assumption, but instead further north beneath the Tibetan Plateau. More recently, Tiwari et al. (2006) showed that gravity and magnetic anomalies across Sikkim can be explained with a model in which the crust beneath Tibet (between 56 and 72 km depth) is eclogitized ~100 km north of the IYS. In the following section, based on the density and composition of the lower crust, we provide evidence against the absence of eclogitization in the lower crust beneath the Himalaya and Lhasa.

6.4.1. Evidence from lower crustal density

Eclogite is characterized by very high seismic velocities (Vp > 7.5 km/s, Vs > 4.3 km/s) and $\rho > 3.2$ g/cm^3. Eclogitization of the lower crust can be inferred from its density. In order to evaluate the presence of eclogitized lower crust, we designed a ρ model (Model III) for the crust (Fig. 10b) with eclogite in the lower crust, keeping the same geometry as in the Model II described in Section 5.2. When including the lower crust beneath the HB and LB blocks with $\rho > 3.3$ g/cm^3, the calculated gravity anomaly is obviously larger than the observed Bouguer anomaly. In order to match the calculated anomaly with the observed data, ρ is reduced in the lower crust: the result obtained with $\rho < 3.2$ g/cm^3 in the lower crust is shown in Fig. 10d. Model IV was preferred following several tests using a trial-and-error approach. The calculated Bouguer anomaly is in good agreement with the observed data, with the exception of a few local misfits. The main negative anomalies at the contact zone between the Indian and Eurasian plates are properly reproduced compared with Model III. A concentration of residuals around zero with a standard deviation is 29.45 mGal, the correlation coefficient between the observed and calculated gravity anomaly data is 0.9 (S.F. Zhang, 2010). According to the modeled ρ structure, our result shows $\rho < 3.2$ g/cm^3 in the lower crust, in contrast with the expected high Vp (6.8–7.6 km/s) and high ρ (3.15–3.6 g/cm^3) in the lower crust if eclogite were present (Mengel and Kern, 1990). This suggests the absence of eclogite or partial eclogitization due to delamination under central-south Tibet.

6.4.2. Evidence from crustal composition modeling

In addition to indirect evidence such as seismic velocities and density, in order to verify the presence of eclogite in the lower crust, one direct piece of evidence is its composition. In order to derive a crustal composition model we compared the values of our models with laboratory measurements of ultrasonic velocities and densities, which are generally performed at room temperature (Brown et al., 2003; Zhang et al., 2008; Zhang and Wang, 2009; X. Zhang et al., 2011; Zhao et al., 2013). We calibrated all Vp (Hirn et al., 1984a,b; Teng et al., 1985a,b; Min and Wu, 1987; Makovsky et al., 1996; Makovsky et al., 1999; Zhang and Klemperer, 2005, 2010; Zhang et al., 2011b) to a standard pressure of 600 MPa and room temperature (Christensen and Mooney, 1995). The crustal temperatures were estimated from thermal modeling results (Hetényi et al., 2007; Jiménez-Munt et al., 2008) and the pressure in each layer was determined by its depth and density, obtained from gravity modeling. The pressure in the deep crust can be calculated easily by the formula $P = \rho g z$, where ρ has been obtained by gravity modeling, g is the acceleration due to gravity (assumed to be 9.81 m/s^2), and z is depth. Vp and ρ corrected for the pressure and temperature field for each layer can be compared with laboratory measurements of ultrasonic velocities, which are generally performed at room temperature. Table 4 lists the published velocities for the units used in the compilation, as well as the P-wave velocities (Vp).

Fig. 17a shows the calculated densities and velocities for the different bodies of the study area and laboratory data set. Every line corresponds to one of the bodies of our density model (see Fig. 10d). As shown in Fig. 17b, metagraywacke (MGW), andesite (AND) and granite–granodiorite (GRA) are the main components of QU8. Although the curves of granite–granodiorite (GRA), granite–gneiss (GGN) and quartzite (QTZ) are around the lines of LU6 and IU2, the velocities of quartzite (QTZ) are lower than the calibrated velocities of LU6 and IU2. We therefore consider that LU6 and IU2 are respectively composed of granite–granodiorite (GRA) and granite–gneiss (GGN). The gravity anomaly is greater in the Himalaya than in Tibet, so if we assume that there are no lateral variations in ρ in the middle crust, lower crust and upper mantle, the material forming the Himalaya is, on average, denser than that making up Tibet. According to Fig. 17b, the composition of HU6 is denser than LU6 and QU8 beneath Tibet, and is possibly composed of biotite (tonalite) gneiss (BGN) and pyroxenite (PYX). Paragranulite

Table 4
Physical parameters of the different bodies used in the ρ modeling. We give the name of the body, ρ (rounded off to 0.05 g/cm^3), the published in situ velocity (rounded off to 0.05 km/s), the temperature, and the calibrated velocity (rounded off to 0.05 km/s).

Unit	ρ	Vp	Temp.	Vp′
	(g/cm^3)	(km/s)	(°C)	(km/s)
IS1	2.55	**3.60–4.6**	50–150[a]	3.70–4.75
IU2	2.7	**5.9–6.5**	150–250[a]	6.05–6.65
HU3	2.75	>5.7 (Hauck et al., 1998)	<400	>5.90
HM23	2.9	**6.5**	<600[a,b]	6.70
HS4	2.65	**4.2–5.3**	**50–180**	4.30–5.45
HS34	2.65	**4.2–5.3**	**50–180**	4.30–5.45
LU6	2.7	6–6.5 (Meissner et al., 2004; Zhao et al., 2001c) 6–6.25 (Haines et al., 2003a,b)	<600[b]	6.2–6.70
LM26	2.9	6.5–6.75 (Haines et al., 2003a,b) 6.5–6.7 (Meissner et al., 2004)	800[b]	6.70–6.85
QS7	2.5	4–5 (Haines et al., 2003a,b)	<200[c]	4.15–5.15
QS37	2.6	4–5 (Haines et al., 2003a,b)	<200[c]	4.15–5.15
QU8	2.65	~5.8–6.2 (Meissner et al., 2004) ~5.6–6.5 (Zhao et al., 2001c) 5.7–6.1 (Haines et al., 2003a,b)	200–600[a,b]	5.75–6.75
QM28	2.90	6.65–6.85 (Haines et al., 2003a,b)	800[b]	6.95–7.10
IL13/132 /134/135	2.9/3.0 3.05/3.1	**6.7**	350–450[a,b]	6.9
HL14/214	3.0, 3.2	**6.9–7.3**	700–800[c]	6.95–7.45
LL15/215	3.0, 3.15	6.6–7.1 (Meissner et al., 2004) 7–7.3 (Zhang and Klemperer, 2005) 6.5–7.3 (Zhao et al., 2001c)	1000–1100[c] 700–800[b]	6.8–7.2
LL315	3.05	6.6–7.1 (Meissner et al., 2004) 7–7.3 (Zhang and Klemperer, 2005) 6.5–7.3 (Zhao et al., 2001c)	1000–1100[c] 700–800[b]	6.8–7.2
QL16	3.0	6.6–7.1 (Meissner et al., 2004) 7–7.3 (Zhang and Klemperer, 2005) 6.5–7.3 (Zhao et al., 2001c) 7.1 (Haines et al., 2003a,b)	1000–1100[c] 700–800[b]	6.8–7.2

Descriptions of each unit: IS1—Indian foreland basin; IU2—Indian upper crust; HU3—Himalaya upper crust; HM23—Himalaya middle crust; HS4—Himalaya sediments; HS34—north Himalaya sediments; LU6—Lhasa block upper crust; LM26—Lhasa block middle crust; QS7—Qiangtang block sediments; QS37—north Qiangtang block sediments; QU8—Qiangtang upper crust; QM28—Qiangtang middle crust; CM29 Chaidam middle crust; IL13, IL132, IL134, IL135—Indian lower crust; HL14—Himalaya lower crust; LL15—Lhasa block lower crust; LL315—north Lhasa block lower crust; QL16—Qiangtang lower crust; QL316—Chaidam lower crust; M17—upper mantle; CM9—Chaidam upper crust. Black body texts for Vp are deduced from Vs from Mitra et al. (2005).
[a] Brewer et al. (2003).
[b] Hetényi et al. (2007).
[c] Jiménez-Munt et al. (2008).

(PGR) and felsic granulite (FGR) are excluded, since their ρ is higher than that of HU6. For the middle crust, the calibrated middle crustal velocities are higher than those of rock types whose densities are around the range of QM28, HM23 and LM26 (see Fig. 17c). We cannot estimate the composition of these middle crustal units, and so the data set of Rudnick and Fountain (1995) were used for further comparison. Fig. 18a shows the calculated densities and velocities for the different bodies of the study area and the laboratory data set of Rudnick and Fountain (1995). As shown in a zoomed figure (Fig. 18b) of Fig. 18a, the middle crust has an intermediate granulite facies composition and might be composed of pelitic gneisses. For the lower crust, as seen in Fig. 17d, the lower crustal rocks of IL13, HL14, LL15 and QL16 are possibly a mixture of gabbro–norite–troctolite (GAB), mafic granulite (MGR) and diabase (DIA). Amphibolite (AMP) and greenschist facies basalt (BGR) are also excluded, because of their high densities. However, AMP and BGR might make up IL134, LL215 and LL315.

From the composition in the lower crust beneath HB and the south of LB, we could not find evidence to support the presence of eclogite in the lower crust. This is also reinforced by the crustal composition model along the INDEPTH-3 profile across the Bangong–Nujiang suture (X. Zhang et al., 2011).

6.5. Crustal responses to lithospheric disruption

6.5.1. Lateral variation of crustal responses to the lithospheric disruption of the North China Craton

Many of the Archean terranes over the globe with ages ranging up to 3.8–4.0 Ga are dominantly composed of tonalite–trondhjemite–granodiorite (TTG) gneisses with or without minor volumes of meta-supracrustal rocks and meta-gabbros (e.g. Nutman et al., 1993, 2000). The major event of formation of TTGs around 2.9–2.7 Ga contributed to the generation of large volumes of juvenile crust, and the TTG rocks were probably derived from the partial melting of mafic (or possibly oceanic) protoliths accompanied by varying degrees of interaction with mantle peridotite (e.g., Martin et al., 2005; Smithies et al., 2007; Huang et al., 2013). On the other hand, granitic gneisses, which form the common constituents of continental crust, were mostly derived from intermediate-felsic rocks as well as sedimentary protoliths by partial melting. Condie et al. (2001) and Condie (2001, 2004) suggested a Neoarchean plume model to interpret the formation of TTGs during 2.9–2.7 Ga, and correlated them to a large igneous province with associated basalt–komatiite suites. The amalgamation of continental fragments at ca. 2.5 Ga into a supercraton (Arctica or Kenorland) has also been proposed (e.g. Rogers and Santosh, 2003, 2004). However, the mechanism of aggregation of the early Precambrian continental blocks to form a supercraton is uncertain, and the various models proposed take into consideration rifting, ρ inversion, back arc basin formation, arc–arc accretion, subduction of oceanic lithosphere, and arc–continent or continent–continent collision (Windley, 1973; Jordan, 1978; Arndt, 1983; Nisbet, 1987; Hoffman, 1988; Kusky, 1990; Mitchell, 1991; Kröner and Layer, 1992; Windley, 1993, 1995; Goodwin, 1996; Condie, 2000; Eriksson and Catuneanu, 2004; Kusky et al., 2004a,b; Santosh et al., 2007a,b, 2010, 2013). The driving mechanism of these processes is debated within varying models of intra-continent tectonics, plume tectonics and plate tectonics (Manikyamba and Kerrich, 2012; Condie and Aster, 2013).

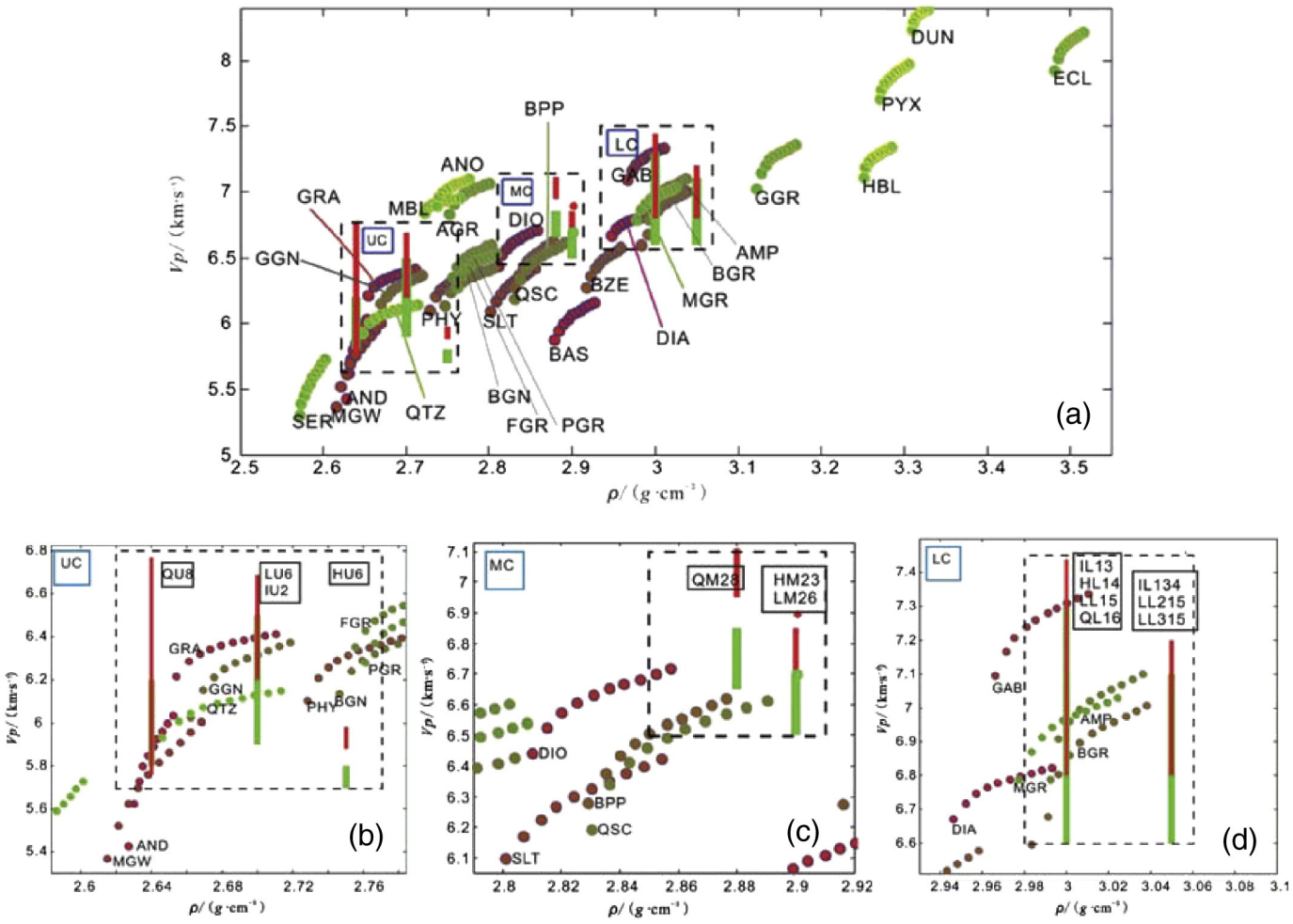

Fig. 17. (a) Vp–ρ relations. Thick green segments show ρ obtained with gravity modeling and the range of published Vp; thick red lines show the calibrated values of Vp at room temperature and 600 MPa pressure. Filled circles represent ρ and Vp for 29 rock types at room temperature and 600 MPa pressure. Dashed rectangles show the cluster of different crustal layers: UC is the upper crust, MC the middle crust and LC the lower crust. Rock types are: andesite (AND), basalt (BAS), diabase (DIA), granite–granodiorite (GRA), diorite (DIO), gabbro–norite–troctolite (GAB), metagraywacke (MGW), slate (SLT), phyllite (PHY), prehnite–pumpellyite facies basalt (BPP), greenschist facies basalt (BGR), granite–gneiss (GGN), biolite (tonalite) gneiss (BGN), mica quartz schist (QSC), amphibolite (AMP), felsic granulite (FGR), paragranulite (PGR), anorthositic granulite (AGR), mafic granulite (MGR), serpentinite (SER), quartzite (QTZ), zeolite facies basalt (BZE), mafic garnet granulite (GGR), mafic–eclogite (ECL), calcite marble (MBL), anorthosite (ANO), hornblendite (HBL), pyroxenite (PYX), dunite (DUN). Blow up of part of (a): (b) upper crust (UC), (c) middle crust (MC) and (d) lower crust (LC). IU2: Indian upper crust; HU6: Himalaya upper crust; HM23: Himalaya middle crust; LU6: Lhasa terrane upper crust; LM26: Lhasa terrane middle crust; QU8: Qiangtang upper crust; QM28: Qiangtang middle crust; IL13, IL134: Indian lower crust; HL14: Himalaya lower crust; LL15, LL215: Lhasa terrane lower crust; LL315: north Lhasa terrane lower crust; QL16: Qiangtang lower crust.

In order to reveal crustal responses to lithospheric destruction, especially west–east differences in crustal response, we constructed a west–east transect (Wen'an–Chayouzhongqi) showing lateral variations in Vp, Vs and Vp/Vs ratio (Fig. 19). The Vp/Vs ratio is usually higher beneath the western NCC and the western portion of the central NCC than beneath the eastern NCC and the eastern portion of the central NCC. Such a pattern probably means that: (1) the lateral variation of the crustal response to the lithospheric disruption, and the leading

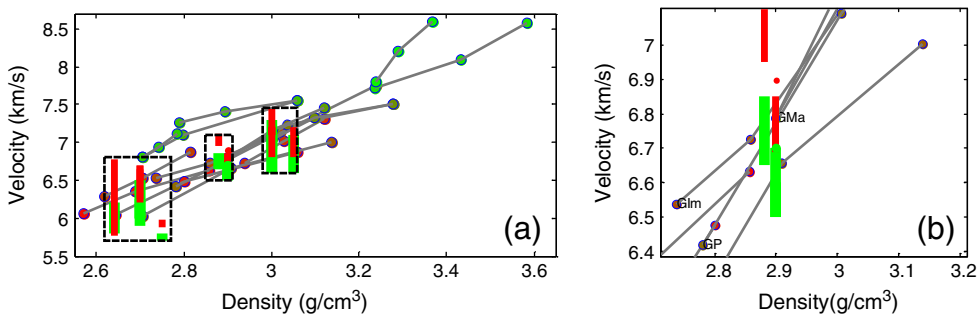

Fig. 18. (a) Same as Fig. 17, thick green lines show ρ determined from gravity modeling and the range of published Vp and thick red lines show the calibrated values of Vp at room temperature and 600 MPa pressure. Filled circles represent the densities and velocities at room temperature and 600 MPa pressure from the data set of Rudnick and Fountain (1995). (b) Blow up of part of (a) for the middle crust. (GMa indicates mafic granulite facies, Glm intermediate granulite facies, and GP pelitic gneisses). From the figure it can be inferred that the middle crust has an intermediate granulite facies composition and may be composed of pelitic gneisses.

edge of the lithospheric disruption is confined to the middle of the central NCC and (2) this lateral variation is a relic consistent with the fact that the 1.85 Ga continent–continent collision was asymmetrical, as required by the double-sided subduction model. The two layers with the lowest Vs beneath the western NCC observed by Zhu and Zheng (2009) are suggested to be seismic signatures of the 1.85 Ga continent–continent westward subduction (Santosh, 2010).

The Vs crustal velocity model in North China reveals the thickness of the sedimentary cover and the lateral variation of the Moho interface very well. The thickness of the sedimentary cover is less than 2 km in the Taihangshan and Yanshan horsts, about 5 km in the Yanqing–Huailai Basin and about 3 km in the Datong Basin. The thickness of the sedimentary cover in the NCP is more than 6 km and has lateral variation corresponding to different tectonic units. The thickness of the sedimentary cover is about 8 km in the Cangxian Horst and about 11 km in the Jizhong and Huanghua depressions. The Moho depth is larger in the western part than in the eastern part: the crustal thickness increases from 28 km in Bohai Bay to 44 km in Zhangjiakou.

The maps of Vs at different depths show that the Taihangshan Fault is a boundary between high and low velocity in the 0–12 km depth range, while the region below the boundary between high and low velocity is visible only at some parts of the Taihangshan Fault. We infer that the Taihangshan Fault only extends to the Moho interface in some regions. From 0 to 8 km, the Yanshan Uplift is mapped as a broad high velocity body, while its southern margin is mapped as an alternation of high and low velocity bodies, which may be caused by the NNE–NE trending faults. There is a distinct low velocity belt, with a NW trend and at a depth of 10 km, near the Zhangjiakou–Bohai seismic zone. This low velocity belt and the southern margin of the Yanshan high velocity body outline the Zhangjiakou–Bohai seismic zone and its northern broader boundary. There is a well-defined low velocity zone in the middle to lower crust (15–25 km) in the Beijing–Tianjin–Tangshan region, which may be caused by the intrusion of hot mantle materials.

The described pattern of sedimentary thickness, Moho depth and Vs at different depths demonstrates that the present configuration of the NCC can be divided into three parts: western, central and eastern. However, whether the popular Precambrian tectonic subdivision of the NCC into the Eastern and Western Blocks with the intervening Trans-North China Orogen is preserved wholly or partly in the Mesozoic remains equivocal.

The tomographic maps show two further important characteristics: (1) a high velocity zone near Datong, Shouzhou and Qingshuihe and (2) a strong velocity gradient adjacent to the boundary between the NCP and the Yanshan–Taihangshan Uplift. The zone with high velocity Rayleigh waves near Datong, Shouzhou and Qingshuihe is located at the northeastern margin of the Ordos Block, which shows characteristics typical of a cratonic lithosphere that has not been affected by the reactivation of the NCC. The block is characterized by low seismicity, low heat flow, a positive vertical velocity gradient and a lack of active fault and magmatic activity (Qiu et al., 2005). The trend of a strong horizontal gradient in velocity seen near the boundary of the NCP and the Yanshan–Taihangshan Uplift mimics that visible in the Bouguer gravity anomaly map (Yin et al., 1989), where along the NE–SW-trending Taihangshan Uplift, a continuous gradient zone is noticeable. The Taihangshan Fault is within this gradient belt, and P-wave tomography has shown that the fault cuts through the Moho interface and penetrates into the upper mantle (Huang and Zhao, 2004; J. Zhang et al., 2007). The belt represents a major lithospheric boundary and separates the NCC into western and eastern sectors, probably with fundamental differences in architecture. Gravity anomaly values decrease from east to west; this indicates that the main ρ interface (Moho discontinuity) is deeper in the west. Thus both densities and velocity structures differ greatly on both sides of the Taihangshan Fault.

The various models related to the early Precambrian evolution of the NCC can be summarized as follows.

(1) An ancient ocean separated the Western and the Eastern sub-blocks of the NCC. The oceanic crust subducted beneath the western margin of the Eastern sub-block and closed at about 1.85 Ga, forming the basement of the North China Craton (Zhao et al., 2001a,b). This model was accepted by Wilde et al. (2002), Kröner et al. (2005, 2006), and J. Zhang et al. (2006, 2007, 2009). However, Santosh (2010) showed that the subduction polarity was towards the west, with the Eastern Block subducting beneath the Western Block, and the Yinshan Block subducting towards the Ordos Block in a double-sided subduction realm.

(2) The basement of the NCC formed at about 2.5 Ga; rifting occurred at about 2.4 Ga along the collisonal belt, and the Inner-Mongolia–northern Heibei orogenic belt formed from collisional compression at the northern margin of the NCC at about 2.3 Ga. This led the craton to produce Andean-type deformation between 2.2 and 1.85 Ga and extension around 1.85–1.70 Ga (Kusky and Li, 2003). The amalgamation of the Western and Eastern sub-blocks of the NCC resulted from the subduction of the Western sub-block beneath the Eastern sub-block (as the passive plate) (Kusky et al., 2007; Li and Kusky, 2007).

(3) Three Paleproterozoic continents (Ordos, Fuping and eastern continental blocks) were separated by the Lvliang and Taihang ancient oceans: the Taihang Ocean closed at about 2.1 Ga, when the Fuping continental block subducted beneath the eastern sub-block. Subsequently, the Fuping continental block collided with the Ordos continental block at about 1.9–1.8 Ga, producing the present Central Orogenic Belt (Faure et al., 2007; Trap et al., 2007, 2008, 2009).

In order to understand the lateral variation in crustal structure across the NCC, we collected crustal Vp models produced by west–east deep seismic sounding profiling. The lithospheric thickness was plotted using data compiled from receiver functions, surface wave tomography and gravity inversion (Fig. 20).

From the more detailed description in Zhang et al. (2013c), we can observe that the average Vp in the crust is about 7.0 km/s beneath the Tanlu Fault, and 6.6 km/s beneath the contact belt between the eastern and the central NCC. Correspondingly, the thickness of the seismic layer is 20–25 km beneath the Tanlu Fault, and 15–20 km beneath the contact belt between the eastern and the central NC sub-blocks. These differences in the average crustal Vp and seismic layer thickness are consistent with lateral variation in the amount of lithospheric disruption or the growth of new oceanic lithosphere (Ying et al., 2010; H.F. Zhang et al., 2010). The observation of the foregoing lateral variations (seismogenic layer thickness, average crustal Vp, and Vs) suggest that lithospheric disruption is more significant in the eastern NCC. However, recent numerous passive-source (earthquake) seismic profilings in the western NCC (Chen et al., 2008; Wang et al., 2010; Tian et al., 2011) have found some new evidence for lithospheric disruption. Our Vs distribution beneath the western NCC sub-blocks from ambient noise tomography supports the conclusion that the NCC disruption also occurred beneath the western NCC, based on passive-source seismic profiling (Tian et al., 2011) and finite-frequency traveltime tomography (Zhao et al., 2009).

The NCC is a unique craton that developed a thick lithospheric root in the Archean, half of which was lost during the Phanerozoic (Menzies et al., 2007; Zhai et al., 2007; Zhai and Santosh, 2011). The removal of the lithospheric mantle, and its transitional properties (from continental to oceanic), may be attributed either to lithospheric delamination (Wu et al., 2003; Gao et al., 2004) or to thermal erosion (Xu, 2001; Y.F. Zheng et al., 2003), or to both these mechanisms (Zhu and Zheng, 2009). The west–east variation in the nature and intensity of lithospheric disruption was recognized from receiver function analysis (Chen et al., 2008), and surface/body wave tomography (Zhu and

Zheng, 2009) as well as from petrological and geochemical studies (Wu et al., 2003, 2005; J. Zhang et al., 2011). Our results in this study of northwest–southeast variation in seismic activity, crustal P-wave velocity, density and temperature, probably reflect the crustal response to the lithospheric disruption. Our northwest-to-southeast transect across the NCC has revealed pronounced lateral variation, especially beneath the contact zones between the major tectonic blocks such as the Western Block, the TNCO and the Eastern Block, as illustrated in Fig. 20. These variations in crustal geophysical properties are in good agreement with the heterogeneity inferred from geochemical and isotopic studies (e.g. Deng et al., 2013; Li et al., 2013a). Recent petrologic and geochemical studies in the NCC (e.g. J.P. Zheng et al., 2001, 2007, 2008; Wu et al., 2003; H.F. Zhang et al., 2003, 2009, 2010; Wu et al., 2005, 2006; Ying et al., 2006; Xiao et al., 2010; J. Zhang et al., 2009, 2011), show that the low-Mg# lherzolites in this terrane have petrologic and mineralogical affinities with mantle peridotitic xenoliths from the Cenozoic basalts of the NCC and represent the newly accreted lithospheric mantle. In contrast, the high-Mg# lherzolites have petrologic characteristics similar to mantle peridotitic xenoliths from the Archean/Proterozoic lithospheric mantle and represent the remnant old refractory lithospheric mantle. However, the percentages of high-Mg# and low-Mg# peridotites (J.P. Zheng et al., 2007; Xiao et al., 2010; J. Zhang et al., 2011) are variable. The majority of the xenoliths from Qingdao in the eastern part of the Eastern Block of the NCC show high-Mg#, with small amounts of low-Mg# peridotites and Archean lower crust granulites (Zhang and Zhang, 2007), whereas the xenoliths from the Junan area are mainly low-Mg# peridotites, with only one high-Mg# peridotite discovered so far, although abundant lower crustal granulite xenoliths occur here (Xiao et al., 2010). Fertile peridotites are rare in the xenolith suites from the Paleozoic Mengyin and Fuxian kimberlites (J.P. Zheng et al., 2007). In the xenolith suites from Mesozoic–Tertiary basalts, the proportion of fertile peridotites is clearly higher in some localities near the Tanlu fault zone, whereas more refractory components are commonly preserved in distant sites such as Hebi, Fuxin and Kuandian (J.P. Zheng et al., 2007). Thus, the lithospheric mantle beneath the eastern part of the NCC in the Qingdao region is composed of a small amount of newly accreted lithospheric mantle and dominant ancient lithospheric mantle that has been substantially modified. The lithospheric mantle beneath the Junan, Kuandian and Fuxin regions is mainly composed of newly accreted lithospheric mantle, with only a small amount of ancient residue at the top of the upper mantle. All the peridotitic xenoliths entrained in the late Mesozoic basaltic rocks in Qingdao, Daxizhuang and Junan, eastern Shandong, are spinel-facies, and no garnet-facies xenoliths have been found, suggesting that the lithospheric thickness here is less than 75–80 km (Xiao et al., 2010). The Beiyan basalts located within the Tanlu Fault and their entrained peridotites show markedly low olivine Fo values, among which the highest Fo value is close to that of Junan low-Mg# peridotites. This suggests that the lithospheric mantle beneath the Tanlu fault zone is composed of newly accreted lithospheric mantle, whereas that beneath the western NCC preserves the remnants of old lithospheric mantle. Abundant Cpx-rich lherzolites and wehrlites with extremely low Fo (<87) values and high $^{187}Os/^{188}Os$ ratios also occur in the interior of the Tanlu fault zone adjacent to the Beiyan locality, such as in Nushan in Anhui Province (Xu et al., 1998; Xiao and Zhang, 2011) and Shanwang in Shandong Province (Xiao and Zhang, 2011).

The differences in the average crustal P-wave velocity and seismic layer thickness are consistent with the lateral variation in the extent of lithospheric destruction and/or the growth of new oceanic lithosphere (Ying et al., 2010; H.F. Zhang et al., 2010). Knowing the seismic velocity, density and temperature field in the crust (Zhang et al., 2012, 2013b), we can calculate rheological yield stress envelopes as shown in Fig. 21, which also reflect northwest–southeast variation in lithospheric strength (Zhang et al., 2013c). The observation of the foregoing lateral variations, including seismogenic layer thickness, average crustal P-wave velocity, and S-wave velocity and rheological yield stress envelopes, suggests that the lithospheric disruption is more extensive in the Eastern Block of the NCC. The recent passive source seismic profiling in the Western Block of the NCC (Chen et al., 2008; Wang et al., 2010; Tian et al., 2011) has revealed further evidence for lithospheric disruption in the western part. The shear wave velocity distribution beneath the Western Block of the NCC in our study from ambient noise tomography

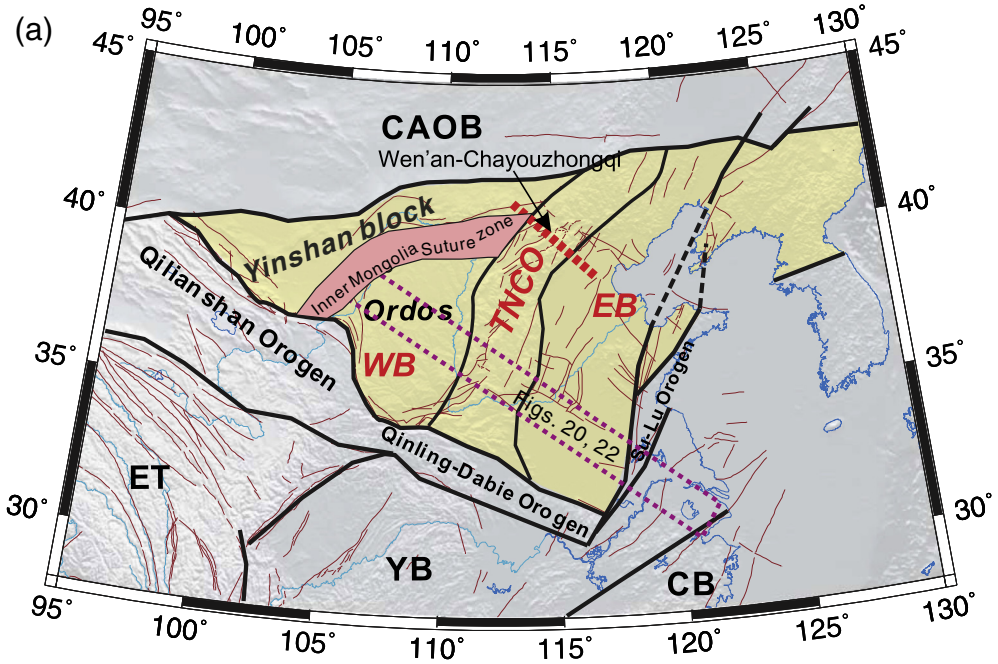

Fig. 19. (a) Position of the Wen'an–Chayouzhongqi profile. WB: Western Block; EB: Eastern Block; TNCO: Trans-North China Orogen; YB: Yangtze Block; CB: Cathaysia Block; ET: Eastern Tibet. The faults are delineated by red lines, the thick dashed red line is the Wen'an–Chayouzhongqi profile; The black solid lines are the tectonic boundary, and the blue lines represent the rivers. The purple rectangle is the region discussed in Figs. 20 and 22. (b) Vp/Vs along Wen'an–Chayouzhongqi profile, (c) Vp (color scale in km/s) and (d) Vs (color scale in km/s) along the profile.

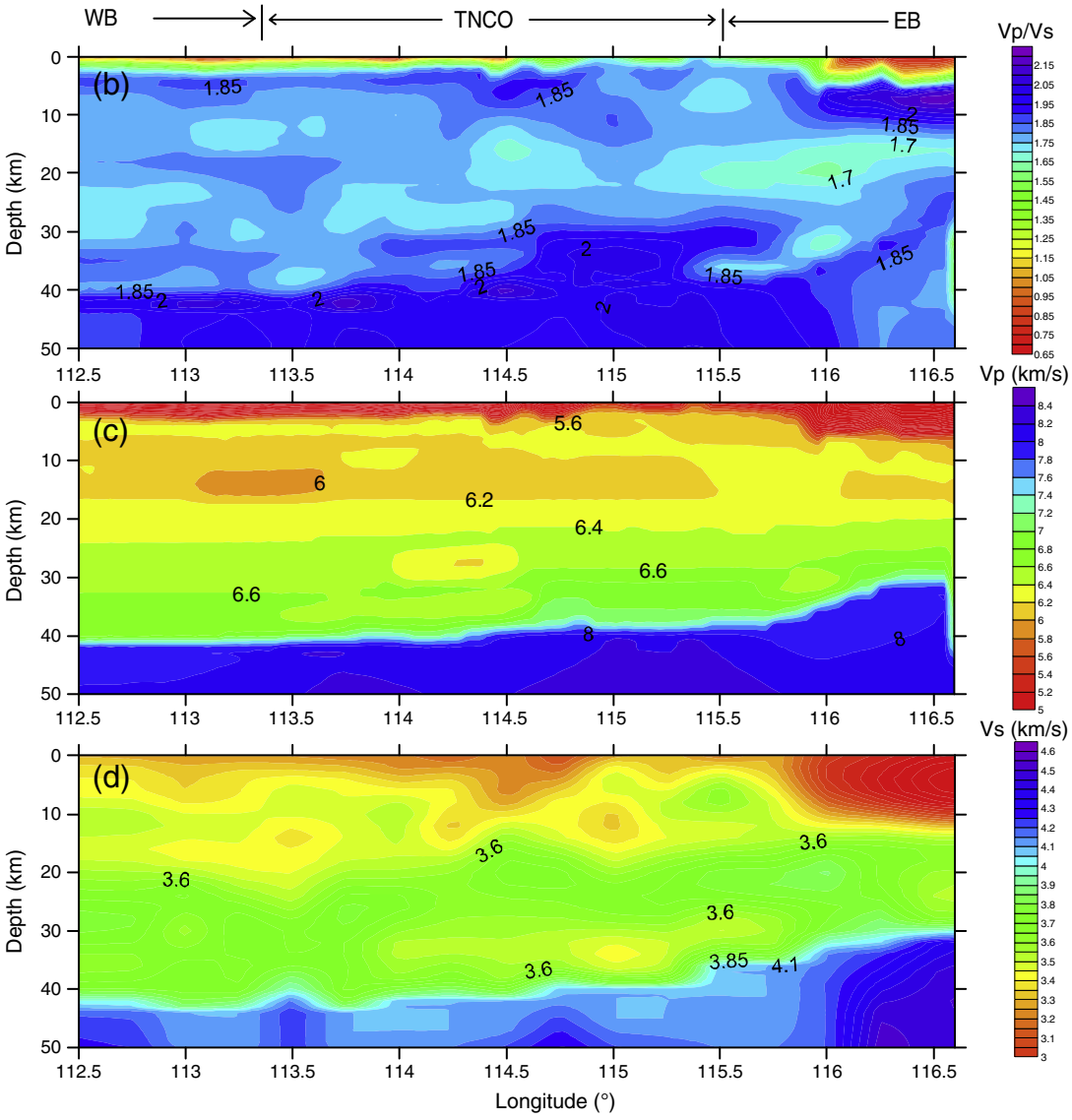

Fig. 19 (*continued*).

also supports the conclusion that lithospheric erosion partly affected the Western Block as well, as also found from passive source seismic profiling (Tian et al., 2011) and finite-frequency traveltime tomography (Zhao et al., 2009). Therefore, the west–east variation in crustal geophysical properties may reflect the strength difference in peridotite–melt reaction (Wu et al., 2006; H.F. Zhang et al., 2010; Xiao and Zhang, 2011) as well as the variation in the degree of lithospheric disruption (Deng et al., 2013).

6.5.2. Evaluation of different mechanisms of lithospheric destruction in the North China Craton

There is still much disagreement on the driving force and mechanism of the Mesozoic lithospheric thinning of the eastern NCC (Menzies et al., 2007). Two thinning models have been proposed: the "top-down" delamination model (e.g. Gao et al., 2004; Deng et al., 2006; H.F. Zhang et al., 2007; Gao et al., 2008) and the "bottom-up" thermal/chemical erosion model (e.g. Niu, 2005; Zhang et al., 2005; J.P. Zheng et al., 2007). The different lithospheric structures in the eastern NCC may provide some information on its past tectonic evolution. From a purely geophysical point of view there are two mechanisms that may stir up the whole lithospheric mantle. The first mechanism is the foundering of the lower crust alone or together with the lithospheric mantle (delamination). Delamination of the continental lithosphere requires a thickened crust and low viscosity (high temperature) in the crust and uppermost upper mantle (Kukkonen et al., 2008). These conditions may have existed in the Mesozoic lithosphere of this area because of the prolonged collisions along the Solonker and Mongol–Okhotsk sutures, a situation similar to some degree to present-day northern Tibet. Geochemical studies have found evidence of foundered lower crust in the NCC (Gao et al., 2004, 2008) and in northern Tibet (Liu et al., 2008). The other mechanism is the asthenosphere rising up to shallow depths through trans-lithospheric faults such as the Tanlu Fault, i.e., the "mushroom cloud" model (e.g. J.P. Zheng et al., 2007). Both mechanisms may bring hot asthenospheric material up to the shallowest mantle, thus effectively reducing the velocity in the top part of the upper mantle.

The lithospheric structure of the northern NCP can be compared to that of northern Tibet (QB) in terms of the abnormally low velocities in the middle crust and upper mantle, implying a similar tectonic setting for their formation. Thus, we may infer that the collision along the Solonker and Mongol–Okhotsk sutures was the main factor in the thinning/modification of the lithosphere of the northern NCP. Conversely, the subduction of the Kula and Pacific plates in late Mesozoic and Cenozoic had a pronounced effect on the tectonic evolution of East

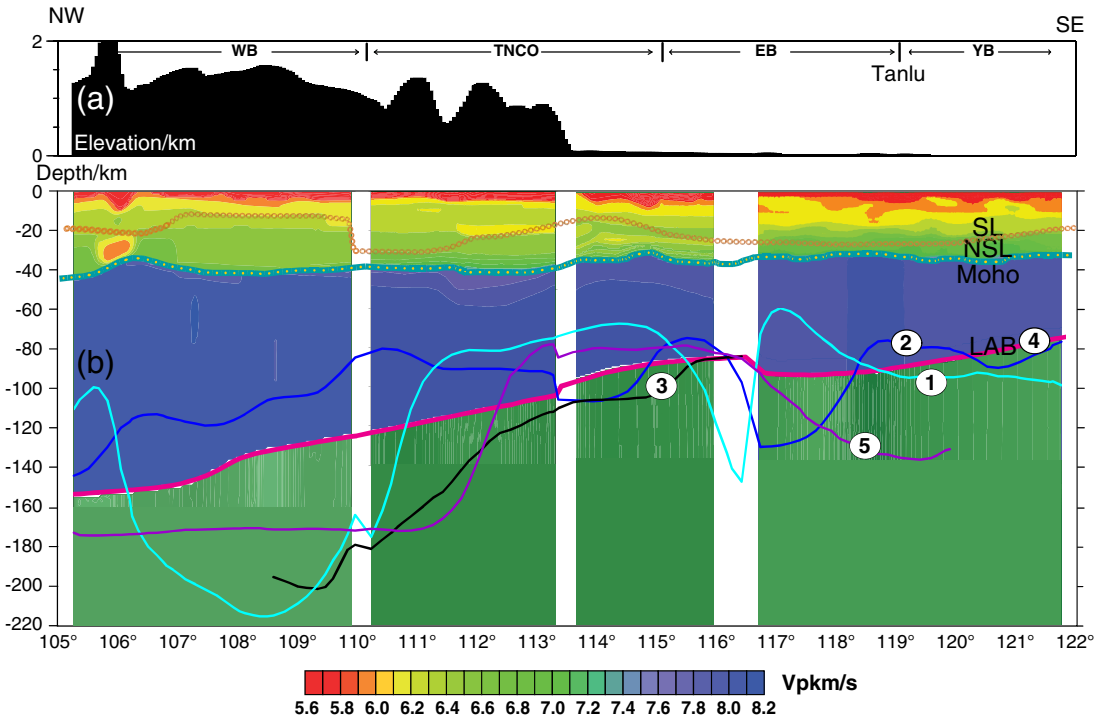

Fig. 20. The west–east transect across the NCC. Top: Topography along the profile Wen'an–Chayouzhongqi. WB: Western Block; EB: Eastern Block; TNCO: Trans-North China Orogen; YB: Yangtze Block. Bottom: Geophysical structures along the lithosphere-scale transect. The crustal velocity structure is compiled by interpreting the results from three wide-angle seismic profiles (Li and Mooney, 1998; Zhang et al., 2011d). The lithosphere bottom (LAB) depth as obtained from gravity inversion (1) (Yuan, 1996a,b), geothermal inversion (2) (Zang et al., 2002), receiver function imaging (3) (Chen, 2010), surface wave tomography (4) (Zhu et al., 1997) and MT (5) (Wei et al., 2006). SL indicates the seismogenic layer (within which 80% of the seismic energy is released) and NSL indicates the BDTL (Brittle/Ductile Transition Layer), the layer between the SL and the Moho discontinuity.

China, especially the marginal seas. This can be seen from the overall decreasing trend in velocity from west to east (Fig. 20), as well as the widespread magmatic rocks and extensional basins in east China (Niu, 2005; Kusky et al., 2007). However, the velocity images show more pronounced characteristics that seem to be related to the tectonic events in the north and south margins of NCC, and we therefore conjecture that the effect of Pacific subduction was secondary. These considerations of the driving forces of lithospheric thinning of the NCC are consistent with the model of Zhang et al. (2003, 2005).

In fact, the NCC has experienced (or is experiencing) the geodynamic effects of the westward subduction of the Pacific Plate, the northward collision of the Yangtze Plate, the southward collision of the Central Asian orogenic belt and the eastward escaping flow of East Tibet. Fig. 22 shows the seismic activity along the west–east transect. Along this transect, a distinctive variation of the seismicity pattern can be observed. In the Eastern Block of the NCC, the seismically active layer is about 10–15 km thick, while it shows as a double vergent distribution pattern in the central orogenic belt of the NCC; very few earthquakes

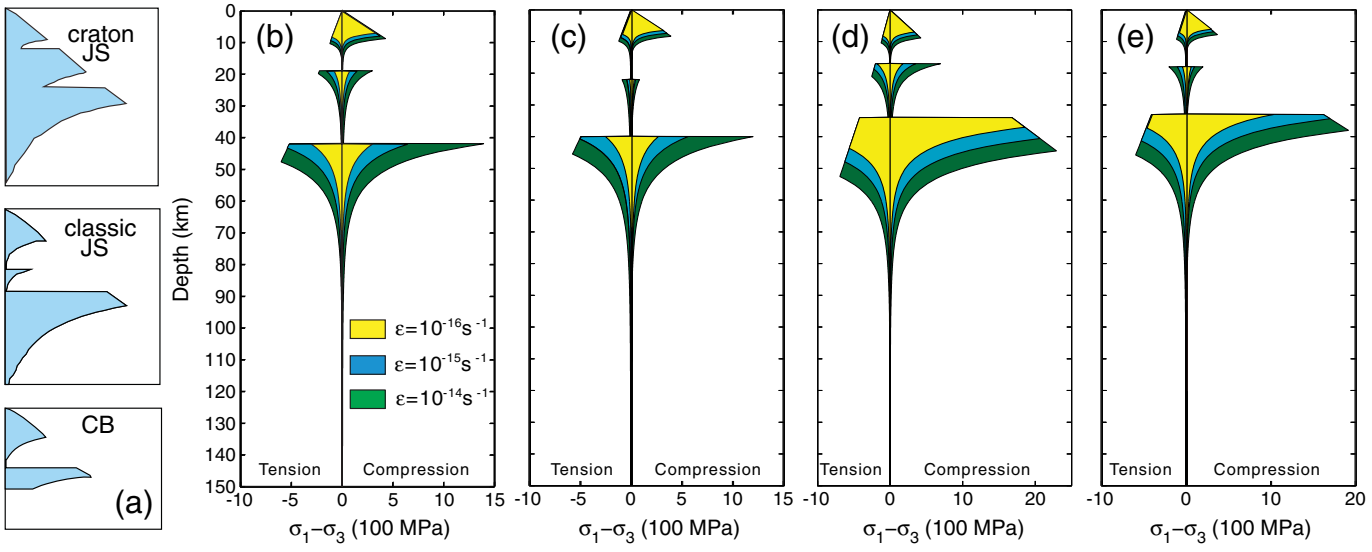

Fig. 21. Rheological yield stress envelopes (YSE) for (a) the craton JS (top of (a)), JS (center of (a)) and the CB (bottom of (a)) (Burov and Watts, 2006); (b) the western NCC; (c) the central NCC and (d) the Eastern Block in NCC; (e) the eastern b in NCC. The YSEs for the western NCC, the central NCC and the western NCC correspond to strain rates of 10–14, 10–15, and 10–16 s^{-1}, respectively.

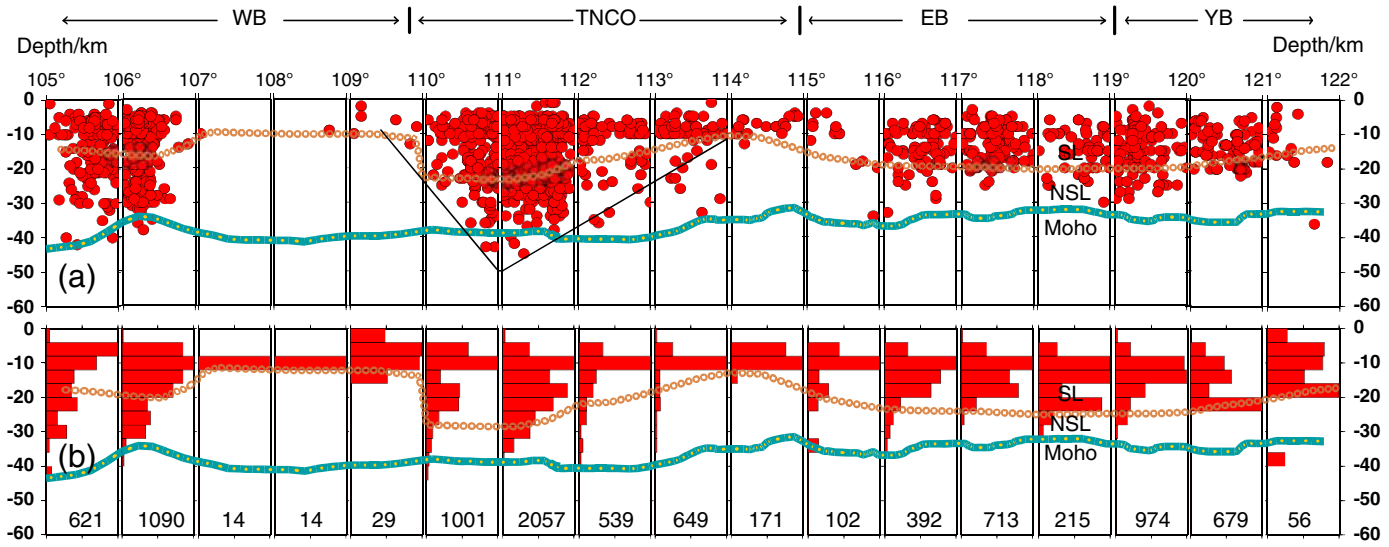

Fig. 22. (a) Distribution of earthquakes (red dots) along the transect Wen'an–Chayouzhongqi. SL indicates the seismogenic layer (within which 80% of the seismic energy is released) and NSL indicates the BDTL (Brittle/Ductile Transition Layer), the layer between the SL and the Moho discontinuity. The thin yellow line marks the depth separating SL and NSL in the crust. (b) Distribution of log E/Emax versus depth (see Brandmayr et al., 2010 for more details).

occur in the crust of the Ordos Basin in the western sub-block of the NCC. The difference in seismicity patterns (lithosphere rheology) among the WB, TNCO and EB, can be considered to be residual evidence of the crustal amalgamation of the NCC, or the lateral variation of crustal responses to lithospheric disruption. An alternative explanation is that this lateral variation may reflect a strong interaction between the eastward escaping flow and westward lithosphere flow (Fig. 23). The global relative westward lithosphere flow (WLF in Fig. 23) has been well studied (Panza et al., 2010), and can be confirmed from SKS splitting analyses (Chang et al., 2012). Eastward escaping flow (EEF in Fig. 23) is driven by the collision between the Indian and Eurasian plates (Tapponnier and Francheteau, 1978; Royden et al., 2008; Zhang et al., 2010b). The convergence between the eastern lithosphere and the western and the central NCC leads to double underthrusting at the eastern and the western margins of the NCC, respectively.

During the interaction between WLF and EEF, the eastern NCC lithosphere plays the role of the upper plate, whereas the western and the central NC act as the lower plate. The high velocity anomaly beneath the EB should result from break-off of the western and the central lithosphere. Our conclusion is against the westward subduction model, because in this model the high velocity anomaly is taken as a signature of lithospheric delamination of the EB or breakoff of the Pacific Plate. In fact, the live duration of the delaminated lithosphere is usually 30–40 Ma with differentiation processes in the mantle. Our model highlights the interaction between the EEF and the WLF, and can be considered to be the consequences for the lithosphere after its disruption.

The foregoing inference is supported by the differences in geochemistry of Cenozoic basalts between the east and the central domains of the NCC (Tang et al., 2006). Most of the ancient lithospheric mantle of the Eastern Block of the NCC has been lost, whereas considerable

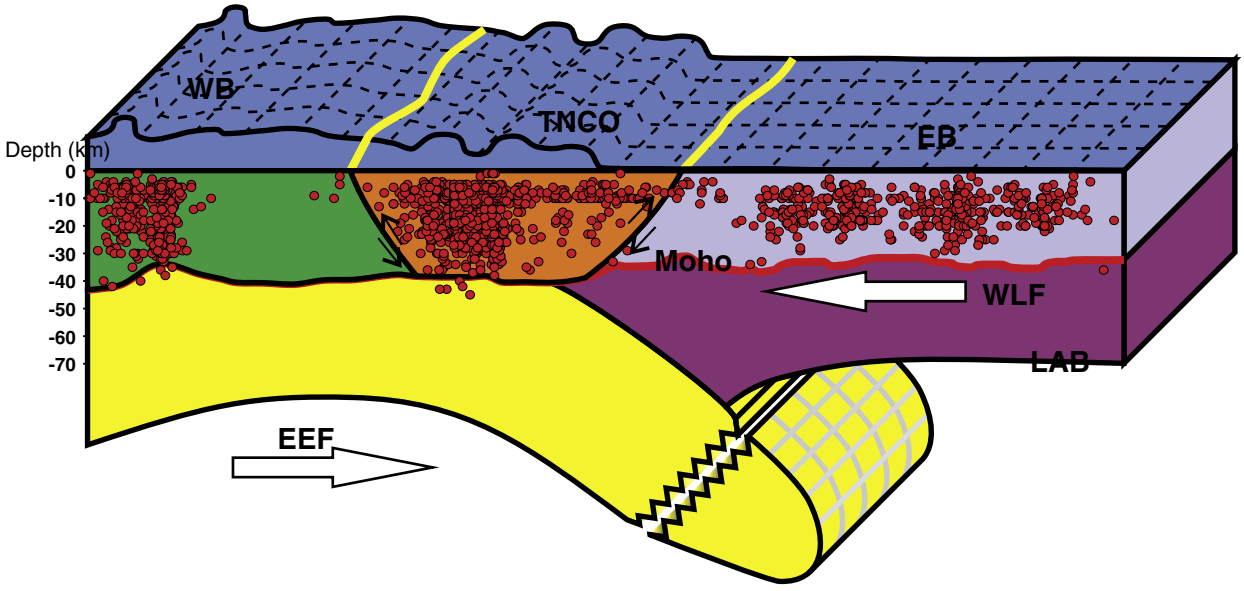

Fig. 23. Cartoon describing the interaction between the eastward escape flow (from the India–Asia collision) and westward lithosphere flow to explain the west–east variation in lithospheric strength across the NCC. Red dots indicate the distribution of earthquakes. LAB: Lithosphere Asthenosphere Bottom; EEF: Eastward escape flow; WLF: westward lithosphere flow. WB: Western Block; EB: Eastern Block; TNCO: Trans-North China Orogen. The white arrows indicate plate movement directions driven by mantle flow.

ancient lithosphere has been preserved in the TNCO (Gao et al., 2002; Rudnick et al., 2004). Additionally, the Cenozoic basalts from Datong and its adjacent regions demonstrate lithospheric thinning in the western NCC (Xu et al., 2004). The TNCO is a zone of transition in lithospheric thickness, and its lithospheric evolution reflects the interaction between the EEF and the WLF.

The mantle plume model (Peng et al., 2008; Peng, 2010) was proposed to explain the distribution of 1.78 Ga mafic dykes and the Xiongerr volcanic association, which is located at the southern margin of NCC, outside the area sampled by our surface wave tomography. Therefore, we cannot provide any constraints on the mantle plume model and its successive influence on the lithosphere disruption.

The north–south lateral variation in lithospheric properties (Zhang et al., 2012, 2013a) has been elucidated using a combination of (1) a compilation of crustal velocity models derived from dense wide-angle seismic profiling (Li and Mooney, 1998; Zhang et al., 2011e), (2) the lithospheric thickness as determined from teleseismic receiver function imaging (Chen, 2010) and surface wave tomography (Zhu et al., 1997), (3) the ρ structure of the crust and upper mantle from Bouguer anomalies inversion (Yuan et al., 1996a,b; Zhang et al., 2012; Deng et al., 2013), and (4) an indicator of lithosphere rheology: the distribution of hypocenters and of seismic energy released versus depth (Panza and Raykova, 2008; Zhang et al., 2011f; Wu and Zhang, 2012; Zhang et al., 2012, 2013a). Four major characteristics can be seen along the transect: (1) the crustal thickness is relatively constant, around 40 km; (2) the lithosphere thins considerably to about 80 km beneath the central segment, compared with about 140 km under the southern segment and the northern margin; (3) a classic Coulomb/Byerlee (brittle/ductile) transition law is valid beneath the southern and the northern segments of the transect, where the rheology and mechanical properties of rocks follow Sibson's (1977) Law in the upper crust and a power law creep in the lower crust; and (4) earthquake energy distribution in the whole crust beneath the central portion of the transect.

These characteristics are inconsistent with the general observation that the ruptures and earthquakes in many stable continental regions are confined within the upper third (0–10 km) and/or the lower third of the crust (20–35 km), while the middle crust (10–20 km) tends to be aseismic (Klose and Seeber, 2007) and is usually considered to be the brittle/ductile transition layer (BDTL) (Brown and Rushmer, 2006). Earthquakes are distributed within the middle crust, even within the whole crust beneath the central portion of the transect. The thick seismogenic layer beneath the NCP could be due to: (1) deeper fault penetration beneath the NCP than beneath the QDOB and the YSOB; (2) delamination of the lower part of the thickened crust, while the thick brittle layer is preserved; and (3) changes to brittleness of the BDTL, which cause a thickening of the seismogeneic layer: it is the underplating of the lower crust that provides the thermal resources necessary to increase its brittle strength by means of thermal softening (of the ductile component) beneath the NCP. Only the first and third processes can explain the lateral variation in the thickness of the seismogenic layer across the eastern part of the NCC, suggesting a significant role for extensional tectonics and thermal erosion, even though we cannot exclude the possibility that lithospheric delamination has been part of the disruption of the NCC.

According to both the P-wave velocity and density in the lowermost crust beneath the central section are significantly higher than in the corresponding parts of the south and north sections on the transect. These features are interpreted as geophysical signature of lower crustal underplating, which supplies sufficiently high gravitational potential energy to trigger lateral flow of the lower crust. This magma underplating-triggered bilateral lower crust flow may facilitate the lithospheric thinning by means of asthenosphere upwelling and decompression melting, which fills the gap produced by the lower crustal flow. The underplating-triggered lower crustal flow can provide an alternative mechanism to explain the NCC lithosphere disruption, which highlights the crustal feedback to Archaean lithosphere disruption, from top to bottom (Fig. 24).

6.6. Initial and boundary conditions between orogeny and craton

The supercontinent cycle maps out the large-scale history of the Earth, the formation and fragmentation of the continents, within an overall evolutionary enlargement of the total size of the continents with each cycle (Nance and Murphy, 2013; Nance et al., 2014). However, models that bridge the gap between detalied studies on individual orogens and their link with regional and global plate tectonic cycles require a better understanding of the difference between bottom-up and top-down processes. The growth and the destruction of continents at

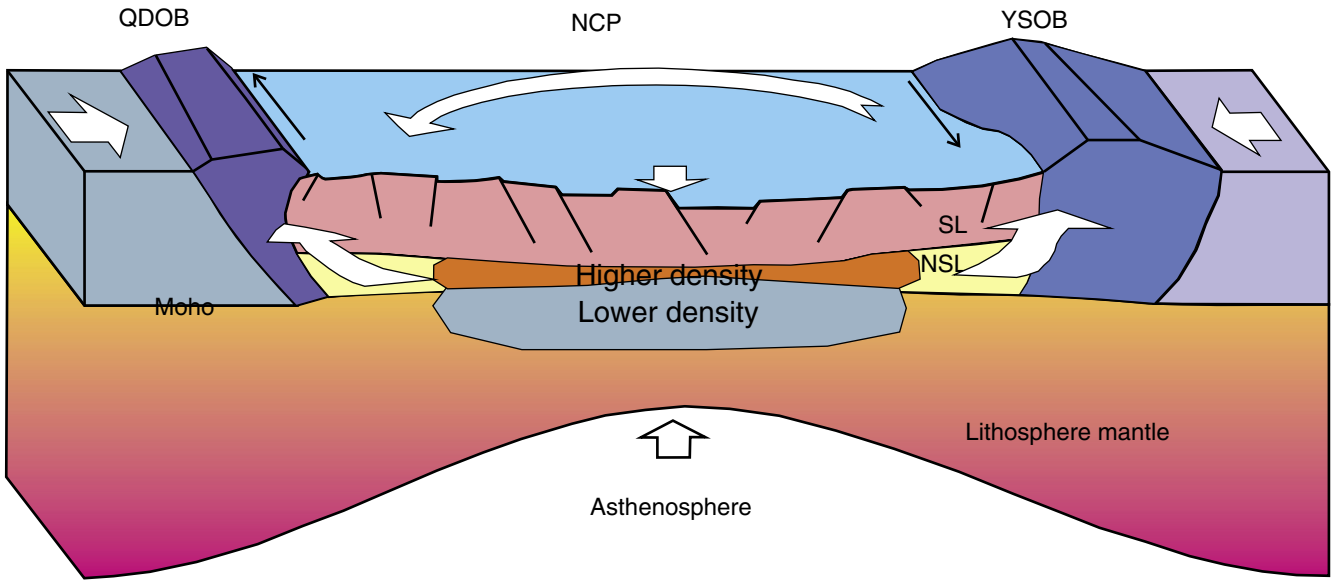

Fig. 24. Interpretation cartoon of the flow of ductile layer of the lower crust, triggered by lower crustal underplating. Sketch showing the internal book-shelf rotation of blocks as demonstrated by palaeomagnetism measurements (Zhu et al., 2002a,b), accommodates a broad east–west left-lateral shear bounded to the south by the sinistral slip Qinling Fault system (Zhang et al., 1995; Zheng et al., 2003) and dextral transtensional to transpressional strike-slip faulting to the north (Chen and Nabelek, 1988; Goscombe et al., 2005) accompanying the lower crust flows.

plate boundaries is yet another topic of interest to understand the net production and consumption of continental crust (Stern, 2011; Kawai et al., 2013). Obviously, the Tibetan Plateau and the North China Craton provide excellent places to understand the processes of orogeny, craton building and destruction.

6.6.1. From orogeny to craton to orogeny: the North China Craton

The NCC contains one of the longest, most complex records of magmatism, sedimentation and deformation on Earth, with deformation spanning the interval from the early Archean (3.8 Ga) to the present (Kusky et al., 2007). In the Wilson cycling between orogeny and craton, the NCC has recorded tectonic evolution from orogeny to craton to orogen (Kusky et al., 2007). It is well recognized that the central NCC records the collision between the western NCC and the eastern NCC at about 1.8 Ga (Zhao et al., 2001a, b, 2003, 2005; Kröner et al., 2006; Zhao et al., 2006a) and 2.5 Ma (Kröner et al., 1998; Zhai and Liu, 2003; Kusky and Li, 2010). These processes can be divided into: (1) 1.85 Ga: continent–continent collision at the northern margin of the craton; (2) 230 Ma: the Qingling–Dabieshan–Sulu Orogeny; (3) 200–100 Ma: Pacific Plate subduction; and (4) 130–120 Ma: from contraction to extension resulting in the original subcontinental mantle root loss beneath the NCC (Fan and Menzies, 1992).

The geophysical evidence on Pacific Plate subduction (200–100 Ma) has been derived from Vp, ρ, seismic activity, and temperature distribution along the Tangcheng–Lujiang fault belt in east China (Deng et al., 2013). Deng et al. (2013) indicated the segmentation along the Tangcheng–Lujiang (TL) fault as evidenced by several factors, such as earthquake occurrence, heat flow, average crustal Vp and ρ. These variations along the Tanlu fault and the high Vp anomaly beneath the eastern NCC defined by body wave tomography (Huang and Zhao, 2004; Tian et al., 2009) are attributed to the subduction of the Pacific Plate.

The Qingling–Dabieshan–Sulu Orogeny (230 Ma) has been extensively studied in the last 20 years by means of tectonics (G.W. Zhang et al., 2004; Zhai et al., 2007) and geochemical and geophysical data (Wang et al., 2000; Zhang et al., 2000). A compilation of crustal seismic velocity models, seismic activity and the yield stress envelope across west–east transects along the Qingling–Dabieshan–Sulu orogenic belt (Zhang et al., 2013a) demonstrates the lateral variation in the crustal structure caused by continental collision between the Yangtze and North China plates. Crustal velocity models across the north–south trending profiles (Wang et al., 2000; Zhang et al., 2000) have demonstrated that the Qingling–Dabieshan–Sulu Orogeny was a result of the continent–continent collision between the North and the South China plates. These geophysical data, together with other tectonic and geochemical evidence, support the idea that the NCC experienced a collision at about 230 Ma.

The occurrence of volcanic rocks (Fan et al., 2007; Zhai et al., 2007), the development of the North China Plain and the series of basins or depressions in the east NCC evidence the transition from a compressional to a tensional stress regime.

From previous studies (Zhang et al., 2012, 2013b), we have obtained the Gravitational Potential Energy (GPE = ρgz, where ρ has been obtained by Bouguer anomaly inversion and surface wave tomography, g is the gravitational acceleration, assumed to be equal to 9.81 m/s^2, and z stands for depth) along a north–south transect across the east NCC, and it is possible to observe that the high GPE beneath the center of the transect, namely in the lower crust beneath the North China Plain, can work as an engine to trigger lower crustal flow both southward and northward. This lower crustal flow can be another mechanism capable of destroying continental lithosphere, in addition to delamination, thermal erosion and marginal subduction (Zhu and Zheng, 2009).

6.6.2. From orogeny to craton: the Tibetan Plateau

Despite recent advances in our understanding of the Tibetan Plateau, many questions remain unresolved, such as: (1) how high can the plateau be uplifted? (2) has the Tibetan Plateau already reached its maximum elevation and entered into the stage of plateau collapse? And (3) what is the explanation for the distribution of north–south trending normal faults? During the evolution from orogeny to craton, the lithosphere should experience the tectonic process of thinning. Our regional map of Vs and of the lithospheric thickness beneath Tibet shows that lithospheric thickness is within the range 200–250 km. This is not compatible with the proposal of Houseman et al. (1981) that the shortening, which increased the crustal thickness beneath Tibet, should produce an unstable lithosphere, the lower part of which would detach and sink into the mantle. Tibet may eventually become a craton when the upper 30–40 km of its crust is removed by erosion (McKenzie and Priestley, 2008). The crustal thickness of most cratons is now about 40 km (Christensen and Mooney, 1995), and the metamorphic rocks at their surface record pressures of about 1 GPa (Harley, 1989, 2004). Presumably as result of shortening, the craton's crustal thickness must therefore have been 70–80 km at the time of metamorphism, if there was no later deformation. An important open question is whether the whole lithosphere was shortened, or whether only the crust was thickened, by thrusting or lower crust flow. Seismic studies (Tilmann et al., 2003) suggest that the crust and lithosphere of the Indian shield extend beneath the southern part of Tibet, and that the thick lithosphere in this region is inherited. This region therefore does not provide information about how thick lithosphere is produced beneath shields. However, Haines et al. (2003a,b) argued that in northern Tibet the crust has been shortened by pure shear. This process could thicken the lithosphere if the mantle was deformed in the same way.

If lithospheric removal did not occur beneath Tibet, the heat responsible for regional metamorphism cannot have been introduced from the base of the crust, and a different process must be responsible for the low sub-Moho velocities. The only other heat source available is crustal radioactivity, and it is clearly of interest to evaluate whether this could produce the observed effects. Numerical experiments show that crustal radioactivity can produce granulite grade regional metamorphism and lower the value of Vs in the mantle beneath the Moho. They also show how the processes that are active at present can account for the main characteristics of the craton. McKenzie and Priestley (2008) showed a sketch of two processes that can generate thick crust and lithosphere like that beneath Tibet: (1) shortening the entire lithosphere, or (2) increasing the crustal thickness of a region that already has a lithospheric thickness of 200 km or more. The final stage of crustal and lithospheric thickening occurs after shortening ceases, when erosion removes the upper crust and its radioactive elements, leaving the depleted mid-crust that underwent granulite facies metamorphism exposed at the surface. This process does not change the thickness of the mantle part of the lithosphere, and does not involve any tectonic deformation. If the upper half of the Tibetan crust is removed by erosion, the resulting velocity structure will be similar to that of cores with surfaces now exposed by erosion, many of which were formed in the Archean.

From the 3-D ρ structure beneath the Tibetan Plateau, we can construct a 3-D GPE map (Haines et al., 2003a,b; Zhang and Klemperer, 2005). In this study, we calculated the GPE difference at different longitudes and latitudes with reference to the average GPE for the Indian Plate. Fig. 25 shows the GPE difference distribution along the seven sections ((a) to (g)) shown in Fig. 9a. The distribution of Vs and ρ along the NE–SW sections (at least for some of them) clearly shows that in some instances the subducted lithosphere is less dense than the ambient rocks, and so cannot be supported by gravity; the subduction process requires the presence of a dynamical force that can be well supplied by the mantle flow that, very likely, is maximized along the TE-perturbed (Panza et al., 2010). In other words, the natural subduction of continental lithosphere cannot be driven by slab pull forces but requires significant drag, from mantle flow in the asthenosphere layer, to overcome the buoyancy of continental crust.

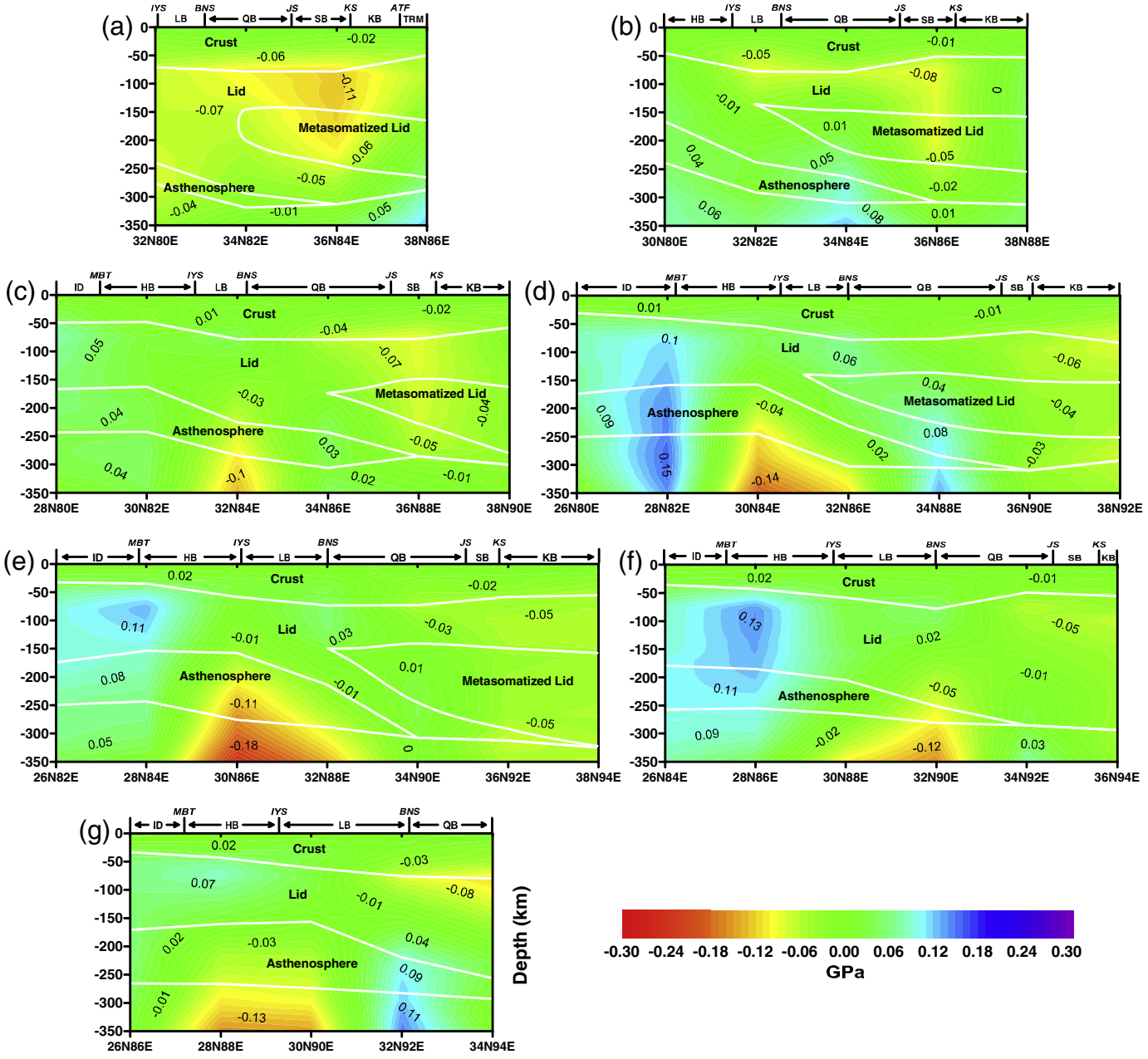

Fig. 25. GPE (Gravitational Potential Energy, unit GPa) deviation from the average GPE along profiles (a), (b), (c), (d), (e), (f) and (g) (see Fig. 9a for their location). ID: Indian Plate; IYS: Indus–Yarlung suture; BNS: Bangong–Nujiang suture; JS: Jinshajiang suture; KS: Anyimaqen–Kunlun–Mutztagh suture; QS: South Qilian suture; HB: Himalayan Block; LB: Lhasa Block; QB: Qiangtang Block; SB: Songpan–Ganzi Block; KB: Kunlun–Qaidam Block.

With the information about the mantle lid, the asthenosphere layer and the metasomatic lid in the Tibetan Plateau given in Figs. 9 and 13, we can construct the plane distribution of the asthenosphere layer and the metasomatic lid (Fig. 26). We observe that the asthenosphere layer is distributed mainly to the south of the BNS, while the metasomatic lid is distributed to the north of the BNS and overlaps with the zone of poor propagation of Sn waves (Ni and Barazangi, 1983). As the asthenosphere layer provides the drag force for the Indian Plate subduction, we can observe that the Indian lithosphere underthrusts as far as the BNS suture. North of the BNS the asthenosphere layer is quite thin, and may not provide sufficient drag force for the northward continuation of the subduction. It is widely accepted that there has been at least 1500 km of crustal shortening during the convergence and continental collision between the Indian and Eurasian plates over the past 50 million years. Crustal thickening and normal faulting cannot compensate this amount of crustal shortening. Tectonic escaping is another candidate mechanism to compensate for part of the shortening, which can also be established from recent GPS measurements (Gan et al., 2007). GPS measurements indicate that deformation is predominantly in a north–south direction in South Tibet, but changes to a nearly west–east direction in the north Tibet (Qiangtang and Songpan–Ganzi blocks. Studies of fault shear rates (Fu and Awata, 2007) also suggest that north Tibet is undergoing eastward tectonic escape. However, there is still a lack of agreement on whether the mechanism is tectonic escaping (Tapponnier and Francheteau, 1978) or lower crustal flow (Royden et al., 1997), and the dynamic source to trigger the escaping or flowing. The tectonic blocks showing this distribution of the asthenosphere layer and the metasomatic lid are south and north Tibet, with deformation in nearly north–south and west–east directions. This consistency leads us to speculate that the transition between the

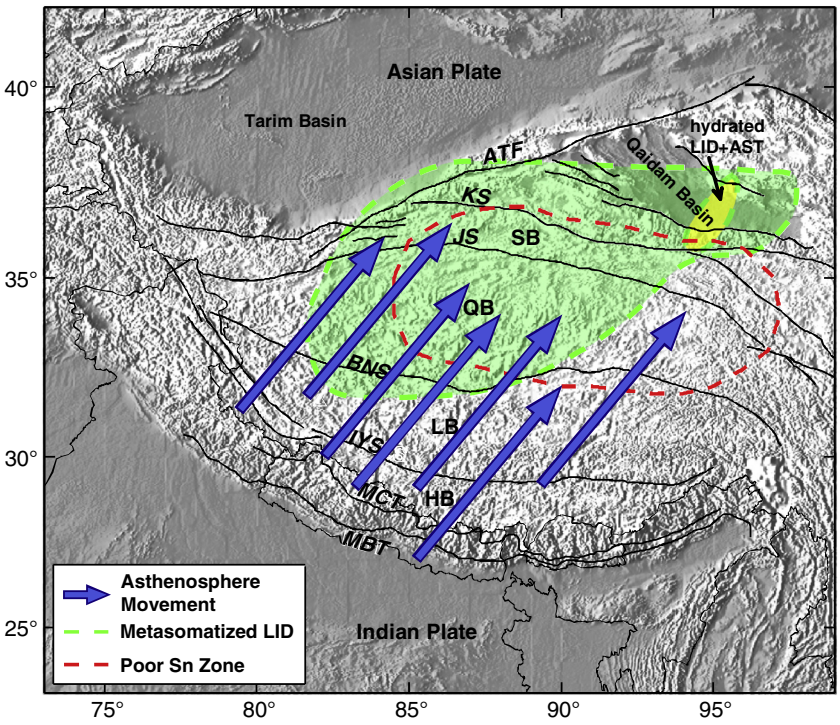

Fig. 26. The spatial distribution of the asthenosphere layer and of the metasomatic lid, corresponds with the transition area from convergence to eastward escape. The tips of the arrows indicate the position where the asthenosphere disappears, which can be considered to be the region dominated by north–south compression, due to the convergence and collision between the Indian and Eurasian plates. The region of poor Sn-wave propagation almost overlaps with the area where the metasomatic lid has been detected; this fact suggests that the region tends to escape eastward to accommodate the north–south shortening from the south of the BNS suture.

asthenosphere and metasomatic lid (Fig. 26) may also emphasize the tectonic system transition from convergence to eastward escape to accommodate the 1500 km long crustal shortening from the convergence of the Indian and Eurasian plates. The tips of the arrows in Fig. 26 indicate the position where the asthenosphere disappears, which can be considered to be the region dominated by north–south compression due to the convergence and collision between the Indian and Eurasian plates. The region of poor Sn-wave propagation almost overlaps with the area where the metasomatic lid has been detected; this fact suggests that the region tends to escape eastward to accommodate the north–south shortening from the south of the BNS suture. Metasomatism in the mantle wedge should be the dynamic source to trigger tectonic escape and provides a heat source to melt the underlying lithospheric mantle to strongly attenuate Sn propagation. Testing this hypothesis will require further investigations.

7. Concluding remarks

We present the structure of the crust and upper mantle as determined from absolute surface wave tomography and Bouguer anomaly inversion beneath the Tibetan Plateau and from ambient noise tomography beneath the NCC. Our main conclusions are as follows.

(1) The structure of crust and upper mantle beneath Tibet and the interaction between Indian and Eurasia plates are strongly strike-dependent (along Himalaya orogenic margin). The strike dependence can be represented by (1) strong west–east lateral variation in Vs in the crust and upper mantle beneath the Tibetan Plateau; (2) west–east variation of the subduction angle of the Indian Plate beneath Lhasa (about 15° beneath the west of the Tibetan Plateau and about <10° beneath the eastern part); and (3) distinctive lateral variation in the thickness of the metasomatic lid from west to the east of the Tibetan Plateau. These results may suggest (1) the diachronous convergence and collision between Indian and Eurasian plates should be taken into account in the interpretation of the wide range of collision aging from 35 Ma to 70 Ma (Mo et al., 2007) and also the difference of topography gradient distribnution along the margin of Himalaya (Yin, 2006); and (2) 3D imaging and the understanding with the base of this imaging should be enhanced, even though it can be generalized with reference to the lithosphere structure along the specific 2D transect and the geodynamic understanding derived from this 2D transect.

(2) Our results cannot provide robust evidence for the presence of eclogites in the lower crust from Vs and ρ beneath the Lhasa Block and Himalaya. However, our results do not exclude the possibility of the delamination of the ecologized lower crust and that the bouyancy from the lower crustal delamination uplifts the Himalaya. The low Vp/Vs ratio and very high Vp and Vs in the lower crust beneath Lhasa terrane (Zhang and Klemperer, 2005, 2010; Mechie and Kind, 2013) suggest that felsic granulite should be the predominant composition of the lower crust, and that metamorphosed mafic granulite contributes to the rise of the plateau. The lower crust with composition of felsic granulite should be weak in rheology strength (Zhang et al., 2013b) and can be deformed or even flow as suggested by polarization anisotropy (Shapiro et al., 2004; Y. Chen et al., 2009), maintaining the topography of the interior of the plateau relatively flat, as observed today (Yin, 2006);

(3) The distribution of Vs and ρ along the NE–SW sections clearly shows that in some instances the subducted lithosphere is less dense than the ambient rocks, thus subduction cannot be due to gravity. The subduction process requires the presence of a dynamic force that can be well supplied by the mantle flow that, very likely, is maximum along the TE-perturbed especially in the LVZ, between 120 and 200 km of depth, that is likely to represent the decoupling between the lithosphere and the underlying mantle at global scale (Panza et al., 2010). Slabs not denser than the

ambient mantle evidence conflicts with the concept of slab pull and thus call for different factors in subduction dynamics (e.g. Doglioni et al., 2007; Ji et al., 2007). This conclusion based on the geophysical imaging results in Tibet is documented in the Alps- or Apennines-type collision/subduction (Brandmayr et al., 2011; Foulger et al., 2013) as well, where the subducting slab is not denser than the ambient mantle, but slightly lighter. The flow is very shallow in the active Tyrrhenian basin due to mantle compensation induced by the eastward migration of the Apennines subduction. High densities (>3.3 g/cm^3) in the mantle seem to be strictly related to the eastward flow itself and to its ascent beneath the back-arc basin.

(4) Different crustal Vs structure between the western, the central and the eastern NCC have been detected using ambient noise tomography. The lateral variation of the crustal structure in seismic P-wave and S-wave velocities, seismic activity, density and temperature suggests the interaction between the Tibetan eastward escape flow and the Pacific westward lithosphere flow. For the west and the central NCC, this strong interaction of westward and eastward motion leads to west–east compression tectonic environment at lithosphere scale and extensional setting at the upper crustal scale in the central NCC. The joint presence of compression state at depth and shallow tensional setting leads the uplift of the TNCO and also the formation of Sanxi depression. For the eastern NCC, there is lower crust underplating beneath the North China Plain revealed by high velocity, dense lower crust, which produces underplating-triggered flow of the lower-crust in the NCC.

(5) The transition of the tectonic system, from north–south shortening beneath the south of the BNS to eastward escape at the north of the BNS, suggests that the mantle flow plays important role in this key continental geodynamical process in the transition from orogeny to craton. The spatial–temporal variation of lithospheric rheology structure (pattern) may be essential in the link between orogeny and craton in the Wilson cycle. This importance can be supported by the west–east variation of the crustal geophysical structure, lithospheric strength, both seismic rheology and yield stress envelope (Zhang et al., 2012, 2013b,c), especially with consideration of fluid inclusion in the mantle wedge (Frezzotti et al., 2009; Zheng et al., 2011). Our conclusion derived from studies in Tibetan Plateau and NCC, echoes and extends the recent results of no-hint for slab pull in the lithosphere in Italy (Brandmayr et al., 2011). This inference requires the contribution of mantle flow as a dynamic source for the subduction of continental lithosphere with low density structure.

Acknowledgments

This paper is one of the main results from the Double Italian–Chinese Doctorate in “Geophysics of the Lithosphere and Geodynamics, XXI Doctorate Cycle” issued by: University of Trieste, Graduate School, Chinese Academy of Sciences (CAS), China Earthquake Administration (CEA), Institute of Geophysics, Beijing, China in the framework of the Internationalization Program (D.M. 5 August 2004, n. 262, Art. 23) — International University Cooperations Program 2004–2006, Prot. II04A1CHC8, MIUR (Italian Ministry for Teaching, University and Research) PROJECT: Advanced methodologies in the field of geophysics and geodynamics. The supervision of the three PhD students (Lihua Fan from IG, CEA; Xuemei Zhang and Sufang Zhang from IGG, CAS) has been carried out by Professor G. Panza, Prof. Carla Braitenberg and Prof. Fabio Romanelli, from Trieste University (DMG), Professors Ding Zhifeng and Wujiang Ping from the Institute of Geophysics, China Earthquake Administration (IG, CEA), and Professors Jiwen Teng and Zhongjie Zhang from the Institute of Geology and Geophysics, Chinese Academy of Sciences (IGG, CAS). Special thanks to Prof. S.S. Rai of NGRI who made available several records from Indian seismological stations. We would like to thank Zhu R., Fan W. and Zhang H., for some fruitful discussions. We are especially grateful to M. Santosh for his constructive comments. The Strategic Priority Research Program (B) of the Chinese Academy of Sciences (Grant XDB03010700), National Basic Research Program of China (973 Program, grant 2011CB808904), and the National Natural Science Foundation of China (41021063) supported this research. Thanks are also due to Italian PRIN projects 2008, 2010, PNRA projects 2004/2.7–2.8, 2009/A2.17.

Appendix A. Supplementary data

Supplementary data to this article can be found online at http://dx.doi.org/10.1016/j.earscirev.2013.12.005.

References

Aitchison, J.C., Davis, A.M., 2001. Orogenic conglomerates indicate timing of collision in Tibet, 16th Himalaya–Karakorum–Tibet workshop. J. Asian Earth Sci. 19/3A, 1–2.
Aitchison, J.C., Davis, A.M., Abrajevitch, A.V., Ali, J.R., Badengzhu Liu, J.B., Luo, H., McDermid, I.R.C., Ziabrev, S.V., 2003. Stratigraphic and sedimentological constraints on the age and tectonic evolution of the Neotethyan ophiolites along the Yarlung Tsangpo suture zone, Tibet. Geol. Soc. Spec. Publ. 218, 147–164 (in Ophiolites in Earth history).
Aitchison, J.C., Ali, J.R., Davis, A.M., 2007. When and where did India and Asia collide? J. Geophys. Res. 112, B05423. http://dx.doi.org/10.1029/2006JB004706.
Aitchison, J.C., Xia, X., Baxter, A.T., Ali, J.R., 2011. Detrital zircon U–Pb ages along the Yarlung–Tsangpo suture zone, Tibet: implications for oblique convergence and collision between India and Asia. Gondwana Res. 20 (4), 691–709.
Allègre, C.J., Courtillot, V., Tapponnier, P., et al., 1984. Structure and evolution of the Himalaya–Tibet orogenic belt. Nature 307, 17–22.
Argand, E., 1924. La tectonique de l' Asie. Proc. 13th Int. Geol. Congr, 7, pp. 171–372.
Armijo, R., Tapponnier, P., Mercier, J.L., Han, T.L., 1986. Quaternary extension in southern Tibet: field observations and tectonic implications. J. Geophys. Res. 91, 13803–13872.
Armijo, R., Tapponnier, P., Han, T.L., 1989. Late Cenozoic right-lateral strike-slip faulting in Southern Tibet. J. Geophys. Res. 94, 2787–2838. http://dx.doi.org/10.1029/JB094iB03p02787.
Arnaud, N.O., Vidal, P., Tapponnier, P., Matte, P., Deng, W.M., 1992. The high K_2O volcanism of northwestern Tibet: geochemistry and tectonic implications. Earth Planet. Sci. Lett. 111, 351–367.
Arndt, N.T., 1983. Role of a thin, komatiite-rich oceanic crust in the Archean plate-tectonic process. Geology 11 (7), 372–375.
Avouac, J.P., Tapponnier, P., 1993. Kinematic model of active deformation in Central Asia. Geophys. Res. Lett. 20 (10), 895–898.
Bai, Z.M., Zhang, Z.J., Wang, Y.H., 2007. Crustal structure across the Dabie–Sulu orogenic belt revealed by seismic velocity profiles. J. Geophys. Eng. 4 (4), 436–442.
Bai, D., Unsworth, M.J., Meju, M.A., et al., 2010. Crustal deformation of the eastern Tibetan plateau revealed by magnetotelluric imaging. Nat. Geosci. 3, 358–362. http://dx.doi.org/10.1038/ngeo830.
Bai, Z., Tian, X., Tian, Y., 2011. Upper mantle P-wave tomography across the Longmenshan fault belt from passive-source seismic observations along Aba–Longquanshan profile. J. Asian Earth Sci. 40, 873–882.
Beaumont, C., Jamieson, R.A., Nguyen, M.H., Lee, B., 2001. Midcrustal channel flow in large hot orogens: results from coupled thermal–mechanical models. In: Cook, F., Erdmer, P. (Eds.), Slave — Northern Cordillera Lithospheric Evolution (SNORCLE) and Cordilleran Tectonics Workshop; Report of 2001 Combined Meeting, Lithoprobe Rep. 79. Lithoprobe Scretariat, Univ. of B. C, Vancouver, pp. 112–170.
Beaumont, C., Jamieson, R.A., Nguyen, M.H., Medvedev, S., 2004. Crustal channel flows: 1. Numerical models with applications to the tectonics of the Himalayan–Tibetan orogen. J. Geophys. Res. 109, B06406.
Bensen, G.D., Ritzwoller, M.H., Barmin, M.P., Levshin, A.L., Lin, F., Moschetti, M.P., Shapiro, N.M., Yang, Y., 2007. Processing seismic ambient noise data to obtain reliable broad-band surface wave dispersion measurements. Geophys. J. Int. 169, 1239–1260.
Bilham, R., Larson, K., Freymueller, J., 1997. GPS measurements of present-day convergence across the Nepal Himalaya. Nature 386, 61–64.
Bird, P., 1991. Lateral extrusion of lower crust from under high topography in the isostatic limit. J. Geophys. Res. 96, 10275–10286.
Blisniuk, P.M., Hacker, B.R., Glodny, J., Ratschbacher, L., Bi, S., Wu, Z., McWilliams, M.O., Calvert, A., 2001. Normal faulting in central Tibet since at least 13.5 Myr ago. Nature 412, 628–632.
Bostrom, R.C., 1971. Westward displacement of the lithosphere. Nature 234, 536–538. http://dx.doi.org/10.1038/234536a0.
Bousquet, R., Goffé, B., Henry, P., Le Pichon, X., Chopin, C., 1997. Kinematic, thermal and petrological model of the Central Alps: Lepontine metamorphism in the upper crust and eclogitisation of the lower crust. Tectonophysics 273 (1–2), 105–127.
Boyadzhiev, G., Brandmayr, E., Pinat, T., Panza, G.F., 2008. Optimization for non-linear inverse problems. Rendiconti Lincei. 19, 17–43. http://dx.doi.org/10.1007/s12210-008-0002-z.
Braitenberg, C., Zadro, M., Fang, J., Wang, Y., Hsu, H.T., 2000. The gravity and isostatic Moho undulations in Qinghai–Tibet plateau. J. Geodyn. 30 (5), 489–505.
Braitenberg, C., Wang, Y., Fang, J., Hsu, H.T., 2003. Spatial variations of flexure parameters over the Tibet–Quinghai plateau. Earth Planet. Sci. Lett. 205, 211–224.
Brandmayr, E., Raykova, R., Zuri, M., Romanelli, F., Doglioni, C., Panza, G.F., 2010. The lithosphere in Italy: structure and seismicity, In: Beltrando, M., Mattei, A.M., Conticelli, S., Doglioni, C. (Eds.), The Geology of Italy, Electronic edition. Journal of the Virtual Explorer1441-8142, vol. 36 (paper 1).

Brandmayr, Marson I., Romanelli, F., Panza, G.F., 2011. Lithosphere density model in Italy: no hint for slab pull running head: lithosphere density model in Italy: no hint for slab pull. Terra Nova 23, 292–299.
Brandon, C., Romanowicz, B., 1986. A "no-lid" zone in the central Chang–Thang platform of Tibet: evidence from pure path phase velocity measurements of long period Rayleigh waves. J. Geophys. Res. 91, B6. http://dx.doi.org/10.1029/JB091iB06p06547.
Breunig, M., Cremers, A.B., Götze, H.J., Schmidt, S., Seidemann, R., Shumilov, S., Siehl, A., 2000. Geological mapping based on 3D models using an interoperable GIS. J. Spat. Inf. Decis. Making 13, 12–18.
Brewer, I.D., Burbank, D.W., Hodges, K.V., 2003. Modelling detrital cooling-age populations: insights from two Himalayan catchments. Basin Res. 15, 305–320.
Brias, A., Patriat, A., Tapponier, P., 1993. Updated interpretation of magnetic anomalies and seafloor spreading stages in the South China Sea: implication for the Tertiary tectonics of Southeast Asia. J. Geophys. Res. 98, 6299–6328.
Brown, M., Rushmer, T., 2006. Evolution and Differentiation of the Continental Crust.Cambridge University Press.
Brown, D., Carbonell, R., Kukkonen, I., Ayala, C., Golovanova, I., 2003. Composition of the Uralide crust from seismic velocity (Vp, Vs), heat flow, gravity, and magnetic data. Earth Planet. Sci. Lett. 210 (1–2), 333–349.
Burchfiel, B.C., Royden, L.H., 1991. Tectonics of Asia 50 years after the death of Emile Argand. Eclogae Geol. Helv. 84, 599–629.
Burchfiel, B.C., Chen, Z., Hodges, K.V., Liu, Y., Royden, L.H., Deng, C., Xu, J., 1992. The South Tibetan detachment system, Himalayan orogen: extension contemporaneous with and parallel to shortening in a collisional mountain belt. Spec. Pap. Geol. Soc. Am. 269 (48 pp.).
Burg, J.P., Chen, G.M., 1984. Tectonics and structural zonation of southern Tibet, China. Nature 311, 219–223.
Burov, E.B., Watts, A.B., 2006. The long-term strength of continental lithosphere: "jelly sandwich" or "crème brulee"? GSA Today 12, 4–10.
Burov, E.V., Kogan, M.G., Lyon-Caen, H., Molnar, P., 1990. Gravity anomalies, the deep structure, and dynamic processes beneath the Tien Shan. Earth Planet. Sci. Lett. 96 (3–4), 367–383.
Campillo, M., Paul, A., 2003. Long-range correlations in the diffuse seismic coda. Science 299, 547–549.
Cattin, R., Martelet, G., Henry, P., Avouac, J.P., Diament, M., Shakya, T.R., 2001. Gravity anomalies, crustal structure and thermomechanical support of the Himalaya of central Nepal. Geophys. J. Int. 147, 381–392.
Chang, C.F., Zheng, S.L., 1973. Tectonic features of the Mount Jolmo Lungma region in southern Tibet, China. Sci. Geol. Sin. 1, 1–12.
Chang, C., Shackleton, R.M., Dewey, J.F., Yin, J., 1988. The Geological Evolution of Tibet: Royal Society—Academia Sinica Geotraverse of the Qinghai–Xizang Plateau 1985.Royal Society, London.
Chang, L., Wang, C.-Y., Ding, Z., 2012. Upper mantle anisotropy beneath North China from shear wave splitting measurements. Tectonophysics 522, 235–242.
Chen, L., 2010. Concordant structural variations from the surface to the base of the upper mantle in the North China Craton and its tectonic implications. Lithos 120, 96–125.
Chen, W.P., Nabelek, J., 1988. Seismological strike-slip faulting and the development of north China basin. Tectonics 7, 975–989.
Chen, Q., Freymueller, J., Wang, Q., Yang, Z., Xu, C., Liu, J., 2004a. A deforming block model for the present day tectonics of Tibet. J. Geophys. Res. 109. http://dx.doi.org/10.1029/2002JB002151.
Chen, Y.J., Pirajno, F., Sui, Y.H., 2004b. Isotope geochemistry of the Tieluping silver deposit, Henan, China: a case study of orogenic silver deposits and related tectonic setting. Miner. Deposita 39, 560–575.
Chen, L., Tao, W., Zhao, L., 2008. Distinct lateral variation of lithospheric thickness in the Northeastern North China Craton. Earth Planet. Sci. Lett. 267, 56–68.
Chen, L., Cheng, C., Wei, Z., 2009a. Seismic evidence for significant lateral variations in lithospheric thickness beneath the central and western North China Craton. Earth Planet. Sci. Lett. 286, 171–183.
Chen, Y., Badal, J., Zhang, Z.J., 2009b. Radial anisotropy in the crust and upper mantlebeneath the Qinghai–Tibet Plateau and surrounding regions. J. Asian Earth Sci. 36 (4–5), 289–302.
Chen, Y., Badal, J., Hu, J., 2010. Love and Rayleigh wave tomography of the Qinghai–Tibet Plateau and surrounding areas. Pure Appl. Geophys. 167 (10), 1171–1203.
Chen, Y., Zhang, Z., Sun, C., Badal, J., 2013. Crustal anisotropy from Moho converted Ps wave splitting analysis and geodynamic implications beneath the eastern margin of Tibet and surrounding regions. Gondwana Res. 24 (3–4), 946–957. http://dx.doi.org/10.1016/j.gr.2012.04.003.
Christensen, N.I., Mooney, W.D., 1995. Seismic velocity structure and composition of the continental crust: a global view. J. Geophys. Res. 100, 9761–9788.
Chung, S.L., Jahn, B.M., Wu, G.Y., Lo, C.H., Cong, B.L., 1998. The Emeishan flood basalt in SW China: a mantle plume initiation model and its connection with continental break-up and mass extinction at the Permian–Triassic boundary. In: Flower, M.F.J., Chung, S.L., Lo, C.H., Lee, T.Y. (Eds.), Mantle Dynamics and Plate Interaction in East Asia. AGU Geodynamic Series, 27, pp. 47–58.
Chung, S.L., Chu, M.F., Zhang, Y., Xie, Y., Lo, C.H., Lee, T.Y., Lan, C.Y., Li, X., Zhang, Q., Wang, Y., 2005. Tibetan tectonic evolution inferred from spatial and temporal variations in post-collisional magmatism. Earth Sci. Rev. 68, 173–196.
Clark, M.K., Royden, L.H., 2000. Topographic ooze: building the easternm argin of Tibet by lower crustal flow. Geology 28 (8), 703–706.
Coleman, M.E., Hodges, K.V., 1995. Evidence for Tibetan Plateau uplift before 14 Myr ago from a new minimum estimate for east–west extension. Nature 374, 49–52.
Condie, K.C., 2000. Episodic continental growth models: afterthoughts and extensions. Tectonophysics 322 (1–2), 153–162.
Condie, K.C., 2001. Mantle Plumes and Their Record in Earth History.Cambridge University Press, Cambridge, UK (306 pp.).
Condie, K.C., 2004. Supercontinents and superplume events: distinguishing signals in the geologic record. Phys. Earth Planet. Inter. 146, 319–332.
Condie, K.C., Aster, R.C., 2013. Refinement of the supercontinent cycle with Hf, Nd and Sr isotopes. Geosci. Front. 4, 667–680.
Condie, K.C., Des Marais, D.J., Abbot, D., 2001. Precambrian superplumes and supercontinents: a record in black shales, carbon isotopes and paleoclimates? Precambrian Res. 106, 239–260.
Cotte, N., Pedersen, H., Campill, M., Mars, J., Ni, J.F., Kind, R., Sandvol, E., Zhao, W., 1999. Determination of the crustal structure in southern Tibet by dispersion and amplitude analysis of Rayleigh waves. Geophys. J. Int. 138, 809–819. http://dx.doi.org/10.1046/j.1365-246x.1999.00927.x.
Crespi, M., Cuffaro, M., Doglioni, C., Giannone, F., Riguzzi, F., 2007. Space geodesy validation of the global lithospheric flow. Geophys. J. Int. 168, 491–506.
Cuffaro, M., Jurdy, D.M., 2006. Microplate motions in the hotspot reference frame. Terra Nova 18, 276–281.
Davis, A.S., Clague, D.A., 2006. Deep submarine explosive basaltic eruptions at vents in the North Arch Volcanic Field. Bull. Volcanol. 68, 294–307.
Davis, G.A., Qian, X.L., Zheng, Y.D., Yu, H., Wang, C., Tong, H.M., Gehrels, G.E., Shafiquallah, M., Fryxell, J.E., 1996. Mesozoic deformation and plutonism in the Yunmeng Shan: a Chinese metamorphic core complex north of Beijing, China. In: Yin, A., Harrison, T.M. (Eds.), The Tectonic Evolution of Asia. Cambridge University Press, Cambridge, pp. 253–280.
Davis, A.M., Aitchison, J.C., Badengzhu, Luo H., Zyabrev, S., 2002. Paleogene island arc collision-related conglomerates, Yarlung–Tsangpo suture zone, Tibet. Sediment. Geol. 150, 247–273.
Deng, W., 1989. Cenozoic volcanic rocks in the northern Ngari district of the Tibet—discussion on the concurrent subduction. Acta Petrol. Sin. 3, 1–11 (in Chinese with English abstract).
Deng, W., 1998. Cenozoic Intraplate Volcanic Rocks in the Northern Qinghai–Xizang Plateau.Geologic Publishing House, Beijing (180 pp., in Chinese with English abstract).
Deng, J.F., Mo, X.X., Zhao, H.L., Wu, Z.X., Luo, Z.H., Su, S.G., 2004. A new model for the dynamic evolution of Chinese lithosphere: 'continental roots-plume tectonics'. Earth Sci. Rev. 65, 223–275.
Deng, J., Su, S., Liu, C., Zhao, G., Zhao, X., Zhou, S., Wu, Z., 2006. Discussion on the lithospheric thinning of the North China craton: delamination? Or thermal erosion and chemical metasomatism. Earth Sci. Front. 13, 105–119 (in Chinese with English abstract).
Deng, Y., Fan, W., Zhang, Z., Badal, J., 2013. Geophysical evidence on segmentation of the Tancheng–Lujiang fault and its implications on the lithosphere evolution in East China. J. Asian Earth Sci. 78, 263–276. http://dx.doi.org/10.1016/j.jseaes.2012. 11.006.
Dewey, J.F., 1988. Extensional collapse of orogens. Tectonics 7, 1123–1139.
Dewey, J.F., Burke, K., 1973. Tibetan, Variscan and Precambrian basement reactivation: products of continental collision. J. Geol. 81, 683–692.
Dewey, J.F., Shackleton, R.M., Chang, C.F., Sun, Y.Y., 1988. The tectonic evolution of the Tibetan plateau. Phil. Trans. R. Soc. London A 327, 379–413.
Dewey, J.F., Cande, S., Pitman, W.C., 1989. Tectonic evolution of the Indian–Eurasia collision zone. Eclogae Geol. Helv. 82, 717–734.
Ding, Z.F., Zeng, R.S., 1994. The 3D velocity structure inversion in Beijing–Tianjin–Tangshan area by using local earthquake data. North China Earthq. Sci. 12 (2), 14–20.
Ding, Z., He, Z., Wu, J., Sun, W., 2001. Research on the 3-D seismic velocity structures in Qinghai–Xizang Plateau. Earthq. Res. China 17, 202–209.
Ditmar, P.G., Yanovskaya, T.B., 1987. Generalization of Backus–Gilbert method for estimation of lateral variations of surface wave velocities. Phys. Solid Earth Izvestia Acad. Sci. U.S.S.R. 23 (6), 470–477.
Dobretsov, N.L., Berzin, N.A., Buslov, M.M., 1995. Opening and the tectonic evolution of Paleo-Asian ocean. Int. Geol. Rev. 35, 335–360.
Doglioni, C., 1990. The global tectonic pattern. J. Geodyn. 12 (1), 21–38.
Doglioni, C., 1991. A proposal of kinematic modelling for W dipping subductions — possible applications to the Tyrrhenian–Apennines system. Terra Nova 3, 423–434. http://dx.doi.org/10.1111/j.1365-3121.1991.tb00172.x.
Doglioni, C., 1993. Some remarks on the origin of foredeeps. Tectonophysics 228 (1–2), 1–20.
Doglioni, C., Gueguen, E., Sàbat, F., Fernandez, M., 1997. The Western Mediterranean extensional basins and the Alpine orogen. Terra Nova 9, 109–112. http://dx.doi.org/10.1046/j.1365-3121.1997.d01-18.x.
Doglioni, C., Gueguen, E., Harabaglia, P., Mongelli, F., 1999a. On the origin of west-directed subduction zones and application to the western Mediterranean. In: Durand, Jolivet, Horváth, Séranne (Eds.), The Mediterranean Basins: Tertiary Extension Within the Alpine Orogen. Geol. Soc. London Spec. Publ., 156, pp. 541–561.
Doglioni, C., Harabaglia, P., Merlini, S., Mongelli, F., Peccerillo, A., Piromallo, C., 1999b. Orogens and slabs vs their direction of subduction. Earth Sci. Rev. 45, 167–208.
Doglioni, C., Carminatia, E., Cuffaroa, M., 2006. Simple kinematics of subduction zones. Int. Geol. Rev. 48 (6). http://dx.doi.org/10.2747/0020-6814.48.6.479.
Doglioni, C., Carminati, E., Cuffaro, M., Scrocca, D., 2007. Subduction kinematics and dynamic constraints. Earth Sci. Rev. 83, 125–175.
Doglioni, C., Tonarini, S., Innocenti, F., 2009. Mantle wedge asymmetries and geochemical signatures along W- and E–NE-directed subduction zones. Lithos 113 (1), 179–189.
Dziewonski, A.M., Anderson, D.L., 1981. Preliminary reference Earth model. Phys. Earth Planet. Inter. 25 (4), 297–356.
Ebbing, J., Braitenberg, C., Götze, H.J., 2001. Forward and inverse modelling of gravity revealing insight into crustal structures of the Eastern Alps. Tectonophysics 337, 191–208.

England, P., Houseman, G., 1985. Role of lithospheric strength heterogeneities in the tectonics of Tibet and neighbouring regions. Nature 315, 297–301.
England, P., Houseman, G., 1988. The mechanics of the Tibetan plateau. Phil. Trans. R. Soc. London A327, 379–413.
England, P., Molnar, P., 1998. The field of crustal velocity in Asia calculated from Quaternary rates of slip on faults. Geophys. J. Int. 130, 551–582.
Eriksson, P.G., Catuneanu, O.A., 2004. commentary on Precambrian plate tectonics. In: Eriksson, P.G., Altermann, W., Nelson, D.R., Mueller, W.U., Catuneanu, O. (Eds.), The Precambrian Earth Tempos and Events, Development in Precambrian Geology, 12. Elsevier, Amsterdam (201–212 pp.).
Fan, W.M., Menzies, M.A., 1992. Destruction of aged lower lithosphere and accretion of asthenosphere mantle beneath eastern China. Geotecton. Metallog. 16, 171–180.
Fan, W.M., Zhang, H.F., Baker, J., Davis, K.E., Mason, P.R.D., Menzies, M.A., 2000. On and off the North China craton: where is the Archean keel? J. Petrol. 41, 933–950.
Fan, W.M., Guo, F., Wang, Y.J., Zhang, M., 2004. Late Mesozoic volcanism in the northern Huaiyang tectono-magmatic belt, central China: partial melts from a lithospheric mantle with subducted continental crust relicts beneath the Dabie Orogen? Chem. Geol. 209 (1–2), 27–48.
Fan, W.M., Guo, F., Wang, Y.J., Zhang, H.F., 2007. Late Mesozoic mafic magmatism from the North China Block: constrains on chemical and isotopic heterogeneity of the subcontinental lithospheric mantle. In: Zhai, M.G., Windley, B.F., Kusky, T.M., Meng, Q.R. (Eds.), Mesozoic Sub-continental Lithospheric Thinning Under Eastern Asia. Geol. Soc. London, Spec. Publ., 280, pp. 77–100.
Fang, J., 1999. Global crustal and lithospheric thickness inversed by using satellite gravity data. Crustal Deformation Earthq. 19 (1), 26–31 (in Chinese with English abstract).
Fang, L.H., 2010. Rayleigh Wave Tomography in North-China from Ambient Seismic Noise. (PhD dissertation) University of Trieste.
Fang, L.H., Wu, J.P., Ln, Z.Y., 2009. Rayleigh wave group velocity tomography from ambient seismic noise in North China. Chin. J. Geophys. 52 (3), 663–671 (in Chinese with English Abstract).
Fang, L., Wu, J., Ding, Z., Panza, G., 2010. High resolution Rayleigh wave group velocity tomography in North China from ambient seismic noise. Geophys. J. Int. 181 (2), 1171–1182.
Faure, M., Trap, P., Lin, W., Monié, P., Bruguier, O., 2007. Polyorogenic evolution of the Paleoproterozoic Trans-North China Belt, new insights from the in Lüliangshan–Hengshan–Wutaishan and Fuping massifs. Episodes 30, 95–106.
Feng, R., Yan, H.F., Zhang, R.S., 1986. Fast inversion method and corresponding programming for 3D potential field. Acta Geol. Sin. 4 (3), 390–402 (in Chinese with English abstract).
Foulger, G.R., Panza, G.F., Artemieva, I.M., Bastow, I.D., Cammarano, F., Evans, J.R., Hamilton, W.R., Julina, B.R., Lustrino, M., Thybo, H., Yanovskaya, T.B., 2013. Caveats on tomographic images. Terra Nova 25, 259–281. http://dx.doi.org/10.1111/ter.12041.
Frezzotti, M.L., Peccerillo, A., Panza, G.F., 2009. Carbonatemetasomatism and CO_2 lithosphere–asthenosphere degassing beneath the Western Mediterranean: an integrated model arising from petrological and geophysical data. Chem. Geol. 262, 108–120.
Fu, B.H., Awata, Y., 2007. Displacement and timing of left-lateral faulting in the Kunlun Fault Zone, northern Tibet, inferred from geologic and geomorphic features. J. Asian Earth Sci. 29, 253–265.
Fu, X.G., Wang, J., Tan, F.W., Chen, M., Chen, W.B., 2010. The Late Triassic rift-related volcanic rocks from eastern Qiangtang, northern Tibet (China): age and tectonic implications. Gondwana Res. 17, 135–144.
Fu, B.H., Shi, P.L., Guo, H.D., Okuyama, S., Ninomiya, Y., Wright, S., 2011a. Surface deformation related to the 2008 Wenchuan earthquake and mountain building of the Longmen Shan, eastern Tibetan Plateau. J. Asian Earth Sci. 40 (4), 805–824.
Fu, B.H., Walker, R., Sandiford, M., 2011b. The 2008 Wenchuan earthquake and active tectonics of Asia. J. Asian Earth Sci. 40 (4), 797–804.
Galvé, A., Hirn, A., Jiang, M., Gallart, J., de Voogd, B., Lépine, J.C., Diaz, J., Wang, Y.X., Qian, H., 2002. Modes of raising northeastern Tibet probed by explosion seismology. Earth Planet. Sci. Lett. 203, 35–43.
Gan, W., Zhang, P., Shen, Z.K., Niu, Z., Wang, M., Wan, Y., Zhou, D., Cheng, J., 2007. Present-day crustal motion within the Tibetan Plateau inferred from GPS measurements. J. Geophys. Res 112 (10.1029).
Gao, R., Cheng, X., Wu, G., 1999. Lithospheric structure and geodynamic model of the Golmud–Ejn transect in northern Tibet. Geol. Soc. Am. 328, 9–17.
Gao, S., Liu, X.M., Yuan, H.L., Hattendorf, B., Günther, D., Chen, L., Hu, S.H., 2002. Determination of forty two major and trace elements in USGS and NIST SRM glasses by laser ablation-inductively coupled plasma-mass spectrometry. Geostand. Newslett. 26, 181–195.
Gao, S., Rudnick, R., Yuan, H.L., 2004. Recycling lower continental crust in the North China craton. Nature 432, 892–897.
Gao, S., Rudnick, R.L., Xu, W.L., Yuan, H.L., Liu, Y.S., Walker, R.J., Puchtel, I.S., Liu, X., Huang, H., Wang, X.R., Yang, J., 2008. Recycling deep cratonic lithosphere and generation of intraplate magmatism in the North China Craton. Earth Planet. Sci. Lett. 270 (1–2), 41–53.
Goodwin, A.M., 1996. Principles of Precambrian Geology.Academic Press, London.
Goscombe, B., Gray, D., Hand, M., 2005. Extrusional tectonics in the core of a transpressional orogen; the Kaoko Belt, Namibia. J. Petrol. 46 (6), 1203–1241.
Götze, H.J., 1984. Über den Einsatz interaktiver Computergraphik im Rahmen 3-dimensionaler Interpretationstechniken in Gravimetrie und Magnetik. Habilitations-Schrift, 121. Technische Universität Clausthal (121 pp.).
Götze, H.J., Lahmeyer, B., 1988. Application of three-dimensional interactive modeling in gravity and magnetics. Geophysics 53 (8), 1096–1108.
Griffin, W., O'Reilly, S., 2003. The origin and evolution of Archean lithospheric mantle. Precambrian Res. 127 (1–3), 19–41.
Griffin, W.L., Zhang, A.D., O'Reilly, S.Y., Ryan, C.G., 1998. Phanerozoic evolution of the lithosphere beneath the Sino-Korean Craton. In: Flower, M., Chung, S.L., Lo, C.H., Lee, T.Y. (Eds.), Mantle Dynamics and Plate Interactions in East Asia. American Geophysical Union, Geodynamics Series, 100, pp. 107–126.
Griffin, W.L., O'Reilly, S.Y., Ryan, C.G., 1999. The composition and origin of sub-continental mantle. In: Fei, Y., Bertka, M., Mysen, B.O. (Eds.), Mantle Petrology: Field Observations and High-pressure Experimentation: A Tribute to France R. (Joe) Boyd. Geochemical Society, Special Publications, 1, pp. 13–46.
Gripp, A.E., Gordon, R.G., 2002. Young tracks of hotspots and current plate velocities. Geophys. J. Int. 150, 321–361. http://dx.doi.org/10.1046/j.1365-246X.2002.01627.x.
Guo, P., Santosh, M., Li, S., 2013. Geodynamics of gold metallogeny in the Shandong Province, NE China: an integrated geological, geophysical and geochemical perspective. Gondwana Res. 24 (3–4), 1172–1202.
Hacker, B.R., Ratschbacher, L., Webb, L., 2000. Exhumation of ultrahigh-pressure continental crust in east central China: late Triassic–early Jurassic tectonic unroofing. J. Geophys. Res. 105 (B6), 13339–13364.
Haines, S.S., Klemperer, S.L., Brown, L., Jingru, G., Mechie, J., Meissner, R., Ross, A., Wenjin, Z., 2003a. Crustal thickening processes in central Tibet: implications of INDEPTH III seismic data. Tectonics 22, 1–18.
Haines, S.S., Klemperer, S.L., Brown, L., Guo, J., Mechie, J., Meissner, R., Ross, A., Zhao, W., 2003b. INDEPTH III seismic data: from surface observations to deep crustal processes in Tibet. Tectonics 22 (1). http://dx.doi.org/10.1029/2001TC001305.
Harley, S.L., 1989. The origins of granulites; a metamorphic perspective. Geol. Mag. 126, 215–247.
Harley, S.L., 2004. Extending our understanding of ultrahigh temperature crustal metamorphism. J. Mineral. Petrol. Sci. 99 (4), 140–158.
Harris, N.B.W., Holland, T.J.B., Tindle, A.G., 1988. Metamorphic rocks of the 1985 Tibet Geotraverse, Lhasa to Golmud. Philos. Trans. R. Soc. Lond. A 327, 203–213.
Harrison, T.M., Copeland, P., Kidd, W.S.F., Yin, A., 1992. Raising Tibet. Science 255, 1663–1670.
Harrison, T.M., Grove, M., Lovera, O.M., Catlos, E.J., 1998. A model for the origin of Himalayan anatexis and inverted metamorphism. J. Geophys. Res. 103, 27017–27032.
Hauck, M.L., Nelson, K.D., Brown, L.D., Zhao, W., Ross, A.R., 1998. Crustal structure of the Himalayan orogen at 90 east longitude from project INDEPTH deep reflection profiles. Tectonics 17, 481–500.
Henry, P., Le Pichon, X., Goff, B., 1997. Kinematic, thermal and petrological model of the Himalayas: constraints related to metamorphism within the underthrust Indian crust. In: Touret, J.L.R., Austrheim, H. (Eds.), Collisional Orogens: Zones of Active Transfer Between Crust and Mantle. Tectonophysics, 273, pp. 31–56.
Hetényi, G., Cattin, P., Bruneta, F., Bollinger, L., Vergne, J., Nábělek, J.L., Diament, M., 2007. Density distribution of the India plate beneath the Tibetan plateau: geophysical and petrological constraints on the kinetics of lower-crustal eclogitization. Earth Planet. Sci. Lett. 264 (1–2), 226–244.
Hirn, A., Lépine, J.C., Jobert, M., Jobert, G., Xu, Z.X., Gao, E.Y., Yuan, L.D., Teng, J.W., 1984a. Crustal structure and variability of the Himalayan border of Tibet. Nature 307, 23–25.
Hirn, A., Nercessian, A., Sapin, M., Jobert, G., Xu, Z.X., Gao, E.Y., Lu, D.Y., Teng, J.W., 1984b. Lhasa Block and bordering sutures; a continuation of a 500-km Moho traverse through Tibet. Nature 307, 25–27.
Hirn, A., Jiang, M., Sapin, M., Diaz, J., Nercessian, A., Lu, Q., Lepine, J., Shi, D., Sachpazi, M., Pandey, M., 1995. Seismic anisotropy as an indicator of mantle flow beneath the Himalayas and Tibet. Nature 375, 571–574.
Hodges, K.V., 2000. Tectonics of the Himalaya and southern Tibet from two perspectives. Geol. Soc. Am. Bull. 112, 324–350.
Hoffman, P.F., 1988. United Plates of America, the birth of a craton — Early Proterozoic assembly and growth of Laurentia. Annu. Rev. Earth Planet. Sci. 16 (A88), 22–46 (52285).
Holt, W.E., Li, M., Haines, A., 1995. Earthquake, strain rates and instantaneous relative motion within central and east Asia. Geophys. J. Int. 122, 569–593.
Houseman, G., England, P., 1996. A lithospheric-thickening model for the Indo-Asian collision. In: Yin, A., Harrision, T.M. (Eds.), The Tectonic Evolution of Asia. Cambridge University, pp. 3–17.
Houseman, G.A., Molnar, P., 1997. Gravitational (Rayleigh–Taylor) instability of a layer with non-linear viscosity and convective thinning of continental lithosphere. Geophys. J. Int. 128, 125–150.
Houseman, G.A., McKenzie, D.P., Molnar, P., 1981. Convective instability of a thickened boundary layer and its relevance for the thermal evolution of continental convergent belts. J. Geophys. Res. 86. http://dx.doi.org/10.1029/JB086iB07p06115.
Hsü, H.T., Lu, Y., 1995. The regional geopotential model in China. Boll. Geodesia Sci. Affiini LIV (N2), 161–175.
Hsü, K.J., Pan, G.T., Sengör, A.M.C., 1995. Tectonic evolution of the Tibetan Plateau: a working hypothesis based on the archipelago model of orogenesis. Int. Geol. Rev. 37 (6), 473–508.
Hu, J.F., Xu, X.Q., Yang, H.Y., Wen, L.M., Li, G.G., 2011. S receiver function analysis of the crustal and lithospheric structures beneath eastern Tibet. Earth Planet. Sci. Lett. 306 (1–2), 77–85.
Hu, J.F., Xu, X.Q., Yang, H.Y., Wen, L.M., Li, G.G., 2012. Lithospheric structure and crust–mantle decoupling in the southeast edge of the Tibetan Plateau. Gondwana Res. 22 (3–4), 1060–1067.
Huang, J., Zhao, D., 2004. Crustal heterogeneity and seismotectonics of the region around Beijing, China. Tectonophysics 385 (1–4), 159–180.
Huang, S., Pollack, H.N., Shen, P.Y., 2000. Temperature trends over the last five centuries reconstructed from borehole temperatures. Nature 403, 756–758.
Huang, H., Polat, A., Fryer, B., 2013. Origin of Archean tonalite–trondhjemite–granodiorite (TTG) suites and granites. Gondwana Res. 23, 452–470.
Jahn, B., Windley, B., Dobrestov, N., 2004. Phanerozoic continental growth in Central Asia. J. Asian Earth Sci. 23, 599–603.

Ji, S., Wang, Q., Marcotte, D., Salisbury, M.H., Xu, Z., 2007. P wave velocities, anisotropy and hysteresis in ultrahighpressure metamorphic rocks as a function of confining pressure. J. Geophys. Res. 112, B09204. http://dx.doi.org/10.1029/2006JB004867.
Jia, S.X., Zhang, X.K., 2005. Crustal structure and comparison of different tectonic blocks in North China. Chin. J. Geophys. 48, 611–620 (in Chinese with English abstract).
Jia, S., Qi, C., Wang, F., Chen, Q., Zhang, X., Chen, Y., 2005. Three dimensional crustal gridded structure of the capital area. Chin. J. Geophys. 48 (6), 1316–1324 (in Chinese with English abstract).
Jiang, M., Galvé, A., Hirn, A., de Voogd, B., Laigle, M., Su, H.P., Diaz, J., Lépine, J.C., Wang, Y.X., 2006a. Crustal thickening and variations in architecture form the Qaidam basin to the Qang Tang (North-Central Tibetan Plateau) from wideangle reflection seismology. Tectonophysics 412, 121–140.
Jiang, Y.H., Jiang, S.Y., Ling, H.F., Dai, B.Z., 2006b. Low-degree melting of a metasomatic lithospheric mantle for the origin of Cenozoic Yulong monzogranite-porphyry, east Tibet: geochemical and Sr–Nd–Pb–Hf isotopic constrints. Earth Planet. Sci. Lett. 241, 617–633.
Jiang, Y.H., Jin, G.D., Liao, S.Y., Zhou, Q., Zhao, P., 2010. Geochemical and Sr–Nd–Hf isotopic constraints on the origin of Late Triassic granitoids from the Qinling orogeny, central China: implications for a continental arc to continent–continent collision. Lithos 117, 183–197.
Jiang, Y.H., Liu, Z., Jia, R.Y., Liao, S.Y., Zhou, Q., Zhao, P., 2012. Miocene potassic granite–syenite association in western Tibetan Plateau: implications for shoshonitic and high Ba–Sr granite genesis. Lithos 134–135, 146–162.
Jiménez-Munt, I., Fernàndez, M., Vergés, J., Platt, J.P., 2008. Lithosphere structure underneath the Tibetan Plateau inferred from elevation, gravity and geoid anomalies. Earth Planet. Sci. Lett. 267 (1–2), 276–289.
Jordan, T.H., 1978. Composition and development of the continental tectosphere. Nature 274, 544–548.
Kaila, K., Narain, H., 1976. Evolution of the Himalaya Based on Seismotectonics and Deep Seismic Soundings.National Geophysical Research Institute.
Kapp, P., Yin, A., Manning, C.E., Harrison, T.M., Taylor, M.H., Ding, L., 2003. Tectonic evolution of the early Mesozoic blueschist-bearing Qiangtang metamorphic belt, central Tibet. Tectonics 22, 1043. http://dx.doi.org/10.1029/2002TC001383.
Karplus, M., Zhao, W.J., Klemperer, S., Wu, Z., Mechie, J., Shi, D.N., Brown, L., Chen, C., 2011. Injection of Tibetan crust beneath the south Qaidam Basin: evidence from INDEPTH IV wide-angle seismic data. J. Geophys. Res. 116, B07301.
Kawai, K., Yamamoto, S., Tsuchiya, T., Maruyama, S., 2013. The second continent: Existence of granitic continental materials around the bottom of the mantle transition zone. Geosci. Front. 4, 1–6.
Khain, E., Bibikova, E., Kröner, A., Zhuravlev, D., Sklyarov, E., Fedotova, A., Kravchenko-Berezhnoy, I., 2002. The most ancient ophiolite of the Central Asian fold belt: U–Pb and Pb–Pb zircon ages for the Dunzhugur Complex, Eastern Sayan, Siberia, and geodynamic implications. Earth Planet. Sci. Lett. 199 (3), 311–325.
Kind, R., Yuan, X., 2010. Seismic images of the biggest crash on Earth. Science 329 (5998), 1479–1480.
Kind, R., Yuan, X., Saul, J., Nelson, D., Sobolev, S.V., Mechie, J., Zhao, W., Kosarev, G., Ni, J., Achauer, U., Jiang, M., 2002. Seismic images of crust and upper mantle beneath Tibet: evidence for Eurasian plate subduction. Science 298 (5596), 1219–1221.
Klemperer, S.L., 2006. Crustal flow in Tibet: geophysical evidence for the physical state of Tibetan lithosphere, and inferred patterns of active flow. In: Law, R.D., Searle, M.P., Godin, L. (Eds.), Channel Flow, Ductile Extrusion and Exhumation in Continental Collision Zones. Geol. Soc. Lond. Special Publication, vol. 268, pp. 39–70.
Klose, C.D., Seeber, L., 2007. Shallow seismicity in stable continental regions. Seismol. Res. 78 (5), 554–562.
Knopoff, L., 1972. Observations and inversion of surface-wavedispersion. In: Ritsema, A.R. (Ed.), The Upper Mantle. Tectonophysics, 13, pp. 497–519.
Knopoff, L., Panza, G.F., 1977. Resolution of upper mantle structureusing higher modes of Rayleigh waves. Ann. Geophys. 30, 491–505.
Kong, X., Bird, P., 1996. Neotectonics of Asia: thin-shell finite element models with faults. In: Yin, A., Harrison, T.M. (Eds.), The Tectonic Evolution of Asia. Cambridge University Press, Cambridge, pp. 18–34.
Kong, X., Yin, A., Harrison, T.M., 1997. Evaluating the role of preexisting weakness and topographic distributions in the Indo-Asian collision by use of a thin-shell numerical model. Geology 25, 527–530.
Kosarev, G., Kind, R., Sobolev, S.V., Yuan, X., Hanka, W., Oreshin, S., 1999. Seismic evidence for a detached Indian lithospheric mantle beneath Tibet. Science 283, 1306–1309.
Kovalenko, V.I., Yarmolyuk, V.V., Kovach, V.P., Kotov, A.B., Kozakov, I.K., Salnikova, E.B., Larin, A.M., 2004. Isotope provinces, mechanisms of generation and sources of the continental crust in the Central Asian mobile belt: geological and isotopic evidence. J. Asian Earth Sci. 23 (5), 605–627.
Kröner, A., Layer, P.W., 1992. Crust formation and plate motion in the early Archean. Science 256 (5062), 1405–1411 (New York, N.Y.).
Kröner, A., Cui, W.Y., Wang, S.Q., Wang, C.Q., Nemchin, A.A., 1998. Single zircon ages from high-grade rocks of the Jianping Complex, Liaoning Province, NE China. J. Asian Earth Sci. 16 (5–6), 519–532.
Kröner, A., Wilde, S., Li, J., Wang, K., 2005. Age and evolution of a late Archean to Paleoproterozoic upper to lower crustal section in the Wutaishan/Hengshan/Fuping terrain of northern China. J. Asian Earth Sci. 24, 577–595.
Kröner, A., Wilde, S., Zhao, G., O'Brien, P., Sun, M., Liu, D., Wan, Y., Liu, S., Guo, J., 2006. Zircon geochronology and metamorphic evolution of mafic dykes in the Hengshan Complex of northern China: evidence for late Palaeoproterozoic extension and subsequent high-pressure metamorphism in the North China Craton. Precambrian Res. 146, 45–67.
Kröner, A., Kovach, V., Belousova, E., Hegner, E., Armstrong, R., Dolgopolova, A., Seltmann, R., Alexeiev, D.V., Hoffmann, J.E., Wong, J., Sun, M., Cai, K., Wang, T., Tong, Y., Wilde, S.A., Degtyarev, K.E., Rytsk, E., 2014. Reassessment of continental growth during the accretionary history of the Central Asian Orogenic Belt. Gondwana Res. 25 (1), 103–125.
Kukkonen, I.T., Kuusisto, M., Lehtonen, M., Peltonen, P., 2008. Delamination of eclogitized lower crust: control on the crust–mantle boundary in the central Fennoscandian shield. Tectonophysics 457, 111–127.
Kumar, P., Yuan, X., Kind, R., Ni, J., 2006. Imaging the colliding Indian and Asian lithospheric plates beneath Tibet. J. Geophys. Res. 111, B06308.
Kusky, T.M., 1990. Evidence for Archean ocean opening and closing in the Southern Slave Province. Tectonics 9 (6), 1533–1563. http://dx.doi.org/10.1029/TC009i006p01533.
Kusky, T.M., Li, J.H., 2003. Paleoproterozoic tectonic evolution of the North China Craton. J. Asian Earth Sci. 22, 383–397.
Kusky, T.M., Li, J.H., 2010. Origin and emplacement of ophiolites of the Central Orogenic belt, North China craton. J. Earth Sci. 21 (5), 744–781. http://dx.doi.org/10.1007/s12583-010-0119-8.
Kusky, T.M., Li, J.H., Tucker, R.T., 2001. The Archean Dongwanzi ophiolite complex, North China Craton: 2.505 billion year old oceanic crust and mantle. Science 292, 1142–1145.
Kusky, T.M., Ganley, R., Lytwyn, J., Polat, A., 2004a. The Resurrection Peninsula ophiolite, mélange and accreted flysch belts of Southern Alaska as an analog for trench–forearc systems in Precambrian orogens. Dev. Precambrian Geol. 13, 627–674.
Kusky, T.M., Li, J.H., Glass, A., Huang, X.N., 2004b. Origin and emplacement of Archean ophiolites of the central orogenic belt, North China Craton. Dev. Precambrian Geol. 13, 223–274.
Kusky, T.M., Windley, B.F., Zhai, M.G., 2007. Tectonic evolution of the North China Block: from orogeny to craton to orogeny. In: Zhai, M.G., Windley, B.F., Kusky, T.M., Meng, Q.R. (Eds.), Mesozoic Sub-continental Lithospheric Thinning Under Eastern Asia. Geol. Soc. London, Spec. Publ., 280, pp. 1–34.
Lacassin, R., Leloup, P.H., Trinh, P.T., Tapponnier, P., 1998. Unconformity of red sandstones in north Vietnam: field evidence for Indosinian orogeny in northern Indochina? Terra Nova 10, 106–111.
Larson, K., Bürgmann, R., Bilhaln, R., Freymueller, J., 1999. Kinematics of the India–Eurasia collision zone from GPS measurements. J. Geophys. Res. 104, 1077–1093.
Le Fort, P., 1996. Evolution of the Himalaya. In: Yin, A., Harrison, T.M. (Eds.), The Tectonics of Asia. Cambridge Univ. Press, New York, pp. 95–106.
Le Pichon, X., Fournier, M., Jolivet, L., 1992. Kinematics, topography, shortening, and extrusion in the India–Eurasia collision. Tectonics 11 (6), 1085–1098.
Le Pichon, X., Henry, P., Goffé, B., 1997. Uplift of Tibet: from eclogites to granulites—implications for the Andean Plateau and the Variscan belt. Tectonophysics 273, 57–76.
Lee, T.Y., Lawver, L.A., 1995. Cenozoic plate reconstruction of Southeast Asia. Tectonophysics 251, 85–138.
Lee, C.T., Yin, Q.Z., Rudnick, R.L., Chesley, J.T., Jacobsen, S.B., 2000. Osmium isotopic evidence for Mesozoic removal of lithospheric mantle beneath the Sierra Nevada, California. Science 289, 1912–1916.
Lei, J., 2012. Upper-mantle tomography and dynamics beneath the North China Craton. J. Geophys. Res. 117 (B6), B06313.
Levshin, A.L., Ratnikova, L., Berger, J., 1992. Peculiarities of surface wave propagation across central Eurasia. Bull. Seism. Soc. Am. 82, 2464–2493.
Li, J.H., Kusky, T.M., 2007. A late Archean foreland fold and thrust belt in the North China Craton: implications for early collisional tectonics. Gondwana Res. 12, 47–66.
Li, S.L., Mooney, W.D., 1998. Crustal structure of China from deep seismic sounding profiles. Tectonophysics 288, 105–113.
Li, Y., Oldenburg, D.W., 1996. 3-D inversion of magnetic data. Geophysics 61, 394–408.
Li, Y., Oldenburg, D.W., 1998. 3D inversion of gravity data. Geophysics 63, 109–119.
Li, S.Z., Zhao, G.C., 2007. SHRIMP U–Pb zircon geochronology of the Liaoji granitoids: constraints on the evolution of the Paleoproterozoic Jiao–Liao–Ji belt in the Eastern Block of the North China Craton. Precambrian Res. 158, 1–16.
Li, S.G., Xiao, T.L., Liou, D.L., Chen, Y., Ge, N., Zhang, Z., Sun, S., Cong, B., Zhang, R., Hart, S.R., Wang, S., 1993. Collision of the North China and Yangtze Blocks and formation of coesite-bearing eclogites: timing and processes. Chem. Geol. 109, 89–111.
Li, S.Z., Zhao, G.C., Sun, M., Wu, F.Y., Liu, J.Z., Hao, D.F., Han, Z.Z., Luo, Y., 2004. Mesozoic, not Paleoproterozoic SHRIMP U–Pb zircon ages of two Liaoji granites, Eastern Block, North China Craton. Int. Geol. Rev. 46, 162–176.
Li, S.L., Mooney, W., Fan, J., 2006. Crustal structure of mainland China from deep seismic sounding profiles. Tectonophysics 288, 105–113.
Li, C., van der Hilst, R.D., Meltzer, A.S., Engdahl, E.R., 2008. Subduction of the Indian lithosphere beneath the Tibetan Plateau and Burma. Earth Planet. Sci. Lett. 274 (1–2), 157–168.
Li, H., Lu, S., Su, W., Xiang, Z., Zhou, H., Zhang, Y., 2013a. Recent advances in the study of the Mesoproterozoic geochronology in the North China Craton. J. Asian Earth Sci. 72, 216–227.
Li, S., Santosh, M., Zhang, H., Shen, J., Dong, G., Wang, J., Zhang, J., 2013b. Inhomogeneous lithospheric thinning in the central North China Craton: Zircon U–Pb and S–He–Ar isotopic record from magmatism and metallogeny in the Taihang Mountains. Gondwana Res. 23 (1), 141–160.
Li, S., Wang, T., Wilde, S.A., Tong, Y., 2013c. Evolution, source and tectonic significance of Early Mesozoic granitoid magmatism in the Central Asian Orogenic Belt (central segment). Earth Sci. Rev. 126, 206–234.
Lin, F.C., Ritzwoller, M.H., Townend, J., Savage, M., Bannister, S., 2007. Ambient noise Rayleigh wave tomography of New Zealand. Geophys. J. Int. 170 (2), 649–666.
Liu, G., Sun, J., Liu, J., 1989. The electrical structure of the crust and upper mantle in North China. In: Ma, X. (Ed.), Lithospheric Dynamics ATLAS of China. China Cartographic Press, Beijing, pp. 59–62 (in Chinese).

Liu, S.W., Liang, H.H., Zhao, G.C., Hua, Y.G., Jian, A.H., 2000. Isotopic chronology and geological events of Precambrian complex in the Taihangshan region. Sci. China Ser. D 43, 386–393.
Liu, F.L., Xu, Z.Q., Katayama, I., Yang, J.S., Maruyama, S., Liou, J.G., 2001a. Mineral inclusions in zircons of para- and orthogneiss from pre-pilot drillhole CCSD-PP1, Chinese Continental Scientific Drilling Project. Lithos 59, 199–215.
Liu, J.B., Ye, K., Maruyama, S., Cong, B.L., Fan, H.R., 2001b. Mineral inclusions in zircon from gneisses in the ultrahigh-pressure zone of the Dabie Mountains, China. J. Geol. 109, 523–535.
Liu, M., Cui, X., Liu, F., 2004. Cenozoic rifting and volcanism in eastern China a mantle dynamic link to the Indo-Asian collision. Tectonophysics 393, 29–42.
Liu, S., Hu, R.Z., Feng, C.X., Zou, H.B., Li, C., Chi, X.G., Peng, J.T., Zhong, H., Qi, L., Qi, Y.Q., Wang, T., 2008. Cenozoic high Sr/Y volcanic rocks in the Qiangtang terrane, northern Tibet: geochemical and isotopic evidence for the origin of delaminated lower continental melts. Geol. Mag. 145, 463–474.
Lobkis, O.I., Weaver, R.L., 2001. On the emergence of the Green's function in the correlations of a diffuse field. J. Acoust. Soc. Am. 110, 3011–3017.
Luo, Y., Sun, M., Zhao, G.C., Li, S.Z., Xu, P., Ye, K., Xia, X.P., 2004. LA-ICP-MS U–Pb zircon ages of the Liaohe Group in the Eastern Block of the North China Craton: constraints on the evolution of the Jiao–Liao–Ji Belt. Precambrian Res. 134, 349–371.
Mahéo, G., Guillot, S., Blichert-Toft, J., Rolland, Y., Pêcher, A., 2002. A slab breakoff model for the Neogene thermal evolution of South Karakorum and South Tibet. Earth Planet. Sci. Lett. 195 (1), 45–58.
Makovsky, Y., Klemperer, S.L., Huang, L.Y., Lu, D.Y., TEAM Project INDEPTH, 1996. Structural elements of the southern Tethyan Himalaya crust from wide-angle seismic data. Tectonics 15, 997–1005.
Makovsky, Y., Klemperer, S.L., Ratschbacher, L., Alsdorf, D., 1999. Midcrustal reflector on INDEPTH wide-angle profiles: an ophiolitic slab beneath the India–Asia suture in southern Tibet? Tectonics 18, 793–808.
Manikyamba, C., Kerrich, R., 2012. Eastern Dharwar Craton, India: continental lithosphere growth by accretion of diverse plumes and arc terranes. Geosci. Front. 3, 225–240.
Martin, H., Smithies, R.H., Rapp, R., Moyen, J.F., Champion, D., 2005. An overview of adakite, tonalite–trondhjemite–granodiorite (TTG), and sanukitoid: relationships and some implications for crustal evolution. Lithos 79, 1–24.
McKenzie, D., Priestley, K., 2008. The influence of lithospheric thickness variation on continental evolution. Lithos 102, 1–11.
McNamara, D.E., Owens, T.J., Walter, W.R., 1995. Observations of the regional phase propagation in the Tibetan plateau. J. Geophys. Res. 100, 22215–22229.
Mechie, J., Kind, R., 2013. A model of the crust and mantle structure down to 700 km depth beneath the Lhasa to Golmud transect across the Tibetan plateau as derived from seismological data. Tectonophysics 606, 187–197.
Meissner, R., Tilmann, F., Haines, S., 2004. About the lithospheric structure of central Tibet, based on seismic data from the INDEPTH III profile. Tectonophysics 380 (1), 1–25.
Meng, Q.R., 2003. What drove late Mesozoic extension of the northern China–Mongolia tract? Tectonophysics 369, 155–174.
Meng, Q.R., Zhang, G.W., 2000. Geologic framework and tectonic evolution of the qinling orogen, central China. Tectonophysics 323, 183–196.
Mengel, K., Kern, H., 1990. Petrologic versus seismic Moho and crustal root mysteries of the Hercynian orogen. In: Freeman, R., Giese, P., Mueller, S. (Eds.), The European Geotraverse: Integrative Studies—Results from the 5th Earth Science Study Centre. European Science Foundation, Strasbourg, pp. 169–176.
Menzies, M.A., Xu, Y.G., 1998. Geodynamics of the North China Craton. In: Flower, M.F.J., Chung, S.L., Lo, C.H., Lee, T.Y. (Eds.), Mantle Dynamics and Plate Interactions in East Asia. American Geophysical Union, Geodynamics Series, 27, pp. 155–165.
Menzies, M.A., Fan, W.M., Zhang, M., 1993. Paleozoic and Cenozoiclithosprobes and the loss of >120 km of Archean lithosphere, Sino-Korean Craton, China. In: Prichard, H.M., Alabaster, T., Harris, N.B.W., Neary, C.R. (Eds.), Magmatic Processes and Plate Tectonics. Geol. Soc. Spec. Pub, 76, pp. 71–78.
Menzies, M.A., Xu, Y.G., Zhang, H.F., Fan, W.M., 2007. Integration of geology, geophysics and geochemistry: a key to understanding the North China Craton. Lithos 96, 1–21.
Metcalfe, 1996. Pre-Cretaceous evolution of SE Asian terranes. In: Hall, R., Blundell, D. (Eds.), Tectonic Evolution of Southeast Asia. Geol. Soc. Spec. Pub., 106, pp. 97–122.
Metcalfe, 2006. Palaeozoic and Mesozoic tectonic evolution and palaeogeography of East Asian crustal fragments: the Korean Peninsula in context. Gondwana Res. 9, 24–46.
Min, Z., Wu, F.T., 1987. Nature of the upper crust beneath central Tibet. Earth Planet. Sci. Lett. 84, 204–210.
Mitchell, N.C., 1991. Distributed extension at the Indian Ocean triple junction Distributed extension at the Indian Ocean triple junction. J. Geophys. Res. 96 (B5), 8019.
Mitra, S., Priestley, K., Bhattacharyya, A.K., Gaur, V., 2005. Crustal structure and earthquake focal depths beneath northeastern India and southern Tibet. Geophys. J. Int. 160 (1), 227–248.
Mo, X.X., Zhao, Z.D., Deng, J.F., Dong, G.C., Zhou, S., Guo, T.Y., Zhang, S.Q., Wang, L.L., 2003. Response of volcanism to the India–Asia collision. Earth Sci. Front. 10, 135–148 (in Chinese with English abstract).
Mo, X.X., Hou, Z.Q., Niu, Y.L., Dong, G.C., Qu, X.M., Zhao, Z.D., Yang, Z.M., 2007. Mantle contributions to crustal thickening during continental collision: evidence from Cenozoic igneous rocks in southern Tibet. Lithos 96, 225–242.
Mo, X.X., Niu, Y.L., Dong, G.C., Zhao, Z.D., Hou, Z.Q., Zhou, S., Ke, S., 2008. Contribution of syncollisional felsic magmatism to continental crust growth: a case study of the Paleogene Linzizong volcanic succession in southern Tibet. Chem. Geol. 250, 49–68.
Mohan, G., Rai, S.S., Panza, G.F., 1997. Shear velocity structure of the laterally heterogeneous crust and uppermost mantle beneath the Indian region. Tectonophysics 277, 259–270.
Molnar, P., 1984. Structure and tectonics of the Himalaya: constraints and implications of geophysical data. Annu. Rev. Earth Planet. Sci. 12, 489–518.
Molnar, P., 1988. A review of geophysical constraints on the deep structure of the Tibetan plateau, the Himalaya, and the Karakoram, and their implications. Philos. Trans. R. Soc. Lond. A 326, 33–88.
Molnar, P., England, P., Martinod, J., 1993. Mantle dynamics, the uplift of the Tibetan Plateau, and the Indian monsoon. Rev. Geophys. 31, 357–396.
Mueller, S., Panza, G.F., 1986. Evidence of a deep-reaching lithospheric root under the Alpine Arc. In: Wezel, F.C. (Ed.), The Origin of Arcs, 21. Elsevier, pp. 93–113.
Nábělek, J., Hetényi, G., Vergne, J., Sapkota, S., Kafle, B., Jiang, M., Su, H., Chen, J., Huang, B.S., 2009. Underplating in the Himalaya–Tibet collision zone revealed by the Hi-CLIMB experiment. Science 325 (5946), 1371–1374.
Nance, R.D., Murphy, J.B., 2013. Origins of the supercontinent cycle. Geosci. Front. 4, 439–448.
Nance, R.D., Murphy, J.B., Santosh, M., 2014. The supercontinent cycle: a retrospective essay. Gondwana Res. 25, 4–29.
Nelson, K.D., et al., 1996. Partially molten middle crust beneath Southern Tibet: synthesis of Project INDEPTH results. Science 274, 1684–1696.
Ni, J., Barazangi, M., 1983. High-frequency seismic wave propagation beneath the Indian Shield, Himalayan Arc, Tibetan Plateau and surrounding regions: high uppermost mantle velocities and efficient Sn propagation beneath Tibet. Geophys. J. Int. 72 (3), 665–689.
Nisbet, 1987. The Young Earth: An Introduction to Archean Geology.G. Allen & Unwin, London.
Niu, Y., 2005. Generation and evolution of basaltic magmas: some basic concepts and a hypothesis for the origin of the Mesozoic–Cenozoic volcanism in eastern China. Geol. J. China Univ. 11, 9–46.
Nutman, A.P., Friend, C.R., Kinny, P.D., McGregor, V.R., 1993. Anatomy of an Early Archean gneiss complex: 3900 to 3600 Ma crustal evolution in southern West Greenland. Geology 21 (5), 415–418.
Nutman, A.P., Bennett, V.C., Friend, C.R., Mcgregor, V.R., 2000. The early Archaean Itsaq Gneiss Complex of southern West Greenland: the importance of field observations in interpreting age and isotopic constraints for early terrestrial evolution. Geochim. Cosmochim. Acta 64 (17), 3035–3060.
Omori, S., Komabayashi, T., Maruyama, S., 2004. Dehydration and earthquakes in the subducting slab: empirical link in intermediate and deep seismic zones. Phys. Earth Planet. Inter. 146 (1–2), 297–311.
Owens, T.J., Zandt, G., 1997. Implications of crustal property variations for models of Tibetan plateau evolution. Nature 387, 37–43.
Panza, G.F., 1980. Evolution of the Earth's lithosphere. In: Davies, P.A., Runcorn, S.K. (Eds.), Mechanisms of Continental Drift and Plate Tectonics. Academic Press, pp. 75–87.
Panza, G.F., 1981. The resolving power of seismic surface waves with respect to crust and upper mantle structural models. In: Cassinis, R. (Ed.), The Solution of the Inverse Problem in Geophysical Interpretation. Plenum Pub. Corp, pp. 39–77.
Panza, G., Mueller, S., 1979. The plate boundary between Eurasia and Africa in the Alpine area. Mem. Sci. Geol. 33, 43–50.
Panza, G.F., Raykova, R.B., 2008. Structure and rheology of lithosphere in Italy and surrounding. Terra Nova 20, 194–199. http://dx.doi.org/10.1111/j.1365-3121.2008.00805.x.
Panza, G.F., Peccerillo, A., Aoudia, A., Farina, B., 2007a. Geophysical and petrological modeling of the structure and composition of the crust and upper mantle in complex geodynamic settings: the Tyrrhenian Sea and surroundings. Earth Sci. Rev. 80, 1–46.
Panza, G.F., Raykova, R.B., Carminati, E., Doglioni, C., 2007b. Upper mantle flow in the western Mediterranean. Earth Planet. Sci. Lett. 257, 200–214. http://dx.doi.org/10.1016/j.epsl.2007.02.032.
Panza, G.F., Doglioni, C., Levshin, A., 2010. Asymmetric ocean basins. Geology 38, 59–62. http://dx.doi.org/10.1130/G30570.1.
Paul, J., Burgmann, R., Gaur, V., Bilham, R., Larson, K., Ananda, M., Jade, S., Mukal, M., Anupama, T., Satyal, G., 2001. The motion and active deformation of India. Geophys. Res. Lett. 28 (4), 647–650.
Peltzer, G., Saucier, F., 1996. Present day kinematics of Asia derived from geologic fault rates. J. Geophys. Res. 101, 27943–27956.
Peltzer, G., Tapponnier, P., 1988. Formation and evolution of strike-slip faults, rifts, and basins during the India–Asia collision: an experimental approach. J. Geophys. Res. 93, 15085–15117.
Peng, P., 2010. Reconstruction and interpretation of giant mafic dyke swarms: a case study of 1.78 Ga magmatism in the North China craton. Geol. Soc. Lond. Spec. Publ. 338 (1), 163–178.
Peng, P., Zhai, M.G., Ernst, R., Guo, J.H., Liu, F., Hu, B., 2008. A 1.78 Ga Large Igneous Province in the North China craton: the Xiong'er Volcanic Province and the North China dyke swarm. Lithos 101 (3–4), 260–280.
Polat, A., Kusky, T., Li, J.H., Fryer, B., Patrick, K., 2005. Geochemistry of the Late Archean (ca. 2.55–2.50 Ga) volcanic and ophiolitic rocks in the Wutaishan Greenstone Belt, Central Orogenic Belt, North China Craton: implications for geodynamic setting and continental growth. Geol. Soc. Am. Bull. 117, 1387–1399.
Polat, A., Herzberg, C., Münker, C., Rodgers, R., Kusky, T., Li, J.H., Fryer, B., Delaney, J., 2006. Geochemical and petrological evidence for a supra-subduction zone origin of Neoarchean (ca. 2.5 Ga) peridotites, central orogenic belt, North China craton. Geol. Soc. Am. Bull. 118, 771–784. http://dx.doi.org/10.1130/B25845.1.
Poudjom, D.Y.H., O'Reilly, S.Y., Griffin, W.L., Morgan, P., 2001. The density structure of subcontinental lithosphere through time. Earth Planet. Sci. Lett. 184, 605–621.
Powell, C. McA, 1986. Continental underplating model for the rise of the Tibetan Plateau. Earth Planet. Sci. Lett. 81 (1), 79–94.
Powell, C.M., Conaghan, P.J., 1973. Plate tectonics and the Himalaya. Earth Planet. Sci. Lett. 20, 1–12.
Qiu, R.Z., Deng, J.F., Zhou, S., Li, J.F., Xiao, Q.H., Wu, Z.X., Liu, C., 2005. Lithosphere types in North China: evidence from geology and geophysics. Sci. China Ser D 48 (11), 1809–1827.

Riguzzi, F., Pietrantonioa, G., Piersantia, A., Mahmoudc, S.M., 2006. Current motion and short-term deformations in the Suez–Sinai area from GPS observations. J. Geodyn. 41 (5), 485–499.
Riguzzi, F., Panza, G., Varga, P., Doglioni, C., 2010. Can Earth's rotation and tidal despinning drive plate tectonics. Tectonophysics 484, 60–73. http://dx.doi.org/10.1016/j.tecto.2009.06.012.
Riley, T.R., Leat, P.T., Kelley, S.P., Millar, I.L., Thirlwall, M.F., 2003. Thinning of the Antarctic Peninsula lithosphere through the Mesozoic: evidence from Middle Jurassic basaltic lavas. Lithos 67, 163–179.
Rogers, J.W., Santosh, M., 2003. Supercontinents in Earth history. Gondwana Res. 6 (3), 357–368.
Rogers, J.W., Santosh, M., 2004. Continents and Supercontinents.Oxford University Press.
Rowley, D.B., 1998. Minimum age of initiation of collision between India and Asia north of Everest based on the subsidence history of the Zhepure Mountain section. J. Geol. 106, 229–235.
Royden, L.H., 1993. The steady state thermal structure of eroding orogenic belts and accretionary prisms. J. Geophys. Res. 98, 4487–4507.
Royden, L., 1996. Coupling and decoupling of crust and mantle in convergent orogens: implications for strain partitioning in the crust. J. Geophys. Res. 101, 17,679–17,705.
Royden, L.H., Burchfiel, B.C., King, R.W., Wang, E., Chen, Z., Shen, F., Liu, Y., 1997. Surface deformation and lower crustal flow in eastern Tibet. Science 276, 788–790.
Royden, L.H., Burchfiel, B.C., van der Hilst, R.D., 2008. The geological evolution of the Tibetan Plateau. Science 321 (5892), 1054–1058.
Rudnick, R.L., Fountain, D.M., 1995. Nature and composition of the continental crust: a lower crustal perspective. Rev. Geophys. 33 (3), 267–310.
Rudnick, R.L., Gao, S., Ling, W.-l, Liu, Y.-S., McDonough, W.F., 2004. Petrology and geochemistry of spinel peridotite xenoliths from Hannuoba and Qixia, North China craton. Lithos 77, 609–637.
Santosh, M., 2010. Assembling North China Craton within the Columbia supercontinent: the role of double-sided subduction. Precambrian Res. 178, 149–167.
Santosh, M., Wilde, S., Li, J.H., 2007a. Timing of Paleoproterozoic ultrahigh-temperature metamorphism in the North China Craton: evidence from SHRIMP U–Pb zircon geochronology. Precambrain Res. 159, 178–196.
Santosh, M., Tsunogae, T., Li, J., Liu, S., 2007b. Discovery of sapphirine-bearing Mg–Al granulites in the North China Craton: implications for Paleoproterozoic ultrahigh temperature metamorphism. Gondwana Res. 11 (3), 263–285.
Santosh, M., Sajeev, K., Li, J., Liu, S., Itaya, T., 2009. Counterclockwise exhumation of a hot orogen: the Paleoproterozoic ultrahigh-temperature granulites in the North China Craton. Lithos 110 (1), 140–152.
Santosh, M., Maruyama, S., Komiya, T., Yamamoto, S., 2010. Orogens in the evolving Earth: from surface continents to 'lost continents' at the core mantle boundary. Geol. Soc. Lond. Spec. Publ. 338, 77–116.
Santosh, M., Yang, Q.Y., Shaji, E., Tsunjogae, T., Ram Mohan, M., Satyanarayanan, M., 2013. An exotic Mesoarchean microcontinent: the Coorg Block, southern India. Gondwana Res. http://dx.doi.org/10.1016/j.gr.2013.10.005.
Schmidt, S., 1996. 3D modeling of geoid and gravity using GIS-functions. Proceedings of the 7th International Meeting on Alpine Gravimetry. Österreichische Beiträge zu Meteorologie und Geophysik, Heft 14, pp. 137–144 (Wien).
Schmidt, S., Götze, H.J., 1998. Interactive visualization and modification of 3D models using GIS functions. Phys. Chem. Earth 23 (3), 289–295.
Schulte-Pelkum, V., Monsalve, G., Sheehan, A., Pandey, M.R., Sapkota, S., Bilham, R., Wu, F., 2005. Imaging the Indian subcontinent beneath the Himalaya. Nature 435, 1222–1225. http://dx.doi.org/10.1038/nature03678.
Scoppola, B., Boccaletti, D., Bevis, M., Carminati, E., Doglioni, C., 2006. The westward drift of the lithosphere: a rotational drag? Geol. Soc. Am. Bull. 118, 199–209.
Searle, M.P., 1996. Cooling history, erosion, exhumation, and kinematics of the Himalaya–Karakoram–Tibet orogenic belt. In: Yin, A., Harrison, T.M. (Eds.), The Tectonic Evolution of Asia. Cambridge Univ. Press, New York, pp. 110–137.
Sengör, A., Burtman, V., 1993. Evolution of the Altaid tectonic collage and Palaeozoic crustal growth in Eurasia. Nature 364, 299–307.
Sengör, A.M.C., Natal'in, B.A., 1996. Paleotectonics of Asia: fragments of a synthesis. In: Yin, A., Harrison, T.M. (Eds.), The Tectonics of Asia. Cambridge Univ, New York, pp. 486–640.
Shapiro, N.M., Campillo, M., 2004. Emergence of broadband Rayleigh waves from correlations of the ambient seismic noise. Geophys. Res. Lett. 31, L07614. http://dx.doi.org/10.1029/2004GL019491.
Shapiro, N.M., Ritzwoller, M.K., Molnar, P., Levin, V., 2004. Thinning and flow of Tibetan crust constrained by seismic anisotropy. Science 305, 233–236.
Shapiro, N.M., Campillo, M., Stehly, L., Ritzwoller, M.H., 2005. High resolution surface wave tomography from ambient seismic noise. Science 307, 1615–1618.
Shen, S.Z., Jin, Y.G., 1999. Brachiopods from the Permian–Triassic beds at the Selong section, Xizang (Tibet), China. J. Asian Earth Sci. 17, 547–559.
Shen, S.Z., Archbold, N.W., Shi, G.R., Chen, Z.Q., 2001. Permian brachiopods from the Selong Xishan section, Xizang (Tibet), China. Geobios 34 (2), 57–182.
Sherrington, H.F., Zandt, G., 2004. Crustal fabric in the Tibetan Plateau based on waveform inversions for seismic anisotropy parameters. J. Geophys. Res. 109, JB02312. http://dx.doi.org/10.1029/2002JB002345.
Shin, Y.H., Xu, H., Braitenberg, C., Fang, J., Wang, Y., 2007. Moho undulations beneath Tibet from GRACE-integrated gravity data. Geophys. J. Int. 170, 971–985.
Shin, Y.H., Shum, C.K., Braitenberg, C., Lee, S.M., Xu, H., Choi, K.S., Baek, J.H., Park, J.U., 2009. Three-dimensional fold structure of the Tibetan Moho from GRACE gravity data. Geophys. Res. Lett. 36, L01302.
Sibson, R.H., 1977. Fault rocks and fault mechanisms. J. Geol. Soc. 133, 191–213.
Smithies, R.H., Van Kranendonk, M.J., Champion, D.C., 2007. The Mesoarchean emergence of modern-style subduction. Gondwana Res. 11 (1–2), 50–68.
Song, T., Wang, X., 1993. Structural styles and stratigraphic patterns of syndepositional faults in a contractional setting: example from Quaidam basin, northwestern China. Am. Assoc. Pet. Geol. Bull. 77, 102–117.
Steffen, A., Lars, A., 2011. Linearized gravity and gauge conditions. Class Quant. Grav. 28, 065001. http://dx.doi.org/10.1088/0264-9381/28/6/065001.
Stern, C.R., 2011. Subduction erosion: rates, mechanisms, and its role in arc magmatism and the evolution of the continental crust and mantle. Gondwana Res. 20, 284–308.
Sun, W., 1989. Bouguer Gravity Anomaly Map of the People's Republic of China (in Chinese), scale 1:4,000,000, Chin. Acad. of Geoexplor., Beijing.
Sun, Y., Li, X., Kuleli, S., Morgan, F.D., Toksöz, M.N., 2004. Adaptive moving window method for 3D P-velocity tomography and its application in China. Bull. Seism. Soc. Am. 94, 740–746.
Tang, Y., Zhang, H., Ying, J., 2006. Asthenosphere–lithospheric mantle interaction in an extensional regime: implication from the geochemistry of Cenozoic basalts from Taihang Mountains, North China Craton. Chem. Geol. 233 (3), 309–327.
Tapponnier, P., Francheteau, J., 1978. Necking of the lithosphere and the mechanics of slowly accreting plate boundaries. J. Geophys. Res. 83, 3955–3970.
Tapponnier, P., Peltzer, G., Armijo, R., 1986. On the mechanics of the collision between India and Asia. In: Coward, M.P., Ries, A.C. (Eds.), Collision Tectonics. Geol. Soc. London, Spec. Publ., 19, pp. 115–157.
Tapponnier, P., Xu, Z., Roger, F., Meyer, B., Arnaud, N., Wittlinger, G., Yang, J., 2001. Oblique stepwise rise and growth of the Tibet plateau. Science 294, 1671–1677.
Teng, J.W., Xiong, S.B., Sun, K.Z., 1981. Explosive seismology for crust and upper mantle structure and velocity distribution beneath Danxiong–Yadong areas, Xizang Plateau. Chin. J. Geophys. 24 (2), 155–170 (in Chinese with English abstract).
Teng, J.W., Sun, K.Z., Xiong, S.B., Yin, Z.X., Chen, L.F., 1983. Deep seismic reflection waves and structure of the crust from Dangxung to Yadong on the Xizang plateau (Tibet). Phys. Earth Planet. Inter. 31 (4), 293–306.
Teng, J.W., Xiong, S.B., Yin, Z.X., 1985a. Structure of the crust and upper mantle pattern and velocity distribution characteristics in the northern region of the Himalayan mountain region. J. Phys. Earth 33, 157–171.
Teng, J.W., Yin, Z.X., Xiong, S.B., 1985b. Crustal structure and velocity distribution beneath the Serlin–Peng–Naqu–Suo region in the Northern Xizang (Tibet) Plateau. Chin. J. Geophys. 28, 28–42 (in Chinese with English abstract).
Teng, J.W., Xiong, X., Zhang, Z., 1997. Deep structure pattern, anisotropy and continental geodynamics revealed by geophysical profiles and transects in China. Geophysics 21, 21–40.
Teng, J.W., Zhang, Z.J., Wang, G.J., Liu, H.B., Hu, J.F., Zhang, B.M., Chen, Y., Zhang, H., 1999. The deep internal dynamical processes and new model of continental–continental collision in Himalayan collision orogenic zone. Chin. J. Geophys. 42 (4), 481–494 (in Chinese with English abstract).
Teng, J.W., Wang, F.Y., Zhao, W.Z., Zhang, Y.Q., Zhang, X.K., Yan, Y.F., Zhao, J.R., Li, M., Yang, H., Zhang, H.S., Ruan, X.M., 2010. Velocity structure of layered block and deep dynamic process in the lithosphere beneath the Yinshan orogenic belt and Ordos Basin. Chin. J. Geophys. 53 (1), 67–85 (in Chinese with English abstract).
Teng, J., Zhang, Z., Zhang, X., Wang, C., Gao, R., Yang, B., Qiao, Y., Deng, Y., 2013. Investigation of the Moho discontinuity beneath the Chinese mainland using deep seismic sounding profiles. Tectonophysics. http://dx.doi.org/10.1016/j.tecto.2012.11.024.
Tian, X., Wu, Q., Zhang, Z., Teng, J., Zeng, R., 2005a. Identification of multiple reflected phases from migration receiver function profile: an example for the INDEPTH-III passive teleseismic P waveform data. Geophys. Res. Lett. 32, L08301. http://dx.doi.org/10.1029/2004GL021885.
Tian, X., Wu, Q., Zhang, Z., Teng, J., Zeng, R., 2005b. Joint imaging by teleseismic converted and multiple waves and its application in the INDEPTH-III passive seismic array. Geophys. Res. Lett. 32, L21315.
Tian, Y., Zhao, D.P., Sun, R., Teng, J., 2009. Seismic imaging of the crust and upper mantle beneath the North China Craton. Phys. Earth Planet. Inter. 2009 (172), 169–182.
Tian, X., Teng, J., Zhang, H., Zhang, Z., Zhang, Y., Yang, H., Zhang, K., 2011. Structure of crust and upper mantle beneath the Ordos Block and the Yinshan Mountains revealed by receiver function analysis. Phys. Earth Planet. Inter. 184 (3), 186–193.
Tilmann, F., Ni, J., INDEPTH III, S.T., 2003. Seismic imaging of the downwelling Indian lithosphere beneath central Tibet. Science 300 (5624), 1424–1427.
Tiwari, V.M., Rao, M.B.S.V., Mishra, D.C., Singh, B., 2006. Crustal structure across Sikkim, NE Himalaya from new gravity and magnetic data. Earth Planet. Sci. Lett. 247, 61–69.
Trap, P., Faure, M., Lin, W., Monié, P., 2007. Late Paleoproterozoic (1900–1800 Ma) nappe stacking and polyphase deformation in the Hengshan–Wutaishan area: implications for the understanding of the Trans-North-China Belt, North China Craton. Precambrian Res. 156, 85–106.
Trap, P., Faure, M., Lin, W., Bruguier, O., Monié, P., 2008. Contrasted tectonic styles for the Paleoproterozoic evolution of the North China Craton. Evidence for a 2.1 Ga thermal and tectonic event in the Fuping Massif. J. Struct. Geol. 30, 1109–1125.
Trap, P., Faure, M., Lin, W., Meffre, S., 2009. The Zanhuang Massif, the second and eastern suture zone of the Paleoproterozoic Trans-North China Orogen. Precambrian Res. 2009 (172), 80–98.
Trap, P., Faure, M., Lin, W., Le Breton, N., Monié, P., 2012. Paleoproterozoic tectonic evolution of the Trans-North China Orogen: toward a comprehensive model. Precambrian Res. 222–223, 191–211.
Turner, S., Hawkesworth, C.J., Liu, J., Rogers, N., Kelley, S., van Calsteren, P., 1993. Timing of Tibetan uplift constrained by analysis of volcanic rocks. Nature 364, 50–53.
Valyus, V.P., 1972. Determining seismic profiles from a set of observations. In: Keilis-Borok (Ed.), Computational Seismology. Consult. Bureau, New-York, pp. 114–118.
Valyus, V.P., Keilis-Borok, V.I., Levshin, A., 1969. Determination of the upper-mantle velocity cross-section for Europe. Proc. Acad. Sci. U.S.S.R. 185, 3.

Van Der Woerd, J., Ryerson, F.J., Tapponnier, P., Gaudemer, Y., Finkel, R., Mériaux, A.S., Caffee, M., Zhao, G.G., He, Q.L., 1998. Holocene left-slip rate determined by cosmogenic surface dating on the Xidatan segment of the Kunlun fault (Qinghai, China). Geology 26, 695–698. http://dx.doi.org/10.1130/0091-7613.
Varga, P., Krumm, F., Riguzzi, F., Doglioni, C., Sule, B., Wang, K., Panza, G.F., 2012. Global pattern of earthquakes and seismic energy distributions: insights for the mechanisms of plate tectonics. Tectonophysics 530–531, 80–86. http://dx.doi.org/10.1016/j.tecto.2011.10.014.
Wang, C.Y., Zeng, R.S., Mooney, W., Hacker, B., 2000. A crustal model of the ultrahigh-pressure Dabie Shan orogenic belt, China, derived from deep seismic refraction profiling. J. Geophys. Res. 105 (B5), 10857–10869.
Wang, Z.Q., Jiang, C.F., Yan, Q.R., Yan, Z., 2001. Accretion and collision orogeneses in the West Kunlun Mountains, China. Gondwana Res. 4, 843–844.
Wang, C.Y., Zhu, L., Lou, H., Huang, B.S., Yao, Z., Lou, X., 2010. Crustal thicknesses and Poisson's ratios in the eastern Tibetan plateau and their tectonic implications. J. Geophys. Res. 115, B11301. http://dx.doi.org/10.1029/2010JB007527.
Wei, W., Unsworth, M., Jones, A., Booker, J., Tan, H., Nelson, D., Chen, L., Li, S., Solon, K., Bedrosian, P., 2001. Detection of widespread fluids in the Tibetan crust by magnetotelluric studies. Science 292, 716–719.
Wei, W.B., Jin, S., Ye, G.F., 2006. MT sounding and lithosphere thickness in North China. Geol. China 33 (2), 762–772 (in Chinese with English abstract).
Welford, J.K., Hall, J., 2007. Crustal structure across the Newfoundland rifted continental margin from constrained 3-D gravity inversion. Geophys. J. Int. 171, 890–908.
Welford, J.K., Shannon, P.M., O'Reilly, B.M., Hall, J., 2010. Lithospheric density variations and Moho structure of the Irish Atlantic continental margin from constrained 3-D gravity inversion. Geophys. J. Int. 183, 79–95.
Wilde, S.A., Zhao, G.C., Sun, M., 2002. Development of the North China Craton during the late Archaean and its final amalgamation at 1.8 Ga: some speculations on its position within a global Palaeoproterozoic supercontinent. Gondwana Res. 5, 85–94.
Wilhem, C., Windley, B.F., Stampfli, G.M., 2012. The Altaids of Central Asia: a tectonic and evolutionary innovative review. Earth Sci. Rev. 113 (3), 303–341.
Willett, S.D., Beaumont, C., 1994. Subduction of Asian lithospheric mantle beneath Tibet inferred from models of continental collision. Nature 369, 642–645.
Williams, H., Turner, S., Kelley, S., Harris, N., 2001. Age and composition of dikes in southern Tibet: new constraints on the timing of east–west extension and its relationship to postcollisional magmatism. Geology 29, 339–342.
Windley, B.F., 1973. Crustal development in the Precambrian. Phil. Trans. R. Soc. Lond. A 273 (1235), 321–341. http://dx.doi.org/10.1098/rsta.1973.0004.
Windley, B.F., 1993. Proterozoic anorogenic magmatism and its orogenic connections: Fermor Lecture 1991. J. Geol. Soc. 150, 39–50. http://dx.doi.org/10.1144/gsjgs.150.1.0039.
Windley, B.F., 1995. The Evolving Continents3rd edition. John Wiley and Sons, Chichester.
Windley, B., Maruyama, S., Xiao, W., 2010. Delamination/thinning of sub-continental lithospheric mantle under Eastern China: The role of water and multiple subduction. Am. J. Sci. 310 (10), 1250–1293.
Windley, B.F., Kröner, A., Guo, J., Qu, G., Li, Y., Zhang, C., 2002. Neoproterozoic to Paleozoic geology of the Altai orogen, NW China: new zircon age data and tectonic evolution. J. Geol. 110, 719–739.
Windley, B.F., Alexeiev, D., Xiao, W., Kröner, A., Badarch, G., 2007. Tectonic models for accretion of the Central Asian Orogenic Belt. J. Geol. Soc. 164 (1), 31–47.
Wittlinger, G., Masson, F., Poupinet, G., Tapponnier, P., Mei, J., Herquel, G., Guilbert, J., Achauer, U., Guanqi, X., Danian, S., 1996. Seismic tomography of Northern-Tibet and Kunlun: evidence for crustal blocks and mantle velocity contrast. Earth Planet. Sci. Lett. 139, 263–279.
Wittlinger, G., Vergne, J., Tapponnier, P., Farra, V., Poupinet, G., Jiang, M., Su, H., Herquel, G., Paul, A., 2004. Teleseismic imaging of subducting lithosphere and Moho offsets beneath western Tibet. Earth Planet. Sci. Lett. 221, 117–130.
Wu, J., Zhang, Z.J., 2012. Spatial distribution of seismic layer, crustal thickness, and Vp/Vs ratio in the Permian Emeishan Mantle Plume region. Gondwana Res. 22 (1), 127–139.
Wu, Y.B., Zheng, Y.F., 2013. Tectonic evolution of a composite collision orogen: an overview on the Qinling–Tongbai–Hong'an–Dabie–Sulu orogeni belt in central China. Gondwana Res. 23, 1402–1428.
Wu, F.Y., Walker, R.J., Ren, X.W., Sun, D.Y., Zhou, X.H., 2003. Osmium isotopic constrains on the age of lithospheric mantle beneath northeastern China. Chem. Geol. 196, 107–129.
Wu, F.Y., Zhao, G.C., Wilde, S.A., Sun, D.Y., 2005. Nd Isotopic constraints on the crustal formation of the North China Craton. J. Asian Earth Sci. 24, 523–545.
Wu, F.Y., Walker, R.J., Yang, Y.H., Yuan, H.L., Yang, J.H., 2006. The chemical–temporal evolution of lithospheric mantle underlying the North China Craton. Geochim. Cosmochim. Acta 70, 5013–5034.
Xia, L.Q., Ma, Z.P., Li, X.M., Xia, Z.C., Xu, X.Y., 2009. Pleocene–Early Eocene (65–40 Ma) volcanic rocks in Tibetan plateau: the products of syn-collisional volcanism. Northwest. Geol. 4 (3), 1–25 (in Chinese with English abstract).
Xiao, W., Kusky, T., 2009. Geodynamic processes and metallogenesis of the Central Asian and related orogenic belts: Introduction. Gondwana Res. 16 (2), 167–169.
Xiao, Y., Zhang, H.F., 2011. Effects of melt percolation on platinum group elements and Re–Os systematics of peridotites from the Tan–Lu fault zone, eastern North China Craton. J. Geol. Soc. 168, 1201–1214.
Xiao, W.J., Windley, B.F., Hao, J., Zhai, M.G., 2003. Accretion leading to collision and the Permian Solonker suture, Inner Mongolia, China: termination of the Central Asian Orogenic Belt. Tectonics 22 (6), 1069. http://dx.doi.org/10.1029/2002TC001484.
Xiao, W., Han, C., Yuan, C., Sun, M., Lin, S., Chen, H., Li, Z., Li, J., Sun, S., 2008. Middle Cambrian to Permian subduction-related accretionary orogenesis of Northern Xinjiang, NW China: implications for the tectonic evolution of central Asia. J. Asian Earth Sci. 32 (2), 102–117.
Xiao, W., Windley, B., Huang, B., Han, C., Yuan, C., Chen, H., Sun, M., Sun, S., Li, J., 2009. End-Permian to mid-Triassic termination of the accretionary processes of the southern Altaids: implications for the geodynamic evolution, Phanerozoic continental growth, and metallogeny of Central Asia. Int. J. Earth Sci. 98 (6), 1189–1217.
Xiao, Y., Zhang, H.F., Fan, W.M., Ying, J.F., Zhang, J., Zhao, X.M., Su, B.X., 2010. Evolution of lithospheric mantle beneath the Tan–Lu fault zone, eastern North China Craton: evidence from petrology and geochemistry of peridotite xenoliths. Lithos 17 (1), 229–246.
Xiong, S.B., Liu, H.B., 1997. Crustal structure in the western Tibetan Plateau. Chin. Sci. Bull. 42 (12), 1309–1311 (in Chinese).
Xiong, X., Teng, J.W., 2002. Crustal movement and deep process of the eastern Tibetan Plateau. Chin. J. Geophys. 45 (4), 527–536 (in Chinese with English abstract).
Xiong, S.B., Teng, J.W., Yin, Z.X., 1985. The thickness of the crust and undulation of Moho discontinuity in Xizang (Tibet) Plateau. Acta Geophys. Sin. 28 (Supp. I), 16–27 (in Chinese with English abstract).
Xu, Y.G., 2001. Thermo-tectonic destruction of the Archean lithospheric keel beneath the Sino-Korean Craton in China: evidence, timing and mechanism. Phys. Chem. Earth A 26, 747–757.
Xu, P.F., Zhao, D.P., 2009. Upper mantle velocity structure beneath the North China Craton: implications for lithospheric thinning. Geophys. J. Int. 177, 1279–1283.
Xu, S.T., Okay, A.J., Ji, S., Sengör, A.M.C., Su, W., Liu, Y., Jiang, L., 1992. Diamond from Dabie Shan metamorphic rocks and its implication for tectonic setting. Science 256, 80–82.
Xu, X.S., O'Reilly, S.Y., Griffin, W.L., Zhou, X.M., 1998. The nature of the Cenozoic lithosphere at Hushan, central eastern China. In: Flower, M., Ching, S.L., Lo, C.H., Lee, T.Y. (Eds.), Mantle Dynamics and Plate Interactions in East Asia. AGU Geodynamics Series, 27, pp. 167–196.
Xu, Y.G., Huang, X.-L., Ma, J.-L., Wang, Y.-B., Iizuka, Y., Xu, J.-F., Wang, Q., Wu, X.-Y., 2004. Crust–mantle interaction during the tectono-thermal reactivation of the North China Craton: constraints from SHRIMP zircon U–Pb chronology and geochemistry of Mesozoic plutons from western Shandong. Contrib. Mineral. Petrol. 147 (6), 750–767.
Xu, Y.G., Blusztajn, J., Ma, J.L., Suzuki, K., Liu, J.F., Hart, S.R., 2008. Late Archean to Early Proterozoic lithospheric mantle beneath the western North China craton: Sr–Nd–Os isotopes of peridotite xenoliths from Yangyuan and Fansi. Lithos 102, 25–42.
Yang, Q.Y., Santosh, M., Shen, J.F., Li, S.R., 2013. Juvenile vs. recycled crust in NE China: Zircon U–Pb geochronology, Hf isotope and an integrated model for Mesozoic gold mineralization in the Jiaodong Peninsula. Gondwana Res. http://dx.doi.org/10.1016/j.gr.2013.06.003.
Yanovskaya, T.B., Ditmar, P.G., 1990. Smoothness criteria in surface wave tomography. Geophys. J. Int. 102, 63–72.
Yao, H., Xu, G., Zhu, L., Xiao, X., 2005. Mantle structure from inter-station Rayleigh wave dispersion and its tectonic implication in western China and neighboring regions. Phys. Earth Planet. Inter. 148, 39–54.
Yao, H., Van Der Hilst, R.D., De Hoop, M.V., 2006. Surface-wave tomography in SE Tibet from ambient seismic noise and two-station analysis: I. Phase velocity maps. Geophys. J. Int. 166, 732–744.
Ye, K., Cong, B.L., Ye, D.N., 2000. The possible subduction of continental material to depths greater than 200 km. Nature 407, 734–736.
Yin, A., 2006. Cenozoic tectonic evolution of the Himalayan orogen as constrained by along-strike variation of structural geometry, exhumation history, and foreland sedimentation. Earth Sci. Rev. 76, 1–131.
Yin, A., Harrison, T.M., 2000. Geological evolution of the Himalayan–Tibetan orogen. Annu. Rev. Earth Planet. Sci. 28, 211–280.
Yin, X.H., Shi, Z.H., Liu, Z.P., 1989. Bouguer gravity anomalies averaged in grid 1° × 1°. In: Ma, X. (Ed.), Lithospheric Dynamics Atlas of China. China Cartographic Publishing House, Beijing, p. 8.
Yin, A., Harrison, T.M., Ryerson, F.J., Chen, W.J., Kidd, W.S.F., Copeland, P., 1994. Tertiary structural evolution of the Gangdese Thrust System, southeastern Tibet. J. Geophys. Res. 99 (B9), 18,175–18,201. http://dx.doi.org/10.1029/94JB00504.
Yin, A., Dubey, C.S., Kelty, T.K., Webb, A.A.G., Harrison, T.M., Chou, C.Y., Célérier, J., 2010. Geologic correlation of the Himalayan orogen and Indian craton: part 2. Structural geology, geochronology, and tectonic evolution of the Eastern Himalaya. Geol. Soc. Am. Bull. 122, 360–395. http://dx.doi.org/10.1130/B26461.1.
Ying, J.F., Zhang, H.F., Kita, N., Morishita, X.H., Shimoda, G., 2006. Nature and evolution of Late Cretaceous lithospheric mantle beneath the eastern North China Craton: constraints from petrology and geochemistry of peridotitic xenoliths from Jünan, Shandong province, China. Earth Planet. Sci. Lett. 244, 622–638.
Ying, J.-F., Zhang, H.-F., Tang, Y.-J., 2010. Lower crustal xenoliths from Junan, Shandong province and their bearing on the nature of the lower crust beneath the North China Craton. Lithos 119, 363–376.
Yuan, X., 1996a. Velocity structure of the Qinling lithosphere and mushroom cloud model. Sci. China Ser. D 39, 235–244.
Yuan, X. C., (Chief compiler), 1996a. Geophysical Atlas of China. Beijing: Geological Publishing House (in Chinese).
Yuan, X., Ni, J., Kind, R., Mechie, J., Sandvol, E., 1997. Lithospheric and upper mantle structure of southern Tibet from a seismological passive source experiment. J. Geophys. Res. 102, 27491–27500.
Yue, Y., Ritts, B.D., Graham, S.A., 2001. Initiation and long-term slip history of the Altyn Tagh Fault. Int. Geol. Rev. 43, 1087–1093.
Zang, S.X., Liu, Y.G., Ning, J.Y., 2002. Thermal structure of the lithosphere in North China. Chin. J. Geophys. 45 (1), 56–66 (in Chinese with English abstract).
Zeng, R.S., Gan, R.J., 1961. Reflected waves from crustal interface in western Qaidam Basin. Acta Geophys. Sin. 10 (1), 120–125 (in Chinese with English abstract).
Zeng, R.S., Lu, H.X., Ding, Z.F., 1988. Seismic refraction and reflection profilings across Tangshan epicentral region and their implication to seismogenic processes. Acta Seism. Sin. 31 (4), 383–398.

Zhai, M.G., Liu, W.J., 2003. Paleoproterozoic tectonic history of the North China Craton: a review. Precambrian Res. 122, 183–199.
Zhai, M.G., Santosh, M., 2011. The early Precambrian odyssey of the North China Craton: a synoptic overview. Gondwana Res. 20, 6–25.
Zhai, M.G., Santosh, M., 2013. Metallogeny of the North China Craton: link with secular changes in the evolving Earth. Gondwana Res. 24, 275–297.
Zhai, M.G., Windley, B.F., Kusky, T.M., Meng, Q.R. (Eds.), 2007. Mesozoic Sub-continental Lithospheric Thinning Under Eastern Asia. Geol. Soc. London, Spec. Publ., 280, pp. 1–352.
Zhang, H.F., 2005. Transformation of lithospheric mantle through peridotite–melt reaction: a case of Sino-Korean craton. Earth Planet. Sci. Lett. 237 (3–4), 768–780.
Zhang, S.F., 2010a. Deep Structure Beneath the Central-south Tibet—Crustal Density Modelling and Azimuthal Anisotropy Variation Inferred from Quasi-Love Waves. (PhD dissertation) University of Trieste.
Zhang, X.M., 2010b. The structural model of the lithosphere–asthenosphere system in the Qinghai–Tibet Plateau and its adjacent areas from surface wave tomography. (PhD dissertation) University of Trieste.
Zhang, Z., Klemperer, S.L., 2005. West–east variation in crustal thickness in northern Lhasa block, central Tibet, from deep seismic sounding data. J. Geophys. Res. 110 (B9), B09403.
Zhang, Z., Klemperer, S.L., 2010. Crustal structure of the Tethyan Himalaya, southern Tibet: new constraints from old wide-angle seismic data. Geophys. J. Int. 181 (3), 1247–1260.
Zhang, Z.M., Santosh, M., 2012. Tectonic evolution of Tibet and surrounding regions. Gondwana Res. 21 (1), 1–3.
Zhang, H.F., Sun, M., 2002. Geochemistry of Mesozoic basalts and mafic dikes in southeastern North China craton, and tectonic implication. Int. Geol. Rev. 44, 370–382.
Zhang, X., Wang, Y., 2009. Crustal and upper mantle velocity structure in Yunnan, Southwest China. Tectonophysics 471 (3), 171–185.
Zhang, J., Zhang, H.F., 2007. Compositional features and P–T conditions of granulite xenoliths from late Cretaceous mafic dike, Qingdao region. Acta Petrol. Sin. 23, 1133–1140 (in Chinese with English abstract).
Zhang, Y.Q., Vergely, P., Mercier, J.L., 1995. Active faulting in and along the Qinling Range (China) inferred from SPOT imagery analysis and extrusion tectonics of south China. Tectonophysics 243, 69–95.
Zhang, Z., Li, Y., Lu, D., Teng, J., Wang, G., 2000. Velocity and anisotropy structure of the crust in the Dabieshan orogenic belt from wide-angle seismic data. Phys. Earth Planet. Inter. 122 (1), 115–131.
Zhang, H.F., Sun, M., Zhou, X.H., Fan, W.M., Zhai, M.G., Yin, J.F., 2002. Mesozoic lithosphere destruction beneath the North China Craton: evidence from major, trace element, and Sr–Nd–Pb isotope studies of Fangcheng basalts. Contrib. Mineral. Petrol. 144, 241–253.
Zhang, H.F., Sun, M., Zhou, X., Zhou, M., Fan, W., Zheng, J., 2003. Secular evolution of the lithosphere beneath the eastern North China Craton: evidence from Mesozoic basalts and high-Mg andesites. Geochim. Cosmochim. Acta 67, 4373–4387.
Zhang, G.W., Dong, Y.P., Lai, S.C., 2004a. Mianlue tectonic zone and Mianlue suture zone on southern margin of Qinling–Dabie orogenic belt. Sci. China Ser. D 47, 300–316.
Zhang, H.F., Sun, M., Zhou, M.F., Fan, W.M., Zhou, X.H., Zhai, M.G., 2004b. Highly heterogeneous Late Mesozoic lithospheric mantle beneath the North China Craton: evidence from Sr–Nd–Pb isotopic systematics of mafic igneous rocks. Geol. Mag. 141, 55–62.
Zhang, H.F., Ying, J.F., Xu, P., Ma, Y.G., 2004c. Mantle olivine xenocrysts entrained in Mesozoic basalts from the North China craton: implication for replacement process of lithospheric mantle. Chin. Sci. Bull. 49 (8), 784–789.
Zhang, H.F., Zhou, X.H., Fan, W.M., Sun, M., Guo, F., Ying, J.F., Tang, Y.J., Zhang, J., Niu, L.F., 2005. Nature, composition, enrichment processes and its mechanism of the Mesozoic lithospheric mantle beneath the southeastern North China Craton. Acta Petrol. Sin. 21, 1271–1280 (in Chinese with English abstract).
Zhang, J., Zhao, G.C., Sun, M., Wilde, S.A., Li, S., Liu, S., 2006. High-pressure mafic granulites in the Trans-North China Orogen: tectonic significance and age. Gondwana Res. 9, 349–362.
Zhang, H.F., Ying, J.F., Shimoda, G., Kita, N.T., Morishita, Y., Shao, J.A., Tang, Y.J., 2007a. Importance of melt circulation and crust–mantle interaction in the lithospheric evolution beneath the North China Craton: evidence from Mesozoic basalt-borne clinopyroxene xenocrysts and pyroxenite xenoliths. Lithos 96 (1), 67–89.
Zhang, J., Zhao, G.C., Li, S.Z., Sun, M., Liu, S., Wilde, S.A., Kröner, A., Yin, C., 2007b. Deformation history of the Hengshan Complex: implications for the tectonic evolution of the Trans-North China Orogen. J. Struct. Geol. 29, 933–949.
Zhang, X.M., Sun, R., Teng, J., 2007c. Study on crustal, lithospheric and asthenospheric thickness beneath the Qinghai–Tibet Plateau and its adjacent areas. Chin. Sci. Bull. 52 (6), 797–804.
Zhang, X.K., Jia, S.X., Zhao, J.R., Zhang, C.K., Yang, J., Wang, F.Y., Zhang, J.S., Liu, B.F., Sun, G.W., Pan, S.Z., 2008. Crustal structures beneath West Qinling–East Kunlun orogen and its adjacent area—results of wide-angle seismic reflection and refraction experiment. Chin. J. Geophys. 51 (2), 439–450 (in Chinese with English abstract).
Zhang, H.F., Goldstein, S.L., Zhou, X.H., Sun, M., Cai, Y., 2009a. Comprehensive refertilization of lithospheric mantle beneath the North China Craton: further Os–Sr–Nd isotopic constraints. J. Geol. Soc. Lond. 166, 249–259.
Zhang, J., Zhao, G.C., Li, S.Z., Sun, M., Liu, S., Yin, C., 2009b. Deformational history of the Fuping Complex and new U–Th–Pb geochronological constraints: implications for the tectonic evolution of the Trans-North China Orogen. J. Struct. Geol. 31, 177–193.
Zhang, Z., Wang, Y., Chen, Y., Houseman, G.A., Tian, X., Wang, E., Teng, J., 2009c. Crustal structure across Longmenshan fault belt from passive source seismic profiling. Geophys. Res. Lett. 36, L17310. http://dx.doi.org/10.1029/2009GL039580.
Zhang, H.F., Zhou, M.F., Sun, M., Zhou, X.H., 2010a. The origin of Mengyin and Fuxian diamondiferous kimberlites from the North China Craton: implication for Palaeozoic subducted oceanic slab–mantle interaction. J. Asian Earth Sci. 37, 425–437.
Zhang, Z., Yuan, X., Chen, Y., Tian, X., Kind, R., Li, X., Teng, J., 2010b. Seismic signature of the collision between the east Tibetan escape flow and the Sichuan Basin. Earth Planet. Sci. Lett. 292 (3–4), 254–264.
Zhang, J., Zhang, H.F., Kita, N., Shimoda, G., Morishita, Y., Ying, J.F., Tang, Y.J., 2011a. Secular evolution of the lithospheric mantle beneath the eastern North China craton: evidence from peridotitic xenoliths from Late Cretaceous mafic rocks in the Jiaodong region, east-central China. Int. Geol. Rev. 53, 182–211.
Zhang, X., Brown, D., Deng, Y., 2011b. Crustal composition model across the Bangong–Nujiang suture belt derived from INDEPTH III velocity data. J. Geophys. Eng. 8 (4), 549–559.
Zhang, Z., Chen, Q.F., Bai, Z.M., Chen, Y., Badal, J., 2011c. Crustal structure and extensional deformation in the thinned lithosphere of North China. Tectonophysics 508, 62–72. http://dx.doi.org/10.1016/j.tecto.2010.06.021.
Zhang, Z., Yang, L.Q., Teng, J.W., Badal, J., 2011d. An overview of the earth crust under China. Earth Sci. Rev. 104 (1–3), 143–166.
Zhang, Z., Deng, Y.F., Teng, J.W., Wang, C., Gao, R., Chen, Y., Fan, W., 2011e. An overview of the crustal structure of the Tibetan plateau after 35 years of deep seismic soundings. J. Asian Earth Sci. 40 (4), 977–989.
Zhang, Z., Klemperer, S., Bai, Z., Chen, Y., Teng, J., 2011f. Crustal structure of the Paleozoic Kunlun orogeny from an active-source seismic profile between Moba and Guide in East Tibet China. Gondwana Res. 19, 994–1007. http://dx.doi.org/10.1016/j.gr.2010.09.008.
Zhang, Z., Wu, J., Deng, Y.F., Chen, Y., Panza, G., 2012. Lateral variation of the strength of the lithosphere across the eastern North China craton: new constraints on the lithospheric disruption. Gondwana Res. 22 (3–4), 1047–1059.
Zhang, Z., Deng, Y.F., Chen, L., Wu, J., Teng, J.W., Panza, G., 2013a. Seismic structure and rheology of the crust beneath mainland China. Gondwana Res. 23 (4), 1455–1483.
Zhang, Z., Wang, Y.H., Deng, Y.F., Chen, L., Wu, J., Teng, J.W., Chen, Y., Fan, W.M., Panza, G., 2013b. Geophysical constraints on Mesozoic disruption of North China Craton by underplating-triggered lower-crust flow of the Archean lithosphere. Terra Nova 25 (3), 245–251.
Zhang, Z., Bai, Z., Klemperer, S., Tian, X., Xu, T., Chen, Y., Teng, J., 2013c. Crustal structure across northeastern Tibet from wide-angle seismic profiling: constraints on the Caledonian Qilian orogeny and its reactivation. Tectonophysics 606, 140–159. http://dx.doi.org/10.1016/j.tecto.2013.02.040.
Zhang, Z., Zhang, G.W., Deng, Y.F., Santosh, M., Teng, J.W., 2013d. Geophysical transect across the North China Craton: a perspective on the interaction between Tibetan eastward escape and Pacific westward flow. Gondwana Res. http://dx.doi.org/10.1016/j.gr.2013.07.004.
Zhao, G.C., Cawood, P.A., 1999. Tectonothermal evolution of the Mayuan Assemblage in the Cathaysia Block; implications for Neoproterozoic collision-related assembly of the South China Craton. Am. J. Sci. 299, 309–339.
Zhao, L.S., Helberger, D.V., 1991. Geophysical implications from relocations of Tibetan earthquakes; hot lithosphere. Geophys. Res. Lett. 18, 2205–2208.
Zhao, W.L., Morgan, W.J., 1984. Injection of Indian crust into Tibetan lower crust: a two dimensional finite element model study. Tectonics 6, 489–504.
Zhao, W.L., Morgan, W., 1985. Uplift of Tibetan Plateau. Tectonics 4, 359–369.
Zhao, G.C., Zhai, M.G., 2013. Lithotectonic elements of Precambrian basement in the North China Craton: review and tectonic implications. Gondwana Res. 23, 1207–1240.
Zhao, Z.F., Zheng, Y.F., 2009. Remelting of subducted continental lithosphere: petrogenesis of Mesozoic magmatic rocks in the Dabie–Sulu orogenic belt. Sci. China Ser. D 52 (9), 1295–1318.
Zhao, W.J., Nelson, K.D., TEAM Project INDEPTH, 1993. Deep seismic reflection evidence for continental underthrusting beneath southern Tibet. Nature 366, 557–559.
Zhao, L.S., Sen, M.K., Stoffa, P., Frohlich, C., 1996. Application of very fast simulated annealing to the determination of the crustal structure beneath Tibet. Geophys. J. Int. 125, 355–370.
Zhao, G.C., Wilde, S.A., Cawood, P.A., Sun, M., 2001a. Archean blocks and their boundaries in the North China Craton: lithological, geochemical, structural and P–T path constraints and tectonic evolution. Precambrian Res. 107, 45–73.
Zhao, G.C., Wilde, S.A., Cawood, P.A., Lu, L.Z., 2001b. High-pressure granulites (retrograded eclogites) from the Hengshan Complex, North China Craton: petrology and tectonic implications. J. Petrol. 42, 1141–1170.
Zhao, W.J., Mechie, J., Brown, L.D., Guo, J., Haines, S., Hearn, T., Klemperer, S.L., Ma, Y.S., Meissner, R., Nelson, K.D., Ni, J.F., Pananont, P., Rapine, R., Ross, A., Saul, J., 2001c. Crustal structure of central Tibet as derived from project INDEPTH wide-angle seismic data. Geophys. J. Int. 145, 486–498. http://dx.doi.org/10.1046/j.0956-540x.2001.01402.x.
Zhao, G.C., Sun, M., Wilde, S.A., Li, S., 2003. Assembly, accretion and breakup of the Paleo-Mesoproterozoic Columbia Supercontinent: records in the North China Craton. Gondwana Res. 6, 417–434.
Zhao, G.C., Sun, M., Wilde, S.A., Li, S.Z., 2005. Late Archean to Paleoproterozoic evolution of the North China Craton: key issues revisited. Precambrian Res. 136, 177–202.
Zhao, G.C., Sun, M., Wilde, S.A., Sanzhong, L., Liu, S., Zhang, J., 2006a. Composite nature of the North China granulite-facies belt: tectonothermal and geochronological constraints. Gondwana Res. 9 (3), 337–348.
Zhao, J.M., Mooney, W.D., Zhang, X., Li, Z., Jin, Z., Okaya, N., 2006b. Crustal structure across the Altyn Tagh Range at the northern margin of the Tibetan Plateau and tectonic implications. Earth Planet. Sci. Lett. 241, 804–814.
Zhao, L., Allen, R.M., Zheng, T., Hung, S.H., 2009. Reactivation of an Archean craton: constraints from P- and S-wave tomography in North China. Geophys. Res. Lett. 36. http://dx.doi.org/10.1029/2009GL039781.
Zhao, G.C., Wilde, S.A., Guo, J.H., Cawood, P.A., Sun, M., Li, X.P., 2010a. Single zircon grains record two Paleoproterozoic collisional events in the North China Craton. Precambrian Res. 177 (3–4), 266–276.

Zhao, J.M., Yuan, X.H., Liu, H.B., Kumar, P., Pei, S.P., Kind, R., Zhang, Z., Teng, J.W., Ding, L., Gao, X., Xu, Q., Wang, W., 2010b. The boundary between the Indian and Asian tectonic plates below Tibet. Proc. Natl. Acad. Sci. 107 (25), 11229–11233.
Zhao, B., Zhang, Z., Bai, Z., Badal, J., Zhang, Z., 2013. Shear velocity and Vp/Vs ratio structure of the crust beneath the southern margin of South China continent. J. Asian Earth Sci. 62, 167–179.
Zheng, J.P., O'Reilly, S.Y., Griffin, W.L., Lu, F.X., Zhang, M., Pearson, N.J., 2001. Relict refractory mantle beneath the eastern North China block: significance for lithosphere evolution. Lithos 57, 43–66.
Zheng, Y.F., Fu, B., Gong, B., Li, L., 2003. Stable isotope geochemistry of ultrahigh pressure metamorphic rocks from the Dabie–Sulu orogen in China: implications for geodynamics and fluid regime. Earth Sci. Rev. 62, 105–161.
Zheng, T.Y., Zhao, L., Chen, L., 2005. A detailed receiver function image of the sedimentary structure in the Bohai Bay Basin. Phys. Earth Planet. Inter. 152, 129–143.
Zheng, T.Y., Chen, L., Zhao, L., Xu, W., Zhu, R., 2006. Crust–mantle structure difference across the gravity gradient zone in North China Craton: seismic image of the thinned continental crust. Phys. Earth Planet. Inter. 159, 43–58.
Zheng, J.P., Griffin, W., O'Reilly, S.Y., Yu, C., Zhang, H., Pearson, N., Zhang, M., 2007a. Mechanism and timing of lithospheric modification and replacement beneath the eastern North China Craton: peridotitic xenoliths from the 100 Ma Fuxin basalts and a regional synthesis. Geochim. Cosmochim. Acta 71 (21), 5203–5225.
Zheng, T.Y., Chen, L., Zhao, L., Zhu, R.X., 2007b. Crustal structure across the Yanshan belt at the northern margin of the North China Craton. Phys. Earth Planet. Inter. 161, 36–49.
Zheng, J.P., Griffin, W., O'Reilly, S., Hu, B., Zhang, M., Tang, H., Su, Y., Zhang, Z., Pearson, N., Wang, F., 2008a. Continental collision and accretion recorded in the deep lithosphere of central China. Earth Planet. Sci. Lett. 269 (3), 497–507.
Zheng, T.Y., Zhao, L., Zhu, R.X., 2008b. Insight into the geodynamics of cratonic reactivation from seismic analysis of the crust–mantle boundary Geophys. Res. Lett. 35, L08303. http://dx.doi.org/10.1029/2008GL033439.
Zheng, T.Y., Zhao, L., Xu, W.W., Zhu, R.X., 2008c. Insight into modification of North China Craton from seismological study in the Shandong Province. Geophys. Res. Lett. 35, L22305. http://dx.doi.org/10.1029/2008GL035661.
Zheng, T.Y., Zhao, L., Zhu, R.X., 2009. New evidence from seismic imaging for subduction during assembly of the North China Craton. Geology 37 (5), 395–398. http://dx.doi.org/10.1130/G25600A.1.
Zheng, Y.F., Xia, Q.X., Chen, R.X., Gao, X.Y., 2011. Partial melting, fluid supercriticality and element mobility in ultrahigh-pressure metamorphic rocks during continental collision. Earth Sci. Rev. 107, 342–374.
Zheng, Y.F., Xiao, W.J., Zhao, G.C., 2013. Introduction to tectonics of China. Gondwana Res. 23 (4), 1189–1206.
Zhou, H., Murphy, M.A., 2005. Tomographic evidence for wholesale underthrusting of India beneath the entire Tibetan Plateau. J. Asian Earth Sci. 25, 445–457.
Zhu, L., Helmberger, D.V., 1996. Intermediate depth earthquakes beneath the India–Tibet collision zone. Geophys. Res. Lett. 23, 435–438.
Zhu, L., Helmberger, D.V., 1998. Moho offset across the northern margin of the Tibetan Plateau. Science 281, 1170–1172.
Zhu, L., Zeng, R., 1990. Three-dimensional P-wave velocity structure under the Beijing network area. Acta Geophys. Sin. 33, 267–277 (in Chinese with English abstract).
Zhu, R.X., Zheng, T.Y., 2009. Destruction geodynamics and Paleoproterozoic plate tectonics of the North China Craton. Chin. Sci. Bull. 54 (14), 1950–1961.
Zhu, J.S., Cao, J.M., Li, X.J., Zhou, B., 1997. The reconstruction of a preliminary three-dimensional earth's model and its implications in China and adjacent regions. Chin. J. Geophys. 40, 627–648 (in Chinese with English abstract).
Zhu, J., Cao, J., Cai, X., Yan, Z., Cao, X., 2002a. High resolution surface wave tomography in East Asia and West Pacific marginal seas. Chin. J. Geophys. 45, 679–698.
Zhu, R.X., Shao, J.A., Pan, Y.X., Shi, R.P., Shi, G.H., Li, D.M., 2002b. Paleomagnetic data from Early Cretaceous volcanic rocks of West Liaoning: evidence for intracontinental rotation. Chin. Sci. Bull. 47, 1832–1837.
Zhu, G., Jiang, D., Zhang, B., Chen, Y., 2012a. Destruction of the eastern North China Craton in a backarc setting: evidence from crustal deformation kinematics. Gondwana Res. 22 (1), 86–103.
Zhu, R.X., Yang, J.H., Wu, F.Y., 2012b. Timing of destruction of the North China Craton. Lithos 149, 51–60.
Zhu, D.C., Zhao, Z.D., Niu, Y., Dilek, Y., Hou, Z.Q., Mo, X.X., 2013. The origin and pre-Cenozoic evolution of the Tibetan Plateau. Gondwana Res. 23 (4), 1429–1454.